# Electromagnetic Properties of Semiconducting Metal Oxides under External Stimulation


**Samuel Partridge**

Supervisor: Prof. A. Porch
Dr. D. Slocombe

Department of Engineering
Cardiff University

This dissertation is submitted for the degree of
*Doctor of Philosophy*

November 2019

# DECLARATION

This thesis is the result of my own independent work, except where otherwise stated, and the views expressed are my own. Other sources are acknowledged by explicit references. The thesis has not been edited by a third party beyond what is permitted by Cardiff University's Use of Third Party Editors by Research Degree Students Procedure.

Signed _____ Date _____

# STATEMENT 1

This thesis is being submitted in partial fulfilment of the requirements for the degree of PhD.

Signed _____ Date _____

# STATEMENT 2

This work has not been submitted in substance for any other degree or award at this or any other university or place of learning, nor is it being submitted concurrently for any other degree or award (outside of any formal collaboration agreement between the University and a partner organisation)

Signed _____ Date _____

# STATEMENT 3

I hereby give consent for my thesis, if accepted, to be available in the University's Open Access repository (or, where approved, to be available in the University's library and for

inter-library loan), and for the title and summary to be made available to outside organisations, subject to the expiry of a University-approved bar on access if applicable.

Signed _____ Date _____

# WORD COUNT 16,300

(Excluding summary, acknowledgements, declarations, contents pages, appendices, tables, diagrams and figures, references, bibliography, footnotes and endnotes)

# Acknowledgements

I would like to express my most sincere thanks to Professor Adrian Porch for believeing in me enough to offer me a PhD, and providing support and guidance throughout especially at my lowest points. I would like to thank Dr Daniel Slocombe for also being there for me and providing me with valuable advice and insight.

My thanks to Dr Johann Bauer, Dr. Markus Heidebrecht, Rodney Riddle who provided support and funding from Merck KGaA, including a range of interesting materials and their chemistry experitise.

Thanks to everyone in the Centre of High Frequency Engineering. In particular Jerome Cuenca for his previous work and insight into his PhD with Merck, and Michael Barter for his collaboration on the degenerate modes paper and helping to iron out the bugs in my software.

Thanks to Andrea Folli for his expertise on photocatalysis and for the x-ray diffraction results.

Thanks to Andrew Rankmore and his team in the mechanical workshop for manufacturing my microwave resonant cavity.

Finally I would like to thank my Mum and Dad for consistently nagging me to get on and finish my thesis, for which I am very grateful!

# Abstract

The main aim of this thesis is to investigate the realtime and long term electrical properties of semiconducting pigments when exposed to light an other environmental stimuli.

A novel rectangular microwave resonant cavity is introduced for measuring the realtime dielectric changes of thin foil samples containing lacqueur and pigment while being exposed to a mostly uniform ultraviolet light source. This in an improvement to the invasive resistive measurements usually used to characterise resistive thin films. It also gives an insight into the localized conductivity of the material compared to the bulk conductivity of a traditional measurement.

A novel temperature correction technique is described which splits degenerate cylindrical cavity modes into a measurement and reference mode. This was tested using a water sample, and was found to be very effective. A simplified analytical method of interpreting the resonant frequencies for temperature correction was also described, and experiments performed to check it's accuracy.

The properties of two sets of photosensitive materials were investigated. Titanium Dioxide ($TiO_2$), which is known for being a brilliant white pigment and effective photocatalyst, was investigated as a powder under ultraviolet, green and red light. It was also investigated during thermal and humidity exposure. The results showed that Anatase $TiO_2$ was more photoactive than Rutile under UV light. A photocatalytic grade of $TiO_2$ with a smaller particle size and Carbon doping didn't show a large change in dielectric loss, however its initial loss was much larger than the other samples suggesting it was already excited from ambient light. A pigment grade of $TiO_2$ with a surface treatment of aluminium, silicon and polysiloxane compunds was also analysed which almost no response to UV light. None of the samples showed significant changes under green and red light.

A range of pigments called Iriotec ® 7000, which are based around Antimony doped Tin Oxide coated onto mica/quartz/talcum substrates, were investigated using the rectangular resonant cavity due to their unusual darkening when exposed to ultraviolet light. The microwave measurements also showed a semi-permanent increase in dielectric loss suggesting

an increase in trapped charge states. The larger particle sizes were in general more conductive than the smaller ones, and the addition of quartz/talcum also increased the conductivity slightly.

Finally the in house built software used to run these experiments was described, including its low level architecture and available features such as a retracking algorithm to keep the frequency sweep close to the resonant frequency of the mode being measured.

# Table of contents

# List of figures

# List of tables

# Nomenclature

**Acronyms / Abbreviations**

| | |
|---|---|
| API | Application Programming Interface |
| ATO | Antimony-doped Tin Oxide |
| BW | Bandwidth |
| CCP | Cardiff Cavity Perturbation |
| DC | Direct Current |
| EM | Electromagnetic |
| EPR | Electron Paramagnetic Resonance |
| ESTA | Electrostaic Application |
| GFC | Glass Fiber Cloth |
| LED | Light Emitting Diode |
| MCP | Microwave Cavity Perturbation |
| PC | Personal Computer |
| RF | Radio Frequency |
| RGB | Red Green Blue |
| SCPI | Standard Commands for Programmable Instruments |
| GFC | $TiO_2$/Glass Fiber Cloth |
| UI | User Interface |

USB Universal Serial Bus

UV Ultraviolet

VISA Virtual Instrument Software Architecture

VNA Vector Network Analyser

XML eXtensible Markup Language

XRD X-Ray Powder Diffraction

ZTO Zinc Tin Oxide

# Chapter 1

# Introduction and Thesis Overview

## 1.1 Introduction Functional Pigments

Functional pigments play a crucial role in today's world, providing useful properties to the products they are coating. These include many products such as sunscreen, self-cleaning glass, anti-static flooring and even as mesh coatings in the water treatment industry. Each of these applications require different properties from the pigments. These properties include but aren't limited to conductivity, laser etchable, pearlescence, Ultraviolet (UV) blocking and photo reactivity.

One such company that produces functional pigments is Merck KGaA. Merck was originally founded in 1668 by Friedrich Jacob Merck as a pharmacy, but has since diversified into the life science and performance materials groups. Within the performance materials group Merck produce a wide variety of functional and visual pigments. For example their Colorstream® pigments are very attractive colour shifting pigments which change based on the angle of observation, while their Iriodin® pigments create a unique pearl lustre effect. Merck also produce more functional pigments such as their Isophor® brand which are phosphors often used in energy saving LEDs, or their Securalic® brand which provide hidden protection from counterfeiting.

This thesis focuses on the analysis of two particular materials: Titanium Dioxide which is a bright white pigment, and a pigment produced by Merck KGaA called Iriotec® 7000 which consists of Antimony Tin Oxide (ATO) coated onto mica, talcum, and quartz substrates. Both of these pigments have a bright appearance, and are used for that property, however they also have some more special and unusual properties. The primary aim of this project is to develop microwave measurement techniques that can measure the dielectric properties of materials in

realtime when exposed to various wavelengths of light. Due to the fact that these exposure experiments also heated the samples slightly, heat and humidity are also measured separately in order to determine the primary mechanism for any changes observed. These experiments may also give an insight into the physics behind these mechanisms.

The primary motivation for understanding these materials is to predict how they will withstand long term exposure in sunlight. Figure 1.1 shows the effect of sunlight on a ceramic figurine. These changes are undesirable, and are especially problematic in the automotive industry where vehicles are exposed to direct sunlight and heat for many hours at a time every day.

Fig. 1.1 Effect of sunlight on a ceramic Gromit figurine. Topside (left) shows bleaching of the pigment compared to the underside (right).

## 1.2 Titanium Dioxide

Titanium Dioxide ($TiO_2$) is an incredibly useful as a white pigment due to its scattering properties, chemical stability and lack of toxicity [1]. It has uses in many applications such as paints, plastics, paper, textiles and also food and pharmaceuticals [2].

$TiO_2$ is also widely used as a photocatalyst, for example in the decomposition of potentially dangerous organic compounds such as pharmaceuticals in wastewater [3–7]. One such technique uses $TiO_2$ coated glass fiber cloth (TGFC) as a practical substrate which could then be fixed into sewage treatment pools and reused. Figure 1.2 shows photographs and

extreme-resolution analytical field-emission scanning electron microscopy (ERSEM) images of glass fiber cloth coated with 0 to 6 layers of $TiO_2$.

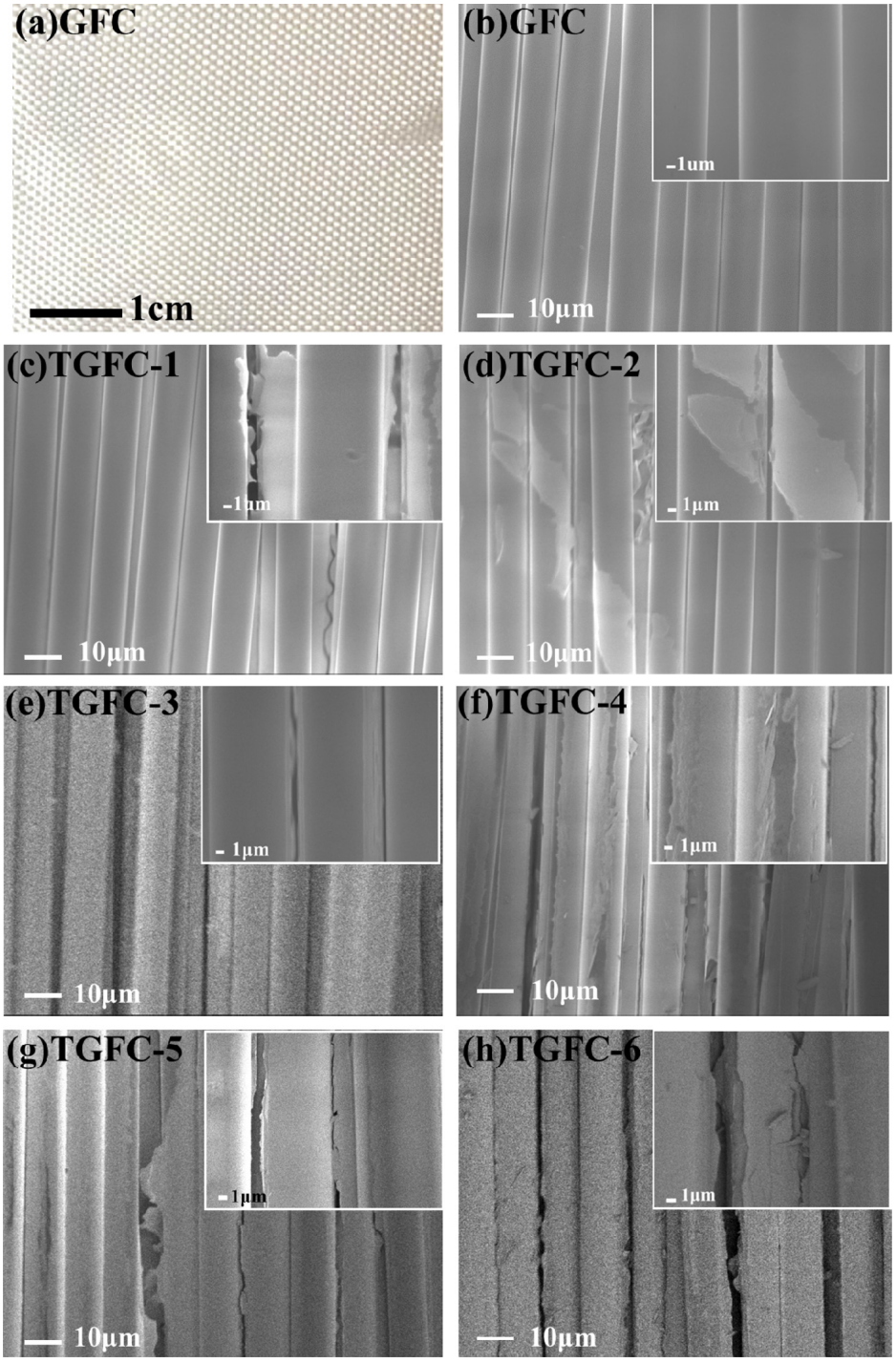


Fig. 1.2 Photograph of untreated GFC (a) and ERSEM images of untreated GFC (b); TGFC-1 (c); TGFC-2 (d); TGFC-3 (e); TGFC-4 (f); TGFC-5 (g) and TGFC-6 (h) [5].

Self cleaning glass is another use of this property where the $TiO_2$ can be deposited as a thin layer on the surface. When exposed to UV light this thin layer can break down any organic compounds on the surface of the glass allowing them to be easily washed away [8, 9]. This can be seen in figure 1.3.

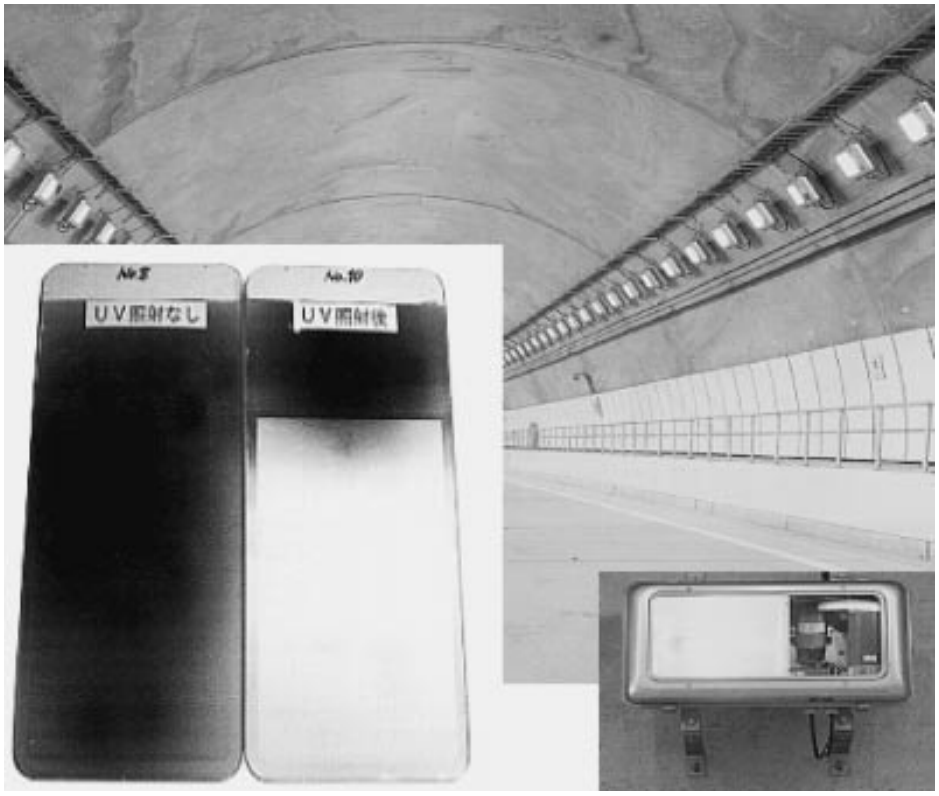


Fig. 1.3 Glass covers on highway tunnel lighting fixtures darkened byautomobile exhaust without $TiO_2$ and maintained clean with $TiO_2$ [10].

Unfortunately when used in paints this photocatalytic activity can also be detrimental to the lacquer matrix within which the $TiO_2$ particles are hosted. The $TiO_2$ induces photodegredation in the host material causing the coating to crack and crumble off of the surfaces [11, 12]. This unwanted effect requires routine maintenance such as re-painting of the surfaces. To reduce this effect the $TiO_2$ particles can be coated in silica ($SiO_2$) and alumina ($Al_2O_3$) to separate the surface of the $TiO_2$ from the lacquer [11, 13]. It is because of these issues that it is important to determine the photo-reactivity of these pigments under UV and visible light radiation.

## 1.3 Iriotec ® 7000

Iriotec® 7000 pigments are designed to be a permanently conductive pigment. In contrast to carbon black, which is a black/dark grey pigment, Iriotec® 7000 is designed to be an almost white or transparent pigment depending on concentration and thickness. These pigments are designed with sheet resistances from $10^4$ to $10^9$ ohms as shown in figure 1.4. All of the following information was obtained from Merck's Minatec® CM pigments brochure which has since been rebranded to the Iriotec® 7000 series.

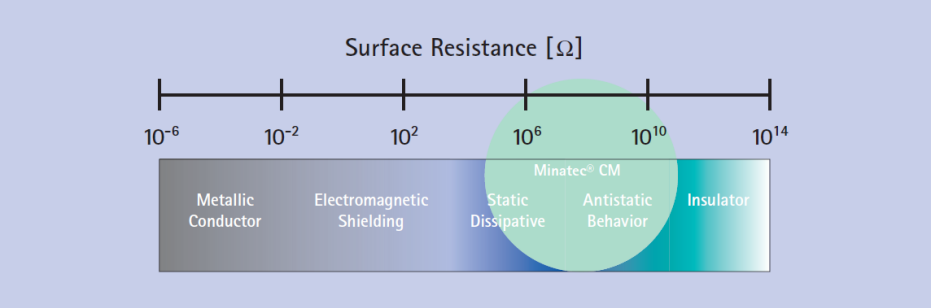


Fig. 1.4 The range of conductivity that can be achieved by applying Iriotec® 7000 pigments in coatings.

The Iriotec® 7000 pigments consist of mica flakes, quartz spheres and talcum flakes coated with a conductive Antimony Tin Oxide (ATO) layer. As shown in figure 1.5, this combination of substrates provides a conductive path to provide conductivity across the entire sheet.

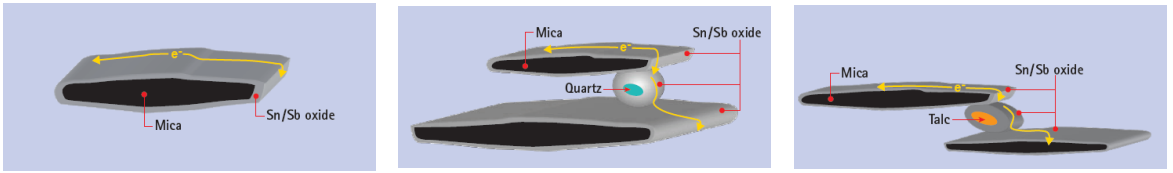


Fig. 1.5 Schematic illustration of Iriotec® 7000 pigments - mica flakes, quartz spheres and talcum flakes coated with conductive metal oxide layer.

These pigments can be used in a wide range of applications. In the automotive industry the properties of the Iriotec ® 7000 pigments make them a suitable light coloured and conductive primer of plastic parts for electrostatic application (ESTA) of paints. In comparison to other methods ESTA protects the environment as it

- requires less coating

- releases less solvent (Volatile Organic Compounds)
- decreases the consumption of raw materials
- saves energy by virtue of the above

The light masstone, i.e. the immediately recognisabe colour, of the Iriotec ® 7000 pigments allow light or colourful car coatings to achieve their full effect.

Iriotec ® 7000 pigments are also widely used in antistatic flooring. Friction and detach movements, as they occur for example when walking across an insulating floor, can build up an electric potential of up to 30,000 volts, which abruptly discharge, often painfully, when making contact with grounded parts. Electronic components are vulnerable against even slight discharges. To protect against discharges, Iriotec ® 7000 pigments can be used in the flooring of warehouses, clean rooms, hospitals, and explosion-proof production areas while maintaining a light appearance which creates a pleasant work atmosphere.

Unfortunately it has been reported by Merck's customers that these pigments undergo a slight colour change when exposed to sunlight. This thesis uses simultaneous microwave measurement with UV illumination to investigate the mechanisms behind this colour change. Microwave based measurements are valuable due to their non-destructive operation while still offering comparable information to much more sophisticated techniques such as Raman and Electron paramagnetic resonance (EPR) spectroscopy.

## 1.4 Thesis Overview

This thesis is split into the following chapters:

**Microwave measurement theory** This chapter summarises the available techniques and provides a base understanding of microwave measurement theory which is used in future chapters.

**Temperature correction methodology** This chapter presents a simplified method of temperature correcting for the thermal expansion and other changes in the microwave resonant cavity. It also presents a novel technique for using degenerate resonant modes as an additional technique for temperature correction.

**Instrument control software** This chapter discusses the design of a software package targeted towards automating experiments using a configurable set of instruments including network analysers, DC power supplies and temperature probes.

**Design of a resonant cavity for light exposure of sheet materials** This chapter discusses the design, manufacturing and testing of a rectangular resonant cavity optimised for large surface area light exposure of sheet samples with simultaneous microwave measurement.

**Properties of Iriotec® 7000 pigment powders when exposed to light** This chapter aims to understand an unusual colour change occuring with Merck's range of antistatic pigments. The experiments primarily use the rectangular cavity discussed in a previous chapter.

**Light exposure of Titanium Dioxide** This chapter aims to understand the photocatalytic properties of Titanium Dioxide when exposed to various wavelengths of light by using simultaneous realtime microwave measurement and exposure.

### 1.4.1 Original Contributions

- The development of a new approach to temperature correction of microwave resonant cavity perturbation measurements using simplified analytical techniques which do not depend on knowledge of the relationship between temperature of the cavity and resonant frequency.
- The development of a new method for temperature correction for cylindrical cavity perturbation measurements using degenerate modes
- Extended analysis of the change in electrical properties of Titanium Dioxide during simultaneous microwave cavity perturbation measurements with light, heat and humidity exposure
- The first use of simultaneous microwave cavity perturbation measurements with UV light exposure for the analysis of Antimony-doped Tin Oxide coated mica platelets, quartz spheres, and talcum platelets for the purpose of understanding the effects on the conductivity of the sample as well as some unusual photochromic effects. A new rectangular resonant cavity with apertures for LED illumination was developed for this experiment.

### 1.4.2 Publications and presentations

- Temperature Correction Using Degenerate Modes for Cylindrical Cavity Perturbation Measurements in IEEE Transactions on Microwave Theory and Techniques [14]. This was in collaboration with Michael Barter.
- Presentations at the Merck CASE conferences, 2016-2018. These were conferences held yearly by Merck as an opportunity for Merck students to share their work and create connections.
- Presentation at the Americal Chemical Society (ACS) conference in New Orleans, spring 2018. This is a yearly conference featuring thousands of presentations on new discoveries in science. My presentation focused on preliminary results showing the use of microwave cavity resonance for the measurement of $TiO_2$ while being exposed to UV light, as well as a background to microwave based measurements considering the chemistry oriented audience.

# Chapter 2

# Microwave Measurement Theory

Techniques that use microwaves are a useful non-invasive means of measuring the dielectric and magnetic properties of bulk materials. They all work on the principle that electromagnetic waves change velocity and get attenuated when passing through a material with different permittivity or permeability than that of free space.

## 2.1 Interaction Between Electric Fields and Materials

When a material is exposed to an electric field, the negatively charged electrons will want to move to cancel out that field, causing the material to become polarized. This polarization vector $\bar{P}_e$ augments the total displacement flux $\bar{D}$

$$\bar{D} = \varepsilon_0 \bar{E} + \bar{P}_e \tag{2.1}$$

where $\varepsilon_0$ is the permittivity of free space and $\bar{E}$ is the applied electric field. In a linear medium this electric polarization of units $C/m^2$ is linearly related to the applied electric field

$$\bar{P}_e = \varepsilon_0 \chi_e \bar{E} \tag{2.2}$$

where $\chi_e$, called the electric susceptibility, is a dimensionless constant that quantifies the polarisation. This then leads to

$$\bar{D} = \varepsilon_0 (1 + \chi_e) \bar{E} = \varepsilon \bar{E} \tag{2.3}$$

At high frequencies there is a phase lag between the polarization and the electric field within the material. The in-phase part of this is then what we call the "polarisation" term, quantifying stored electric field energy, whilst the out-of-phase part quantifies the electric field driven energy dissipation. We then consider the relative permittivity to be a complex quantity as defined below

$$\varepsilon = \varepsilon' - j\varepsilon'' \tag{2.4}$$

Due to energy conservation the imaginary part of $\varepsilon$ must be negative which is explained in more detail by Pozar [15]. If the material has conductivity $\sigma$, then there will also be a current density $\bar{J}$

$$\bar{J} = \sigma\bar{E} \tag{2.5}$$

Substituting these into Maxwell's curl equation for $\bar{H}$ results in

$$\begin{aligned}
\nabla \times \bar{H} &= j\omega\bar{D} + \bar{J} && \text{(2.6a)}\\
&= j\omega\varepsilon\bar{E} + \sigma\bar{E} && \text{(2.6b)}\\
&= j\omega\left(\varepsilon - j\frac{\sigma}{\omega}\right)\bar{E} && \text{(2.6c)}\\
&= j\omega\left(\varepsilon' - j\left(\varepsilon'' + \frac{\sigma}{\omega}\right)\right)\bar{E} && \text{(2.6d)}
\end{aligned}$$

The loss due to conductivity is indistinguishable from the loss due to dielectric damping. These can be combined to form an equation for relative permittivity:

$$\begin{aligned}
\varepsilon_r &= \frac{\varepsilon}{\varepsilon_0} && \text{(2.7a)}\\
&= \varepsilon_1 - j\varepsilon_2 && \text{(2.7b)}\\
&= \frac{1}{\varepsilon_0}\left(\varepsilon' - j\left(\varepsilon'' + \frac{\sigma}{\omega}\right)\right) && \text{(2.7c)}
\end{aligned}$$

This is a slightly different definition to Pozar who uses $\varepsilon' = \varepsilon_r\varepsilon_0$.

There are 3 main causes of polarization in a dielectric material: electronic, molecular and orientational [16]. Electronic polarization is the movement of the bound electron clouds

surrounding the ions of the material. Molecular polarization is caused by the stretching of the bonds between atoms. This stretching occurs due to the atoms giving or sharing electrons between each-other as part of the bonding process, causing them to become slightly positively or negatively charged. Finally orientational polarization is the rotation of whole molecules which have a permanent or induced dipole moment. In conductive or semi-conductive materials the electrons are also allowed to move beyond the bounds of the atom, but are still restricted by the overall material boundary, whether that's small particles or a solid block.

Both the conductivity and dipolar mechanisms can be represented by the Debye relaxation equation [16–18]:

$$\varepsilon_{r,Debye}(\omega) = \varepsilon'(\infty) + \frac{\varepsilon'(0) - \varepsilon'(\infty)}{1 + j\frac{\omega}{\omega_r}} \tag{2.8}$$

where $\varepsilon'(0)$ is the permittivity at DC, $\varepsilon'(\infty)$ is the permittivity at an infinite frequency, and $\omega_r$ is the frequency at which the permittivity transitions between the two.

Other improvements have been made to the Debye model, for example the Cole-Cole and Cole-Davidson formulae which raise various parts of the denominator to a power.

If the mechanism has a restoring force then the Lorentz resonator model can be used instead [19]

$$\varepsilon_{r,Lorentz}(\omega) = \varepsilon'(\infty) + \varepsilon'(0)\frac{\omega_p^2}{\omega_r^2 - \omega^2 + j\gamma\omega_r\omega} \tag{2.9}$$

where $\omega_r$ is the resonant frequency, $\gamma$ is the damping coefficient, and $\omega_p$ is known as the plasma frequency.

Regardless of the models used, multiple mechanisms will come together to define the complete frequency response of a material. An example of this is shown in figure 2.1.

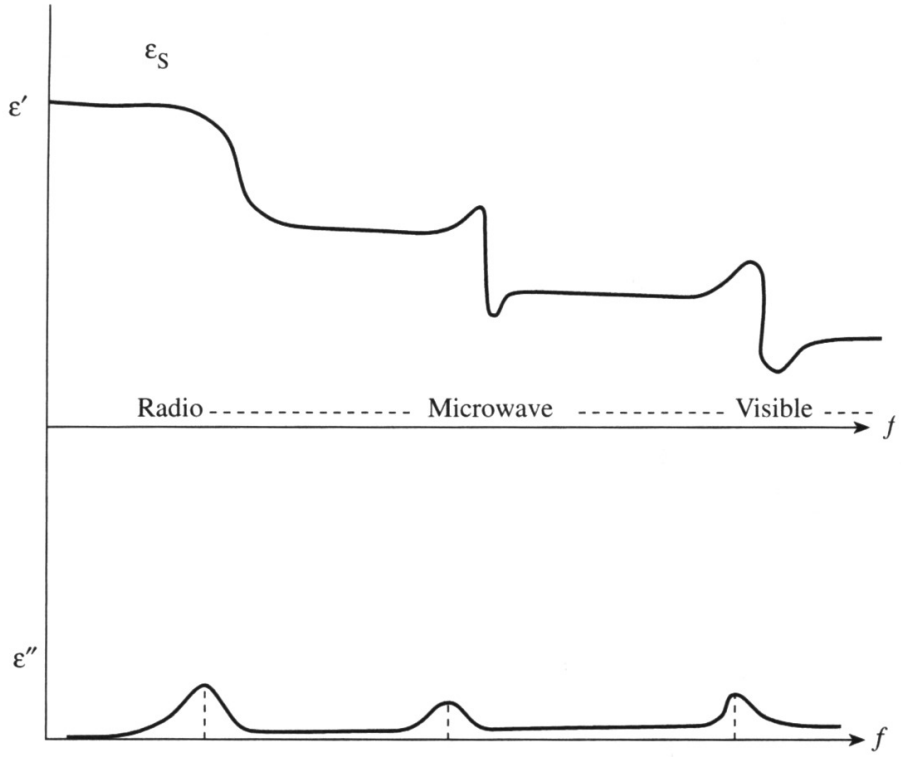


Fig. 2.1 Typical variation of $\varepsilon_1$ and $\varepsilon_2$ with frequency [16]. In the order of increasing frequency, the three shifts correspond to the rotation of polar molecules, stretching of the bonds between atoms, and distortion of the electron clouds surrounding the individual ions.

## 2.2 Overview of Microwave Measurement Techniques

Microwave measurement techniques can be divided into two categories, resonant and non-resonant. Resonant techniques make use of a microwave structure that has one or more resonant modes of operation. A sample is then introduced into the electric or magnetic field of the resonant structure which causes a shift in resonant frequency and bandwidth. This shift can then optionally be converted back into an effective permittivity. Non-resonant techniques are not restricted to spot frequencies and involve measurement of the amplitude and phase of a transmitted and/or reflected microwave signal which has been modified by the presence of the sample; such techniques, whilst broadband, lack the inherent sensitivity of measurement of resonant techniques.

### 2.2.1 Resonant Techniques

Some examples of host microwave resonators used for EM property measurement of materials are discussed in detail below.

#### Hairpin Resonator

The basic structure of a hairpin resonator is a u-shaped metallic conductor. This can be as simple as a bent length of wire, or a specially machined structure [20–22]. An example is shown in figure 2.2.

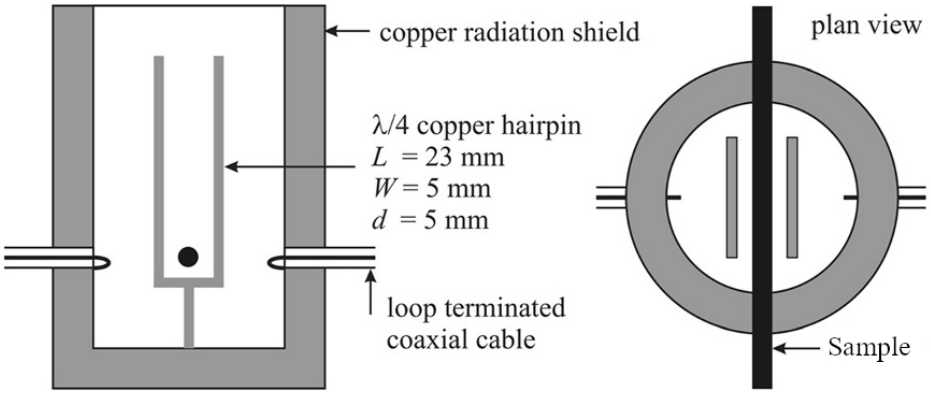


Fig. 2.2 Schematic diagram of a copper hairpin resonator [23].

When coupled to an external microwave source at the appropriate resonant frequency a strong magnetic field will develop at the base of the u-shape, and an electric field between the ends of the prongs. These can be seen in figure 2.3.

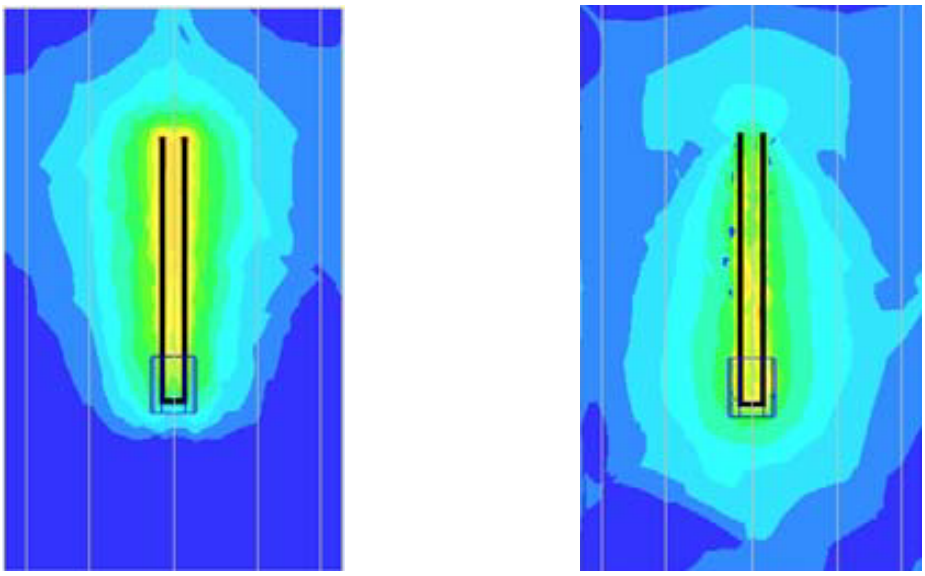

Fig. 2.3 Electric and magnetic field distribution simulations [24].

The main advantage of hairpin resonators is they provide a large area for external stimuli. For example they have been used for simultaneous microwave and X-ray diffraction to measure ammonia storage materials [25].

### Split Ring Resonator

Split ring resonators come in various shapes and sizes such as toroids, hollow cylinders, and even PCB structures such as hollow circles and rectangles [26–29]. Despite the differences, all these structures contain a split within the shape which becomes the capacitive element of the resonator with almost all of the electric field concentrated within this gap. Figure 2.4 ilustrates the electric and magnetic fields.

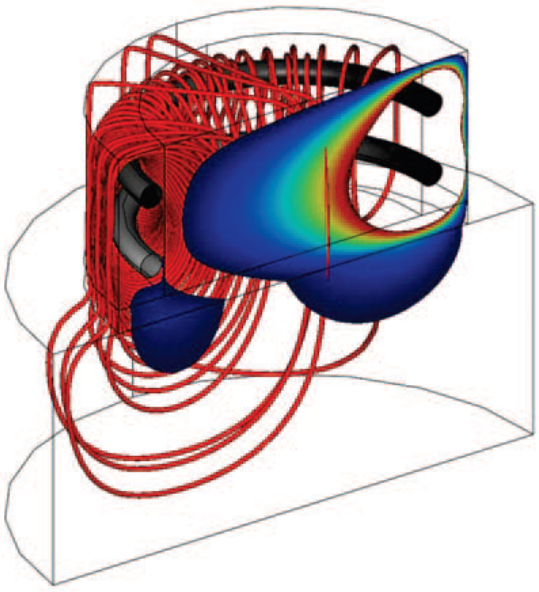

Fig. 2.4 Comsol multiphysics simulation of a double ring resonator designed for blood glucose measurement [27]. The magnetic field is shown as the red lines, and the electric field the red and blue overlay.

Just like with the hairpin resonator, a sample can be placed within the electric field which will cause a shift in resonant frequency and bandwidth of the structure which can be measured by an external network analyser.

### Microwave Cavity Resonator

Microwave cavity resonators are closed metal cavities which can be constructed in a range of shapes from cuboids [30–32], cylinders [33–35], spheres, or even hybrid shapes [36]. The cavities are usually air-spaced, but can be filled with a low loss dielectric such as PTFE or sapphire to reduce the resonant frequencies for a given size. The samples themselves can also vary in shape from sheets to cylindrical pucks to tubes.

### Parallel Plate Resonator

At low frequencies a parallel plate capacitor structure is often used for measuring the dielectric constant of a material [37, 38]. These are constructed by sandwiching a dielectric

layer between two parallel conducting plates. Ignoring fringe effects, the capacitance is approximately equal to the following

$$C \approx \frac{\varepsilon_r \varepsilon_0 A}{d} \tag{2.10}$$

where $\varepsilon_r$ is the relative permittivity of the dielectric, $A$ is the surface area, and $d$ is the dielectric thickness.

At higher frequencies the inductive elements of the structure become significant, and so resonant techniques must be used instead. To simplify the calculation of the field patterns a dielectric rod is often used between the plates [39–41]. Two coaxial probes can then be used to couple into and measure the resonant frequency and bandwidth of the structure.

### 2.2.2 Non-resonant Techniques

Unlike resonant techniques, non-resonant techniques allow measurements of samples across a continous range of frequencies. The most common non-resonant techniques use coaxial cable or waveguide test fixtures, as now will be described.

#### Coaxial Probe

A coaxial probe is constructed from an open ended coaxial cable. The other end of the coaxial cable is then connected to a VNA which will be configured to perform a measurement of the voltage reflection coefficient $S_{11}$. This reflection is caused by an impedance mismatch between the coaxial cable and the sample under test. A schematic of a coaxial probe is shown in figure 2.5.

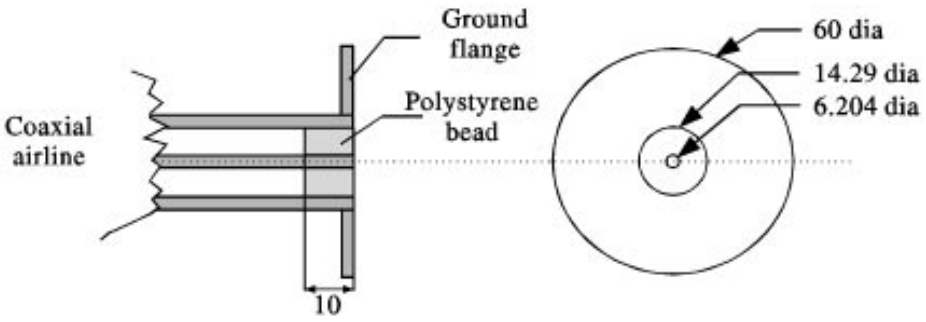


Fig. 2.5 Example schematic of a coaxial probe [42].

One of the drawbacks to coaxial probes is that the electric field protrudes a very small distance from the end of the probe. For a liquid sample this is not an issue [43–45], however for solid samples it is critical to maintain a good surface contact between the sample and the probe. Any slight air gaps can adversely affect the measurement, causing both the permittivity and loss of the sample under test to be underestimated; this is a major systematic error for high permittivity materials, and materials which are not flat (e.g. powders). To help with this, coaxial probes are typically constructed with a flange and optionally some clamping mechanism to ensure a good contact.

This small field penetration can also be an advantage however, especially for thin film samples. With a suitable film thickness the probe can be used to measure the film without being affected by the substrate [46].

### Waveguide

Waveguides are another non-resonant measurement technique to measure samples at a range of frequencies. There are two primary modes of operation: short circuit $S_{11}$ only measurement, and open circuit $S_{11}/S_{21}$ measurement. These are shown in figure 2.6.

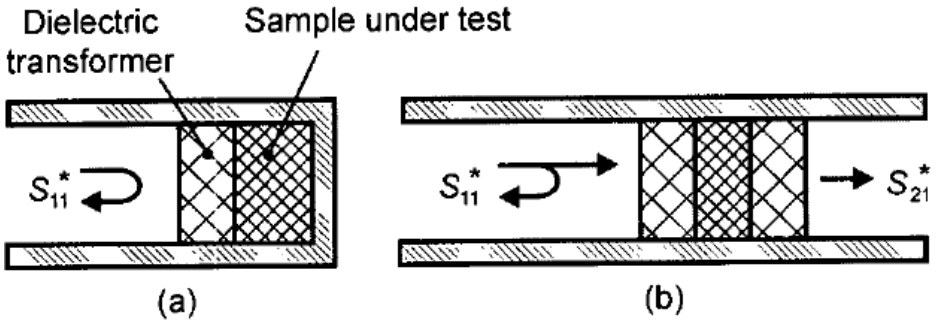


Fig. 2.6 Measurement schemes of (a) the short-circuit line and (b) the transmission/reflection measurement method [47].

The obvious advantage of waveguide measurements over coaxial probe measurements is the ability to measure the bulk of the sample as opposed to the surface. However they have a smaller bandwidth, associated with the inherent bandwidth of the host waveguide for single mode operation.

## 2.3 Microwave Cavity Resonance

Before delving into the theory behind cavity perturbations it is useful to have an understanding of how an unperturbed microwave resonant cavity operates.


Fig. 2.7 Resistive, capacitive and inductive elements that represent a lossy resonant cavity

A microwave resonant cavity operates by exchanging energy between the electric and magnetic field. This energy exchange can be represented as a series RLC resonant circuit. The resistance represents the losses in the cavity walls, and the inductance and capacitance represent the energy stored within the electric and magnetic fields. The impedance of the cavity can be represented by the following equation [15]:

$$Z(\omega) = R + j\omega L + \frac{1}{j\omega C} \approx R\left[1 + j2Q_0\left(\frac{\omega - \omega_0}{\omega_0}\right)\right] \tag{2.11}$$

At resonance the impedance becomes entirely real. From the roots of the reactance we can derive an equation for complex resonant frequency:

$$\omega \approx \omega_0 + j\frac{\omega_0}{2Q_0} \tag{2.12}$$

This will become useful later in section 2.4 when calculating complex frequency shift of a perturbed cavity.

### 2.3.1 Microwave Cavity Coupling

For a resonant cavity to be useful it has to be coupled to an external system. This is usually achieved through the use of small probe or loop antennas which couple into the electric and magnetic fields, respectively. The circuit model of figure 2.7 now becomes as follows:

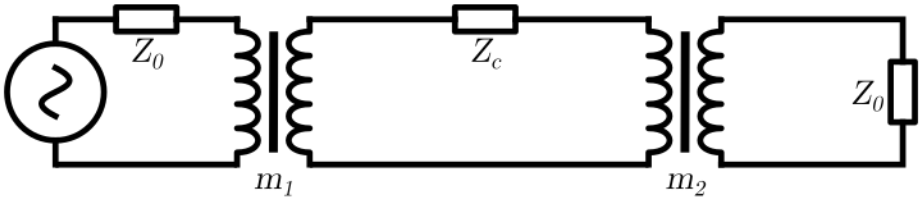


Fig. 2.8 Microwave cavity resonator represented as $Z_C$ with coupling loops.

Using Kirchoff's voltage law and mesh analysis, and a conversion from impedance to scattering parameters, we can derive an equation for the transmitted power:

$$|S_{21}|^2 = \frac{4g_1g_2}{(g_1+g_2+1)^2+4Q_0^2\left(\frac{\omega-\omega_0}{\omega_0}\right)^2} \tag{2.13}$$

where $g_n$ are defined as the coupling coefficients of the resonator:

$$g_n = \frac{\omega_0^2 m_n^2}{Z_0 Z_R} \approx \frac{\omega_0^2 m_n^2}{Z_0 R} \tag{2.14}$$

This equation however is still in terms of the inherent (i.e. "unloaded") quality factor $Q_0$ of the resonator. When performing a measurement the value we obtain is the loaded quality factor $Q_L$ since the effect of the coupling coefficients is to broaden the 3 dB bandwidth (i.e. reduce the measured, or "loaded", quality factor $Q_L$) by the factor $1+g_1+g_2$. We are also able to measure the peak transmitted power $P_0$ at the resonant frequency, i.e. when $\omega = \omega_0$. An equation for $|S_{21}|^2$ can then be derived in terms of these two parameters:

$$|S_{21}|^2 = \frac{P_0}{1+4Q_L^2\left(\frac{\omega-\omega_0}{\omega_0}\right)^2} \tag{2.15}$$

Quite simply, we can now write $Q_L = Q_0(1-\sqrt{P_0})$. The assumption that $g_1 \approx g_2 = g$ was also made. This is known as "symmetric coupling", where the two coupling structures are assumed to be identical. This is now in the form of a standard lorentzian function $1/1+x^2$ with the appropriate translation and scaling. The $|S_{21}|^2$ meausrement from the network analyser can then either be a non-linear curve fit to equation 2.15, or the $P_0$ and $Q_L$ paramaters can be extracted directly by measuring the peak power and the half power bandwidth. A non-linear curve fit is generally preferred since it will be less susceptible to noise, especially at low power levels.

Symmetric coupling can be achieved experimentally by analysing the $S_{11}$ and $S_{22}$ reflection parameters separately. The coupling is equal when the resonant troughs have identical amplitudes.

### 2.3.2 Resonance Skew and Correction

When a resonant mode has a high Q factor without nearby interfering modes, Equation 2.13 is a reasonably accurate fit. However when there are other modes nearby, or there is cross coupling between the coupling antennas, then the curve can become significantly skewed, and Equation 2.13 is no longer a good fit. The resonator model can be extended to an arbritrary number of modes and cross couplings as shown in Figure 2.9.

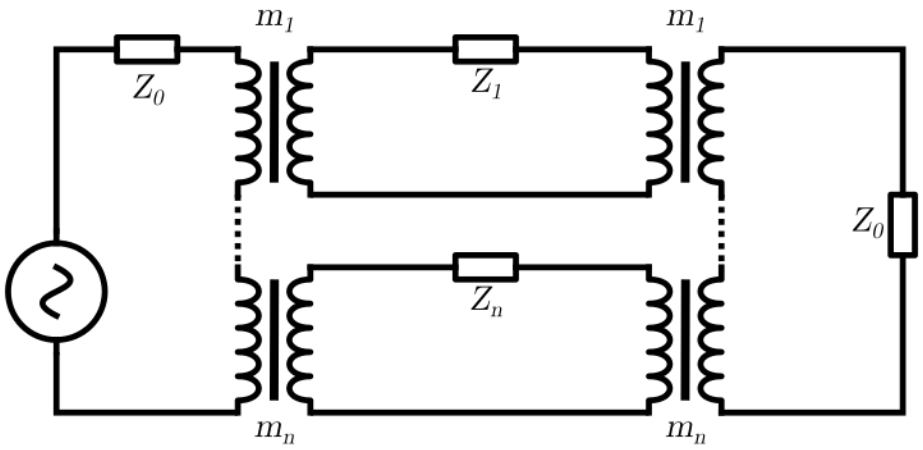


Fig. 2.9 Generalised microwave cavity resonator model with arbritrary number of resonance or crosstalk terms

The $S_{21}$ response for $N$ terms can be derived:

$$S_{21,N} = \frac{2\sum_{n=1}^{N} \frac{g_n}{G_n(\omega)}}{1+2\sum_{n=1}^{N} \frac{g_n}{G_n(\omega)}} \tag{2.16}$$

where $G_n = \frac{Z_n}{R}$. For a resonator $Z_n$ is equal to that in equation 2.11 which results in the following:

$$G_n = 1 + j2Q_0\left(\frac{\omega-\omega_0}{\omega_0}\right) \tag{2.17}$$

For a cross coupling term $G_n$ is defined as:

$$G_n = \frac{j\omega L_{skew}}{R} = jX_{sk}(\omega) \tag{2.18}$$

These terms can be combined to produce various responses as shown in Figure 2.10.

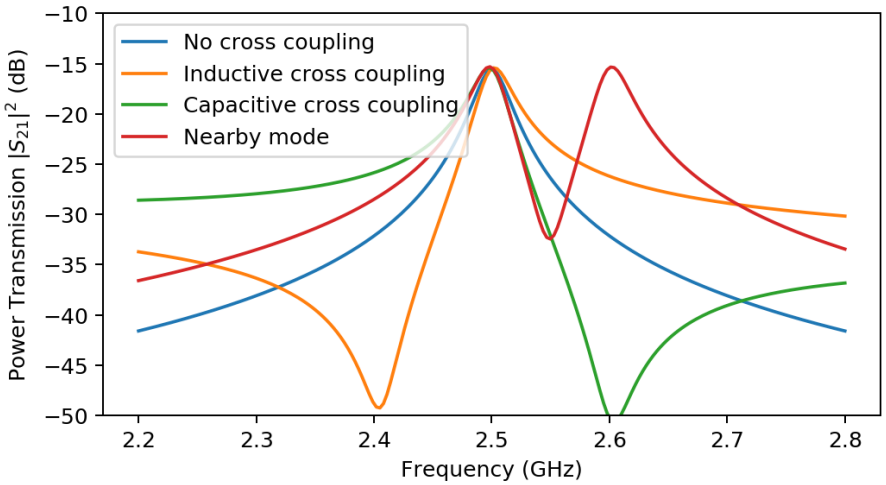


Fig. 2.10 Examples of skew caused by capacitive and inductive cross coupling, and by nearby modes.

The red and green traces in the figure above represent a single resonant mode with a capacitive or inductive skew term. These two terms can be substituted into equation 2.16 resulting in the the following:

$$|S_{21}|^2 = \frac{2g\left(1+\frac{G_{res}(\omega)}{G_{skew}(\omega)}\right)}{G_{res}(\omega)+2g\left(1+\frac{G_{res}(\omega)}{G_{skew}(\omega)}\right)} \tag{2.19}$$

A resonant cavity is almost always designed to minimise cross coupling, and so ideally the skew impedance should be a lot larger than the resonator impedance. This allows us to eliminate the skew term in the denominator. After some rearranging and substitutions we can obtain an equation which will allow us to correct for a small amount of skew:

$$|S_{21}|^2 = \frac{P_0 + 2P_0\frac{G_{res}}{G_{skew}} + P_0\left(\frac{G_{res}}{G_{skew}}\right)^2}{1+4Q_L^2\left(\frac{\omega-\omega_0}{\omega_0}\right)^2} \tag{2.20}$$

The equation above now contains first and second order terms in the numerator. In practice only the first order term is required. Figure 2.11 shows the effectiveness of various fitting methods to a skewed curve:

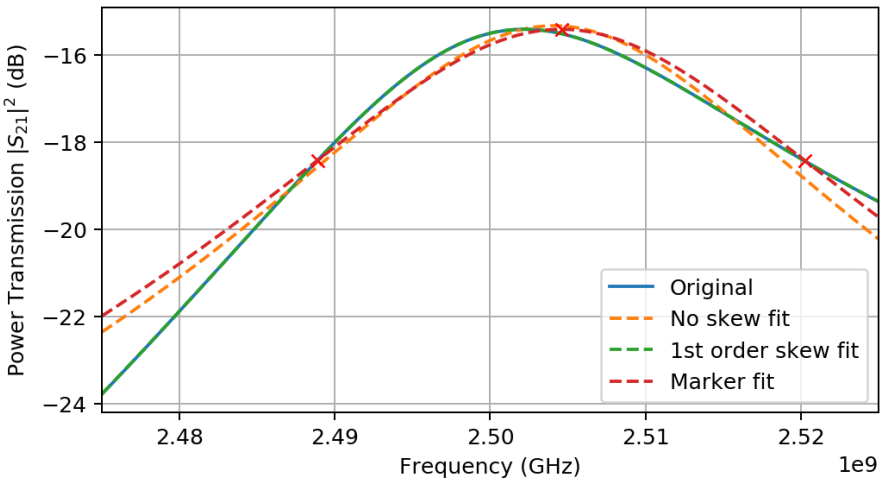


Fig. 2.11 Fitting to a skewed Lorentzian curve using no skew correction, 1st order correction and 3dB marker points. The 1st order correction almost perfectly matches the original.

The figure already shows that a first order skew fitting performs better than a fitting without skew, or using 3dB markers. Table 2.1 compares the systematic errors of the various methods.

| Method | $f_0$ (GHz) | $f_0$ error (MHz) | BW (MHz) | BW error (MHz) |
|---|---|---|---|---|
| Original | 2.5000000 | | 25.000 | |
| No skew | 2.5041026 | 4.103 | 23.981 | -1.019 |
| 1st order | 2.4999340 | -0.066 | 24.912 | -0.088 |
| 2nd order | 2.4999381 | -0.062 | 24.961 | -0.039 |
| Markers | 2.5045612 | 4.561 | 26.060 | 1.060 |

Table 2.1 Comparison of various fitting methods with the loaded Q factor set to 100 as an example value where skewness starts to become an issue.

1st order fitting simply omits the $(G_{res}/G_{skew})^2$ term from equation 2.20 above as this is usually negligible. The 2nd order skew correction performs marginally better than the first order skew correction, however again both outperform the no skew and marker fitting methods. It is important to note that the above bandwidth values were also converted from loaded bandwidth to unloaded by multiplying by $1-\sqrt{P_0}$. Without this all of the values were approximately 5 MHz too large.

## 2.4 Resonant Cavity Perturbation

On their own, resonant cavities have been used as bandpass filters [48–50], however they can also be used as non-contact measurement devices [51–53]. Some authors have also analysed the accuracy of these measurements [54, 55] including errors caused by the sample hole [56].

The standard first-order perturbation equation as given by Waldron is [57]

$$-\frac{\delta\omega}{\omega} \approx \frac{\int_{V_{samp}} \varepsilon_0(\varepsilon_r-1)\bar{E}_{samp}\cdot\bar{E}^*_{cav}+\mu_0(\mu_r-1)\bar{H}_{samp}\cdot\bar{H}^*_{cav}dV}{\int_{V_{cav}} \varepsilon_0\bar{E}_{cav}\cdot\bar{E}^*_{cav}+\mu_0\bar{H}_{cav}\cdot\bar{H}^*_{cav}dV} \tag{2.21}$$

where $\bar{E}_{samp}$ and $\bar{H}_{samp}$ are the electric and magnetic fields at the sample location, $\bar{E}_{cav}$ and $\bar{H}_{cav}$ are the unperturbed fields, and $\varepsilon_r$ and $\mu_r$ are the complex relative permittivity and permeability respectively.

If the sample is mostly within the E or H field then the other term in the numerator becomes zero. Also the denominator can be expressed in terms of E field since $\varepsilon_0\bar{E}^2_{cav} = \mu_0\bar{H}^2_{cav}$.

If perturbation is non depolarizing then the electric field in the sample can be assumed to be the same as the electric field of the cavity. Making these assumptions and rearranging yields

$$\varepsilon_r \approx -2\left(\frac{\Delta\omega}{\omega}\right)\frac{V_{eff}}{V_{samp}}+1 \tag{2.22}$$

Using the definition $\varepsilon_r = \varepsilon_1 - j\varepsilon_2$ [15], and equation 2.12 from earlier the following equations can be derived

$$\varepsilon_1 \approx -2\left(\frac{\omega_s-\omega_0}{\omega_0}\right)\frac{V_{eff}}{V_{samp}}+1 \tag{2.23a}$$

$$\varepsilon_2 \approx \left(\frac{1}{Q_s}-\frac{1}{Q_0}\right)\frac{V_{eff}}{V_{samp}} \tag{2.23b}$$

where $V_{eff}$ is the effective cavity volume and $V_{samp}$ is the sample volume. The equations are approximate since we have made the assumption that $\omega$ in the denominator is entirely real. With a high Q factor when empty this assumption works well. The effective cavity volume is a function of the physical cavity volume, and the distribution of electric field within the cavity. Assuming the electric field within the sample is constant, this can be defined as

$$V_{eff} = \frac{\int_{V_{cav}} \bar{E}_{cav}^2 dV}{\bar{E}_{samp}^2} \tag{2.24}$$

This value can be obtained by calibration by placing a sample of known volume and permittivity into the cavity and measuring the resulting frequency shift. A quartz rod is a common choice.

When measuring a sample, two readings are required. One of an empty sample tube, and one with the sample. Figure 2.12 shows an example of these two measurements along with an empty cavity.

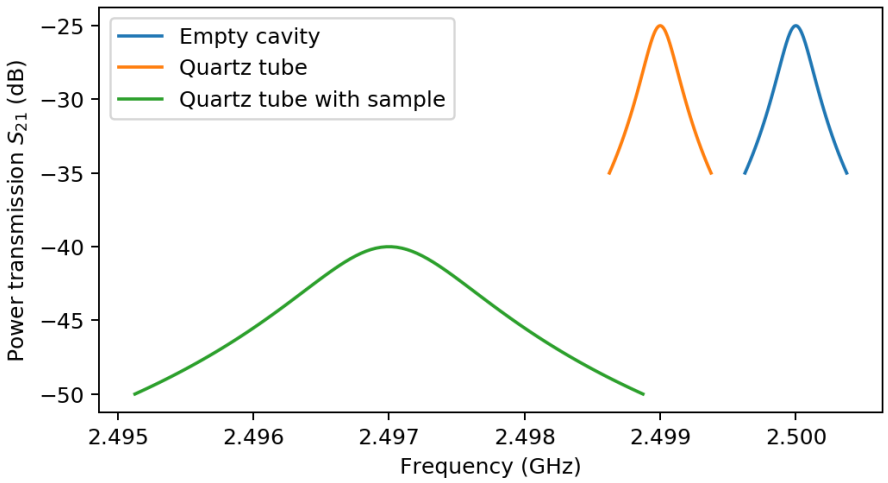


Fig. 2.12 An example MCP measurement.

## 2.5 Cylindrical Resonant Cavity Modes

All resonant cavity modes can be derived from Helmholtz's equations which in turn can be derived from Maxwell's equations shown below.

$$\nabla \times E = -j\omega\mu\bar{H} \tag{2.25a}$$

$$\nabla \times H = -j\omega\varepsilon\bar{E} \tag{2.25b}$$

For the electric field Helmholtz equation we can then take the curl of equation 2.25a and combine it with equation 2.25b to elminiate any $\bar{H}$ terms.

$$\nabla \times \nabla \times \bar{E} = -j\omega\mu\nabla \times \bar{H} = \omega^2\mu\varepsilon\bar{E} \tag{2.26}$$

Using the vector identity $\nabla \times \nabla \times \bar{A} = \nabla(\nabla \cdot \bar{A}) - \nabla^2\bar{A}$ this can then be converted into the Helmholtz equation for the electric field of a wave.

$$\nabla^2\bar{E} + \omega^2\mu\varepsilon\bar{E} = 0 \tag{2.27}$$

A similar equation can be derived for the magnetic field

$$\nabla^2\bar{H} + \omega^2\mu\varepsilon\bar{H} = 0 \tag{2.28}$$

Using this equation and the boundary conditions for a cylindrical resonant cavity, an equation for the $E_z$ field component of a transverse magnetic resonant mode can be derived. The full derivation is shown in appendix A.2.

$$E_z(r,\phi,z) = E_0 J_m\left(\frac{\alpha_{mn}r}{a}\right)\cos\left(m\left(\phi \pm \frac{\pi}{4}\right)\right)\cos\left(\frac{z\pi p}{h}\right) \tag{2.29}$$

To calculate the $H$ field we can substitute this equation back into equation 2.25a. Since the electric field is only in the $z$ direction for $\text{TM}_{mmp}$ modes, the curl simplifies to

$$H_r(r,\phi,z) = -\frac{1}{j\omega\mu r}\frac{\partial E_z}{\partial\phi} \tag{2.30a}$$

$$H_\phi(r,\phi,z) = \frac{1}{j\omega\mu}\frac{\partial E_z}{\partial r} \tag{2.30b}$$

$$H_z(r,\phi,z) = 0 \tag{2.30c}$$

Solving the differentials we get

$$H_r(r,\phi,z) = -\frac{jmE_0}{\omega\mu r} J_m\left(\frac{\alpha_{mn} r}{a}\right) \cos\left(\frac{z\pi p}{h}\right) \sin\left(m\left(\phi \pm \frac{\pi}{4}\right)\right) \tag{2.31a}$$

$$H_\phi(r,\phi,z) = -\frac{jE_0}{\omega\mu}\left[\frac{m}{r} J_m\left(\frac{\alpha_{mn} r}{a}\right) - \frac{\alpha_{mn}}{a} J_{m+1}\left(\frac{\alpha_{mn} r}{a}\right)\right] \cos\left(m\left(\phi \pm \frac{\pi}{4}\right)\right) \cos\left(\frac{z\pi p}{h}\right) \tag{2.31b}$$

$$H_z(r,\phi,z) = 0 \tag{2.31c}$$

Some examples of these modes are shown in Figure 2.13

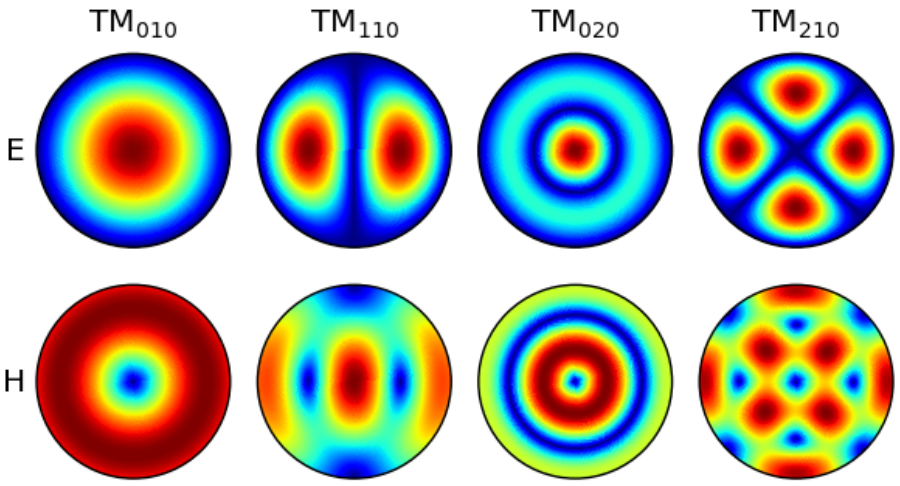


Fig. 2.13 Z slice of electric and magnetic fields of some $TM_{mm0}$ modes

## 2.6 Conclusion

All materials respond in some way when exposed to an electric field, whether that be due to free electrons, stretching of polar molecules, or distortion of the electron cloud around the atoms themselves. The movement of these electrons causes polarization which reduces the electric field within the sample and possibly absorbs some energy from the field. This polarization and loss can be measured by a microwave resonant cavity. The geometry of the cavity sets up standing electric and magnetic fields at certain resonant frequencies. A sample

inserted into a high electric field region will cause a small distortion which can be measured as a change in resonant frequency, and any energy absorbed by the sample will be visible as a change in the bandwidth of the mode. With calibration this change in resonant frequency and bandwidth can be used to calculate the permittivity and loss of the sample.

One common geometry for a resonant cavity is a cylinder. This is particularly suited for cylindrical samples such as powder filled quartz tubes. Using Helmholtz equations the electric and magnetic field patterns of the resonant modes can be calculated. The lowest frequency mode, known as $TM_{010}$ consists of high electric field at the centre of the cylindrical cavity, and high magnetic field at the edges. This is ideal for measuring the electrical properties of samples. Other modes such as $TM_{110}$ have a high magnetic field at the centre, and can be used to measure the magnetic properties of samples.

# Chapter 3

# Temperature Correction Methodology

## 3.1 Introduction

When performing a resonant cavity perturbation experiment a measurement containing the sample is compared against a measurement without the sample. Unfortunately many measurements carried out with the microwave perturbation technique involve a change in temperature such as environmental changes or exothermic/endothermic chemical reactions within the sample [58–61]. Alternatively, the change can be intentional while examining dielectric properties over a range of temperatures. This is an issue since changes in temperature of the cavity can cause thermal expansion of the metal and thus change the geometry. Some existing work has been done by various people [62–65] based on the resonant frequency of an empty cylindrical cavity as a function of its dimensions:

$$f_0 = \frac{c}{2\pi}\sqrt{\left(\frac{k_{mn}}{a(T)}\right)^2 + \left(\frac{p\pi}{l(T)}\right)^2} \tag{3.1}$$

where $c$ is the speed of light, $n$, $m$,and $p$ are the mode integers, $k_{nm}$ is the $n$th root of the $m$th order Bessel function of the first kind for TM modes, and $a(T)$ and $l(T)$ are the temperature-dependent radius and height of the cavity, respectively. As the cavity undergoes a change in temperature, this causes a change in the geometry of the cavity. As described in [64, 65], by using first order partial derivatives, the changes in resonant frequency due to a change in temperature can be seen in (3.2)

$$\frac{\Delta f_0}{f_0} \approx -\alpha_c \Delta T \tag{3.2}$$

where $\Delta T$ is the change in temperature and $\alpha_c$ is the linear thermal expansion coefficient. This equation only accounts for changes in the cavity geometry - the main source of temperature dependent error.

Equation 3.3 is used to correct frequency measurements for temperature changes[64, 65]

$$\frac{\Delta f_s(T)}{f_s(0)} \approx \left[\frac{\Delta f_{010,s}(T)}{\Delta f_{010,s}(0)} - \frac{\Delta f_{m10,s}(T)}{\Delta f_{m10,s}(0)}\right] - \left[\frac{\Delta f_{010,u}(T)}{\Delta f_{010,u}(0)} - \frac{\Delta f_{m10,u}(T)}{\Delta f_{m10,u}(0)}\right] \tag{3.3}$$

where $u$ and $s$ denote the temperature-dependent fractional frequency shift of the unperturbed and perturbed cavity respectively [64, 65]. As (3.2) suggests, any change in temperature causes a proportional change in resonant frequency of the cavity. This change in frequency has the same fractional shift for an ideal cavity regardless of cavity mode. When the sample is present the frequency can be corrected by subtracting the fractional frequency shift of the reference mode from the fractional frequency shift of the measurement mode. This can be seen in the sample related terms in (3.3). The unperturbed terms of this equation are included to remove any errors caused by differences in gradient from the thermal expansion coefficient. These differences are caused by imperfections in the cavity construction and material.

This method, while correct theoretically, introduces unnecessary complexity by depending on this understanding of thermal expansion. The method proposed in section 3.2 takes a more analytical approach to the problem, making use of curve fitting and regression analysis to pick functions that are only as complicated as they need to be.

## 3.2 Simplified Temperature Correction Technique

Almost every microwave resonant cavity perturbation measurement depends on analysing the relative frequency shift between a known sample and an empty cavity. In general we know that the resonant frequency of the sample is some function of the sample temperature and cavity temperature. The resonant frequency of the empty cavity is only a function of the cavity temperature. This can be expressed mathematically as

$$\frac{f_s(T_c, T_s) - f_0(T_c)}{f_0(T_c)} \tag{3.4}$$

Fundamentally, temperature correction is not possible unless the above equation is independent of the cavity temperature, i.e. we can separate the cavity temperature response into it's own function which we call $G$ below

$$\frac{f_s(T_s)\,G(T_c) - f_0 G(T_c)}{f_0 G(T_c)} = \frac{f_s(T_s) - f_0}{f_0} \tag{3.5}$$

This can be verified by measuring a temperature independent sample such as quartz at various cavity temperatures.

The next challenge is calculating the value of $f_0$ to use. The most obvious approact would be to perform a temperature ramp on the cavity while measuring the temperature with a thermocouple or similar instrument to calculate $f_0(T_c)$ over a range of temperatures. When performing the experiment with the sample the temperature is measured throughout, allowing the correct value of $f_0$ to be used for each data point. Unfortunately this has some limitations. Due to the sensitivity of the microwave resonant cavity, a small change in temperature can cause a noticable change in resonant frequency. This requires good precision when measuring the temperature.

An improved approach to temperature correction is to use a resonant mode which is not affected by the sample being measured. Ideally this mode should have zero electric and magnetic field at the sample location. We can then make the assumption that for an empty resonant cavity the following equation always holds true:

$$f_{0,m} = H(f_{0,r}) = H(f_{s,r}) \tag{3.6}$$

where $m$ is the measurement mode, $r$ is the reference mode, $f_0$ and $f_s$ are the empty and sample states respectively, and $H$ is an arbritrary repeatable function. We can then substitute this equation back into the relative frequency shift equation 3.4 to obtain the following:

$$\frac{f_{s,m} - H(f_{s,r})}{H(f_{s,r})} \tag{3.7}$$

Using linear curve fitting and regression analysis, the function $H$ can be chosen to be as simple or as complicated as required.

### 3.2.1 Experimental Verification

To verify this theory we can use a sample whose dielectric properties change little with temperature. Clear fused quartz is a common choice. Two measurements were performed with a microwave resonant cavity placed inside of a temperature controlled oven. The first measurement contained an empty quatz tube, and the second added a quartz rod inside

the tube. Both measurements were swept from 30 °C to 70 °C over 1 hour with a dwell at the top for 30 minutes. The temperature was then ramped back down to 30 °C over 1 hour with another 30 minute dwell at the bottom. This ramp was performed twice for each measurement. For both samples the modes $TM_{010}$ and $TM_{210}$ were measured. $TM_{010}$ is the measurement mode which is affected by the sample, and $TM_{210}$ is a reference mode which is not affected by the sample.

Using the theory explained in section 3.2, firstly the function $H(f)$ needs to be calculated. This is achieved by fitting a curve to the plot of $TM_{210}$ against $TM_{010}$ for the empty tube measurement. The plot and fit for this experiment is shown in figure 3.1:

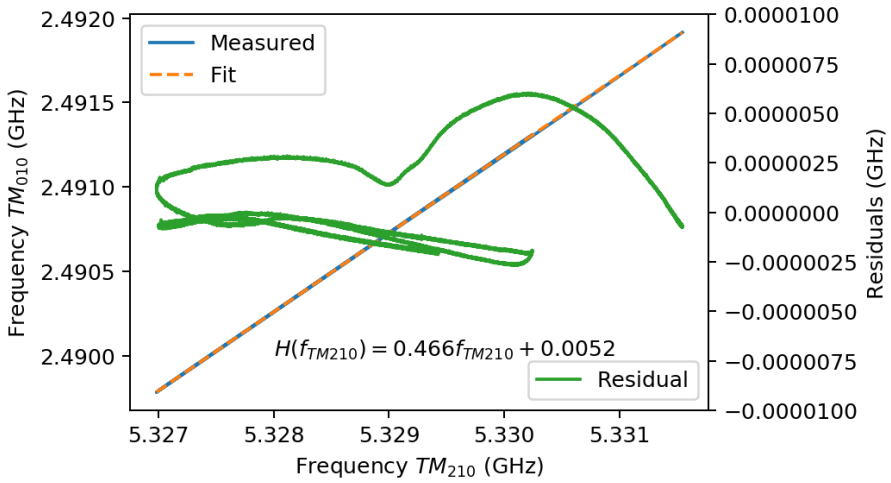


Fig. 3.1 Plot of $TM_{210}$ against $TM_{010}$ with 1st order linear curve fit. The residuals scale is 10x smaller than the frequency scale.

As you can see by the residuals, a 1st order linear fit is more than adequate for relating $TM_{210}$ to $TM_{010}$. If the residuals were sigificant then a 2nd order fit could be considered. This may be the case with stronger coupling where the temperature change of the coupling loops becomes significant too.

This can be compared to the plot of temperature against $TM_{010}$ in figure 3.2 which, although not terrible across a range of 40°C, does become limited in its ability to correct for small ambient temperature changes. The main issue is the hysterysis caused by the measurement thermocouple being placed on the outside of the microwave resonant cavity. This results in a delay between the cavity temperature changing and the thermocouple detecting that change.

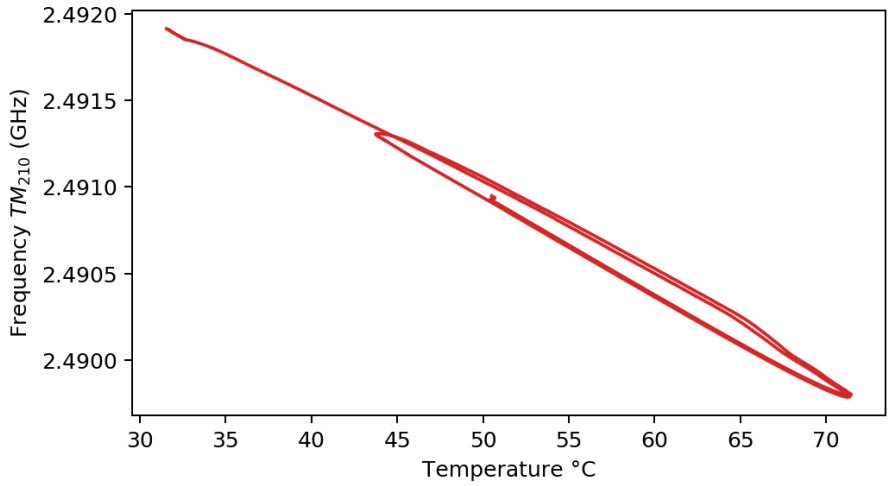


Fig. 3.2 Plot of temperature against $TM_{010}$

This function $H(f)$ can now be used to perform temperature correction on a quartz rod measurement using equation 3.7. The result of this correction is shown in figure 3.3.

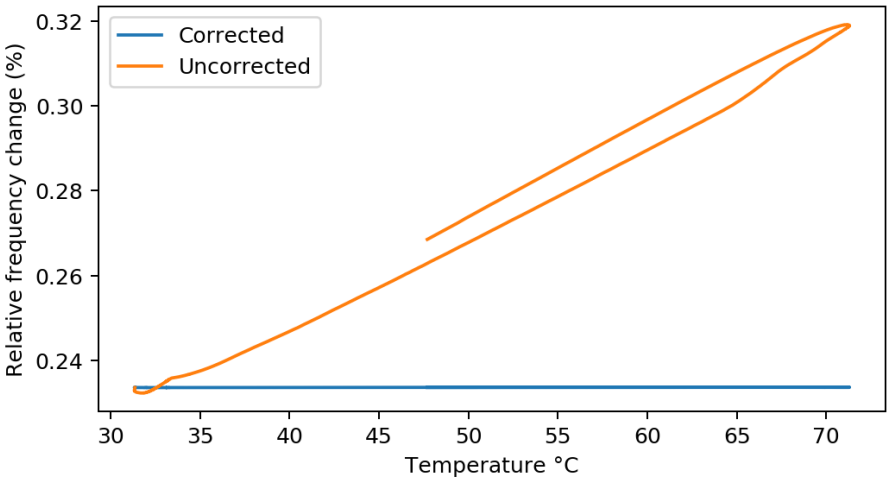


Fig. 3.3 Temperature corrected and uncorrected measurement of a quartz rod from 32°C to 74°C

As can be seen the temperature correction eliminates almost all of the measured fractional frequency shift. For a sample as stable as a quartz rod, this is the expected result. The hysterysis in the uncorrected result is again caused by delayed thermocouple response.

As a bonus, this quartz rod measurement can be used to calibrate the effective cavity volume in equation 2.23 based on the known permittivity of quartz, the volume of the quartz rod, and the relative frequency shift.

### 3.2.2 Simulation Verification

The algorithm can also be verified using a simulation. A COMSOL model was created using geometry similar to that shown in figure 3.4, but only including internal walls and scattering boundary conditions where there are holes in the cavity. The temperature change was simulated by scaling the microwave cavity proportional to the thermal expansion coefficient of aluminium.

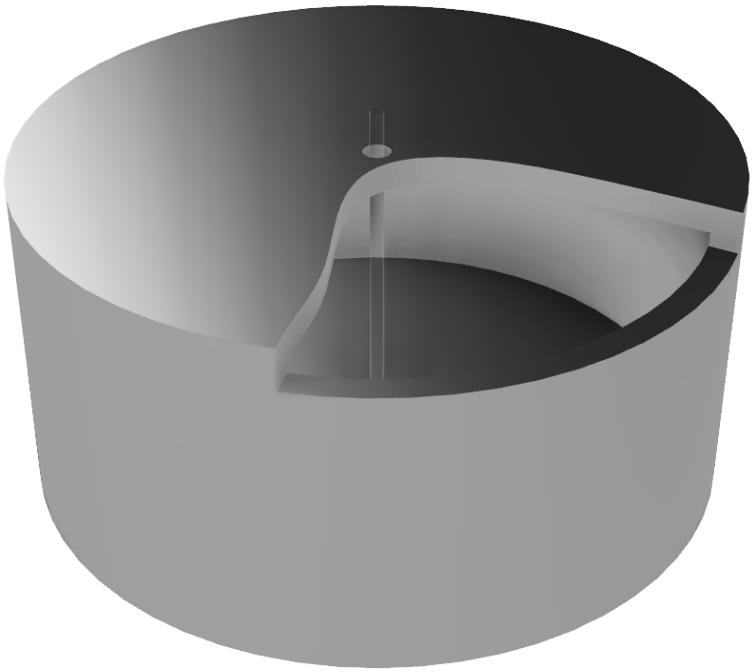

Fig. 3.4 Cutaway view of the microwave cavity and sample used in the COMSOL simulation

When first order linear fitting $TM_{210}$ against $TM_{010}$ without a sample, the residual is at most 3kHz which is very small compared to the resonant frequencies. Applying the temperature correction algorithm described above results in the following figure:

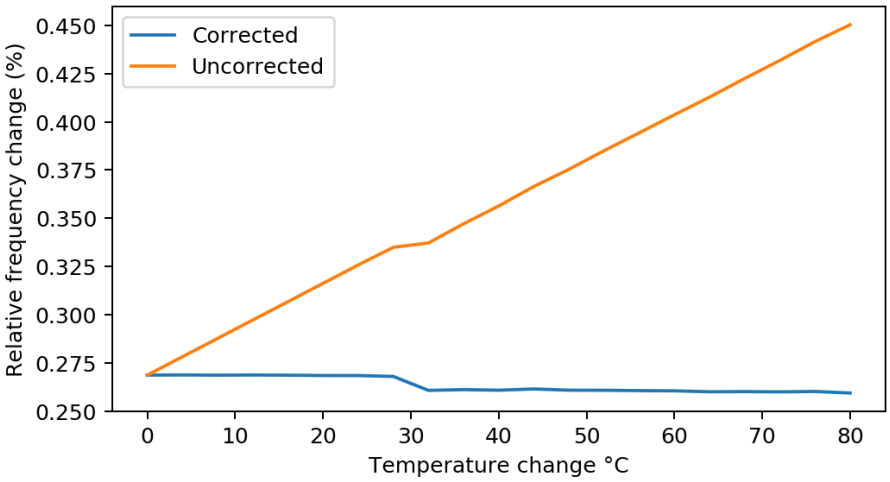


Fig. 3.5 Uncorrected and corrected permittivity of the simulated sample

Besides the artifact of the parameter sweep simulation, the temperature correction has again been effective in removing any changes in resonant frequency caused by thermal expansion of the microwave cavity. A possible cause of this artefact is two different datasets being used in COMSOL at different temperature ranges which don't quite align correctly.

## 3.3 Temperature Correction Using Degenerate Modes

The following work was done in collaboration with co-workers [14]. In the previous section the $TM_{210}$ was used successfully to temperature correct a quartz rod measurement. Cylindrical or cubic host resonators offer another unique way of accounting for temperature variation using the fact that some of their modes are degenerate. This is where some of their modes have the same frequencies, but different field orientations. Referring back to equation 2.29 of chapter 2 it can be seen that the $TM_{m10}$ modes where $m > 0$ have two possible simultaneous orientations. This is illustrated in figure 3.6:

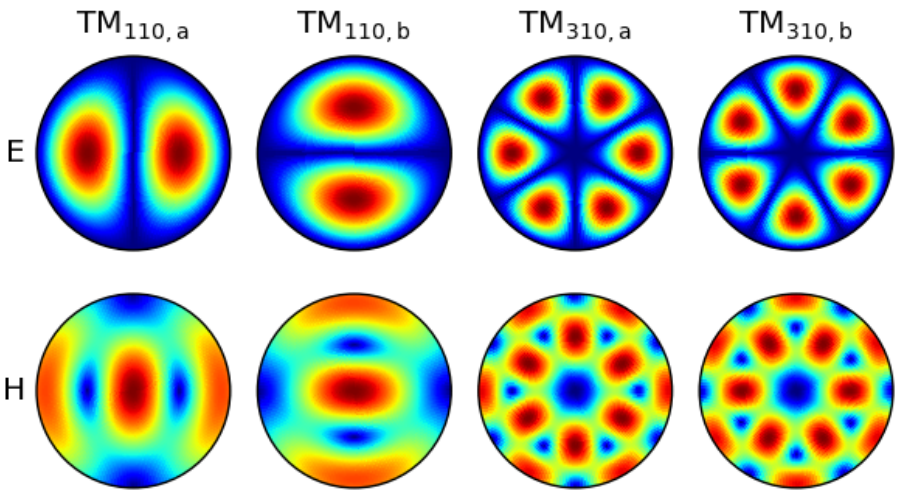


Fig. 3.6 Electric field (E) and magnetic field (H) patterns for the degenerate $TM_{110,a}$, $TM_{110,b}$, $TM_{310,a}$, and $TM_{310,b}$ modes.

With a perfectly symmetrical cylindrical microwave cavity, the spatial orientations of the $TM_{m10}$ modes result in exactly the same frequency, thus yielding a single Lorentzian response. Distortion or splitting of the Lorentzian response can occur when the frequencies are unequal. This can happen when the azimuthal symmetry of the cylindrical cavity is broken, such as with a split in the cavity construction in the vertical plane, or where there are holes in the cavity. These ideal and practical scenarios can be seen in figure 3.7 along with the orientation of $TM_{110,a}$ and $TM_{110,b}$ modes.

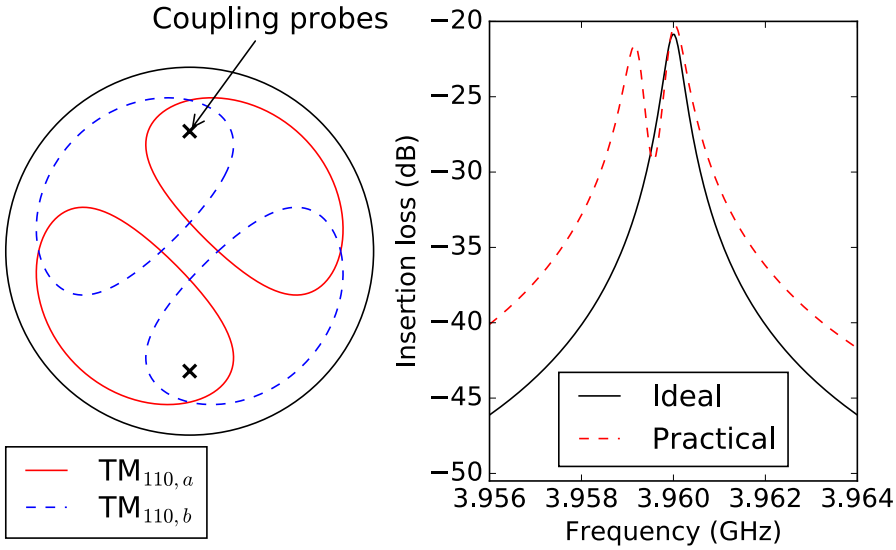


Fig. 3.7 Schematic contour plot of the electric field magnitude for the $TM_{110}$ mode with capacitive (i.e. E field) coupling probes, located as shown for a transmission measurement (left). Measured transmitted power $|S_{21}|^2$ in the frequency domain of the $TM_{110}$ mode in a cavity split in the vertical plane in the ideal case (black solid) and in the practical case (red dashed).

In the practical scenario it is difficult to extract Lorentzian curve parameters from the $TM_{110}$ mode due to the distortion of the Lorentzian peak. A perturbation can be positioned to maintain equal coupling between the two modes while also increasing separation between the $TM_{110,a}$ and $TM_{110,b}$ modes. If the perturbation is large enough to ensure sufficient separation, then the unperturbed $TM_{110}$ mode can be used for temperature correction.

### 3.3.1 Proposed Use of Degenerate Modes

Degenerate TM modes can be used with temperature correction by placing the sample to be measured off-axis, causing the degenerate mode frequenies to split. The placement of the sample must be chosen to ensure both modes are coupled to equally. For modes $TM_{110}$ and $TM_{310}$ used in this experiment, the sample is inserted at an angle of 45° from the coupling structures, however this results in $TM_{210}$ and $TM_{410}$ being unusable. This is shown in figure 3.8.

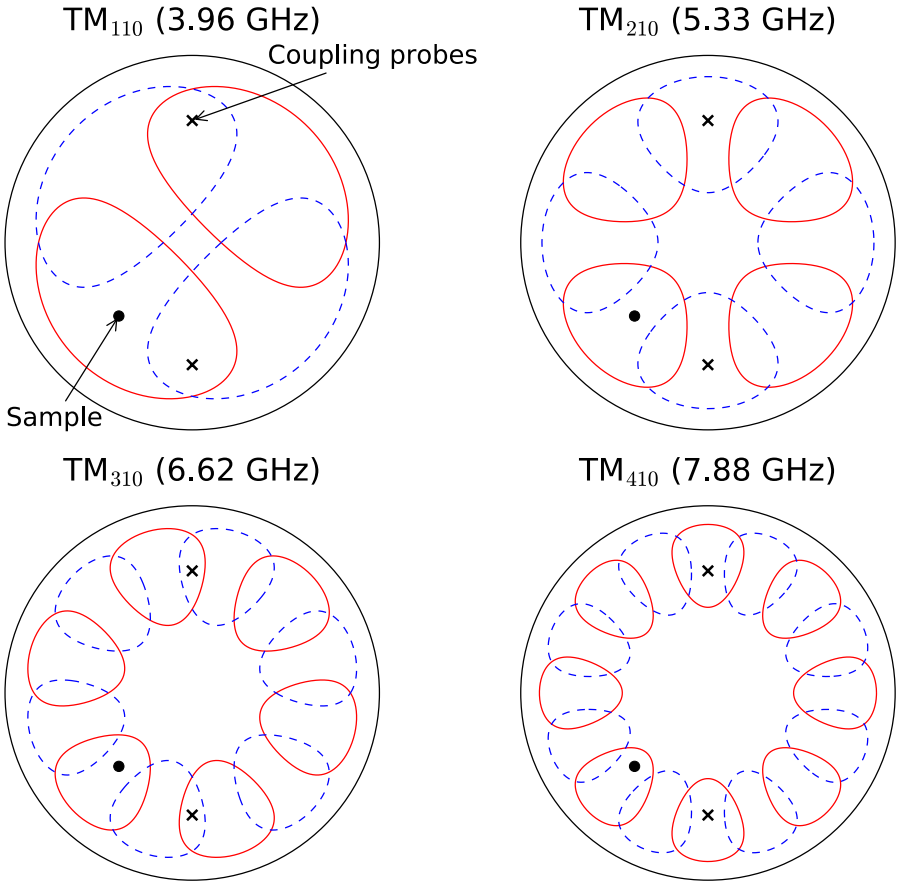


Fig. 3.8 Contour plots of $TM_{m10}$ modes. $TM_{110}$ and $TM_{310}$ have equal coupling between the perturbed and unperturbed modes. Only the unperturbed $TM_{210}$ mode is coupled, and only the perturbed $TM_{410}$ mode is coupled.

This perturbation locks the orientation of the modes. One of the modes will be perturbed by the sample and thus will have a lower frequency. This lower frequency mode becomes the measurement mode and is referred to as $TM_{m10,a}$. The higher frequency of the two modes will not be affected by the introduction of the perturbing sample. This unaffected mode becomes the reference mode and is used for temperature corrections. This mode is referred to as $TM_{m10,b}$.

Due to the geometry of the modes, not all of them can be coupled equally at once. Placing the sample at 45° from the coupling probes allows use of the $TM_{110}$ and $TM_{310}$ modes. $TM_{210}$ and $TM_{410}$ are unusable due to them only coupling the unperturbed and perturbed mode respectively. Either of the temperature correction techniques discussed earlier in this chapter can be used, except the measurement and reference modes are replaced with $TM_{m10,a}$ and $TM_{m10,b}$ modes, respectively.

Using this technique the sample is placed in the region of high electric field and notionally zero magnetic field of the measurement mode $TM_{m10,a}$. When considering the fields of the reference mode $TM_{m10,b}$ the sample is in a region of low electric field but high magnetic field. As described at the beginning of this chapter, in order for this technique to work for any material the reference mode must have no magnetic of electric field at the sample location. Due to this the degenerate mode temperature correction technique described may only be used on samples which are non-magnetic.

### 3.3.2 Method and Results

These experiments were conducted using an aluminium microwave cavity resonator designed for TM measurements with capacitive antenna coupling into the E-field. Measurements were taken using the $TM_{110}$ mode configuration shown in Figure 3.8. The $TM_{310}$ mode was not used due to interference from another mode with similar resonant frequency.

The temperature was controlled by placing the resonant cavity in a Memmert IPP400 temperature controlled oven. The Voltage transmission coefficient ($S_{21}$) measurements were obtained using Keysight Technologies Vector Network Analyser (VNA) (PNA-L N5232A) with RF cables from Huber+Suhner. The VNA was connected to a PC running an in-house measurement acquisition program built with LabVIEW. The program also measures the temperature of the cavity using an Omega PT100 temperature sensor connected to a National Instruments (NI) cDAQ-9171. This is shown in Fig. 3.9.

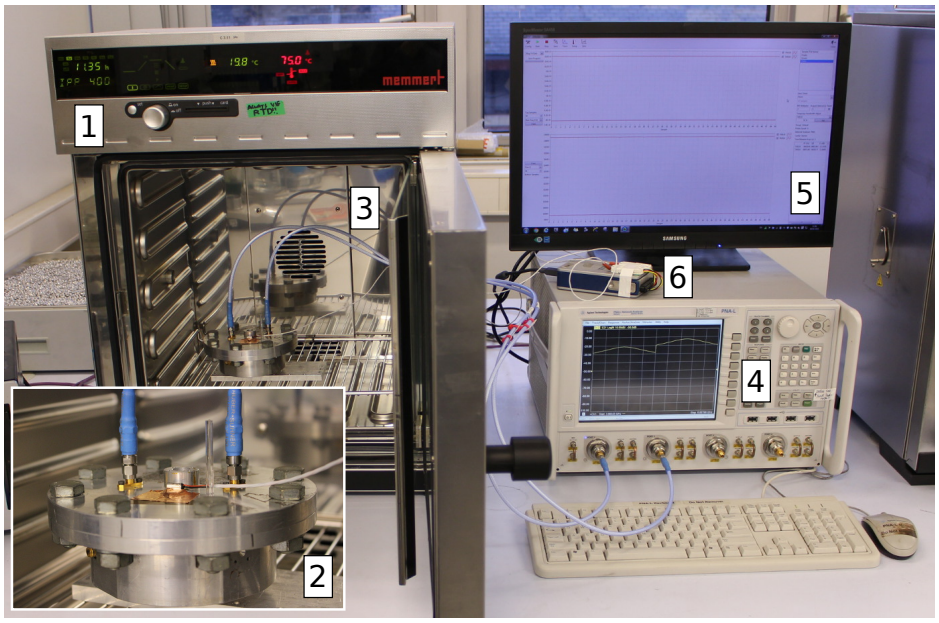


Fig. 3.9 Experimental setup showing the temperature controlled oven (1) containing the microwave cavity resonator with inserted sample and attached temperature sensor (2). Coaxial cables (3) connect the cavity to the VNA (4) which is being driven by the LabVIEW measurement acquisition program (5). The temperature sensor is connected to the NI-DAQ (6), also controlled by the same program.

The experiment consisted of two temperature ramp measurements, one with empty quartz tubes, and the other with the addition of a water sample. Two nested quartz tubes were used. The outer tube has an outer diameter of 4.0 mm and inner diameter of 2.0 mm. The inner tube has an outer diameter of 0.4 mm and inner diameter of 0.3 mm. The purpose of the outer tube was to split the high and low $TM_{110}$ modes enough to treat them as separate modes and reliably extract the frequency and Q factor. The inner tube is used as a container for a small volume of water. The frequency response showing the separation of these modes can be seen with and without the water sample in Figure 3.10.

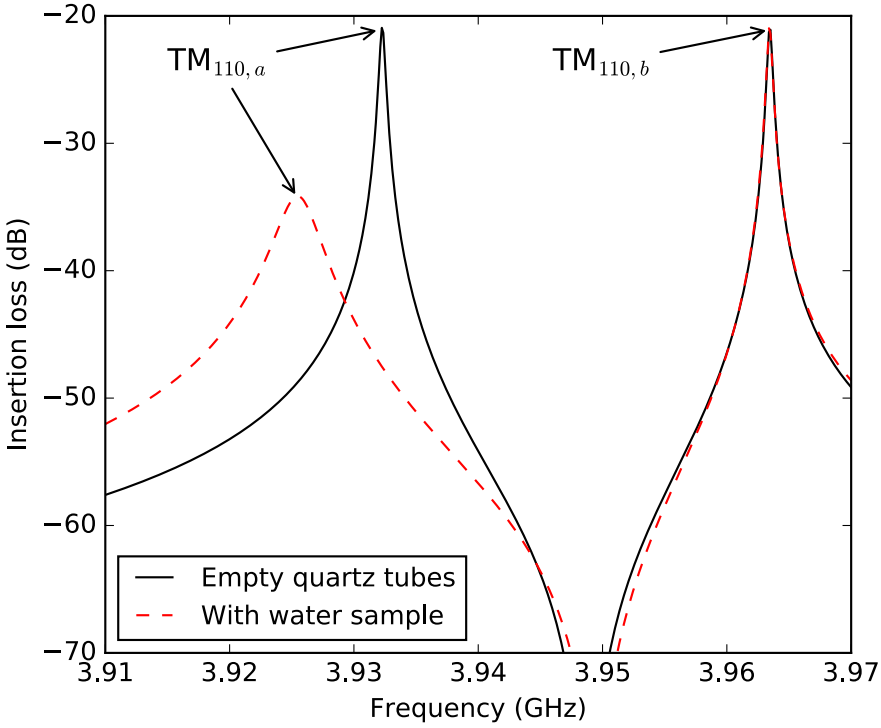


Fig. 3.10 Measured transmitted power $|S_{21}|^2$ in the frequency domain of the $TM_{110}$ mode when perturbed by the empty quartz tubes (black solid) and when a water sample is added (red dashed).

The temperature ramps were performed from 20 °C to 60 °C over 8 hours, then returning to 20 °C at the same rate. Both the measurement mode $TM_{110,a}$ and reference mode $TM_{110,b}$ were measured for the empty and water ramps. The frequency results of these measurements are shown in figure 3.11.

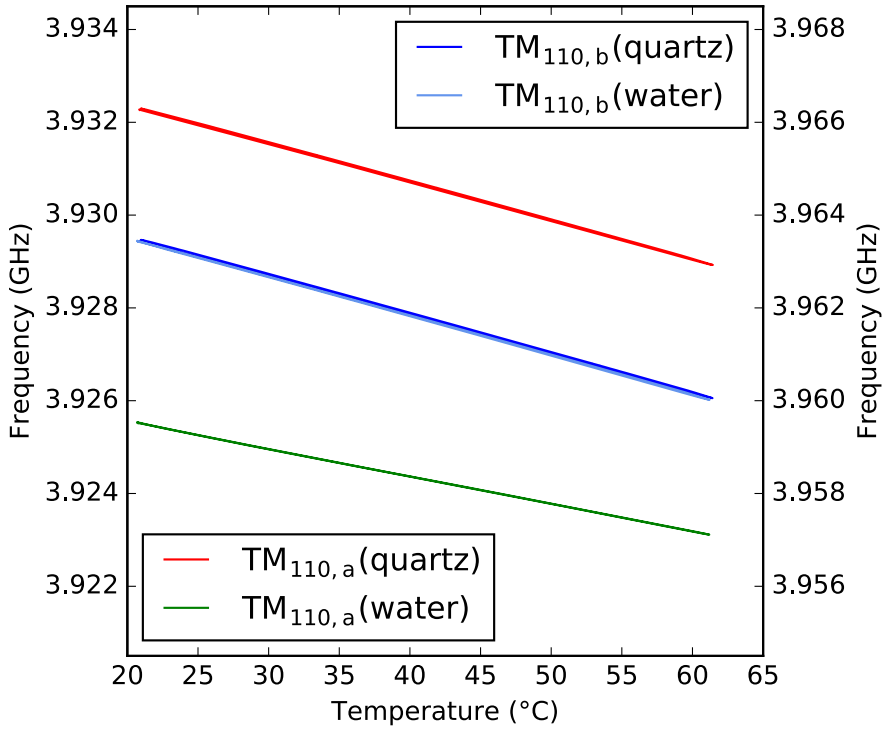


Fig. 3.11 $TM_{110}$ measured frequency versus temperature with measurement modes on the left axis and reference modes on the right axis. The two reference measurements are almost identical as expected.

Frequency results show the reference mode $TM_{110,b}$ is not affected by presence of the sample. The measurements for the $TM_{110,a}$ mode have different resonant frequencies for water and quartz due to the addition of water affecting the perturbation. These measurement modes also have different gradients. The gradient in the quartz tubes is caused predominantly by the change in cavity temperature as the permittivity of quartz has very little temperature dependence. The gradient of the water containing sample has the same contribution from temperature change of the cavity and quartz but also a contribution due to the temperature dependence of permittivity for water. Before temperature correction of the water sample, the frequency decreases as temperature increases. This trend is the opposite of the expected result. To resolve this, the modified temperature correction technique is used to remove the contributions from the cavity and quartz tubes, as well as reduce the errors present. This method ensures that after correcting these values, the only changes in observed frequency are due to changes in the permittivity of water. The real permittivity of water is calculated using equation 2.23 before and after temperature correction of frequency has been carried out. This can be seen in figure 3.12.

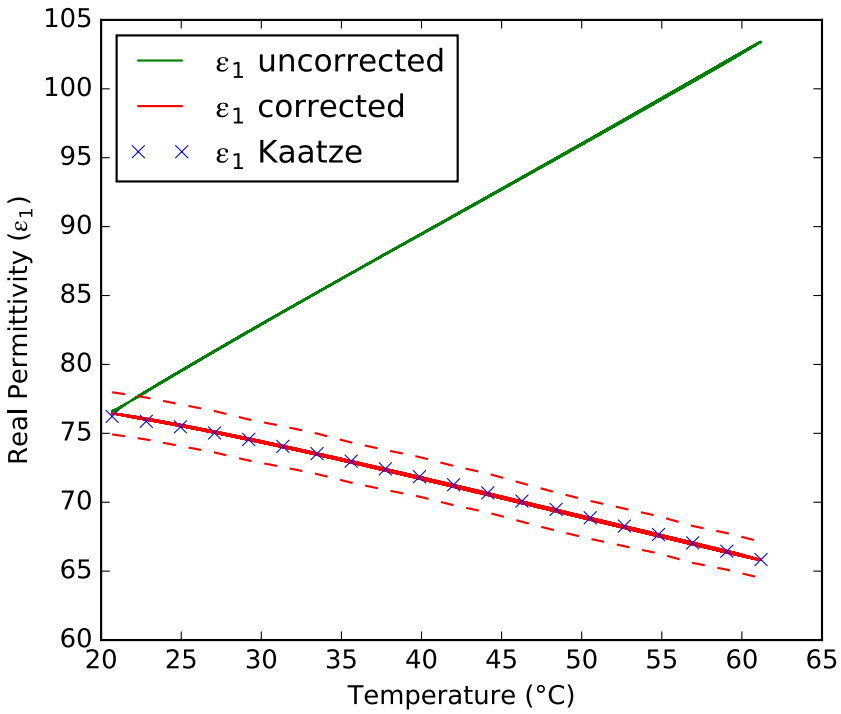


Fig. 3.12 Corrected, uncorrected and literature values for real permittivity ($\varepsilon_1$) of water at 4 GHz versus temperature with 2% systematic error indicated by the dotted lines.

Real permittivity values shown in figure 3.12 show that before temperature correction the graph suggests a rise in permittivity of the water sample as temperature increases. Once this data has been corrected, a decrease in real permittivity can be seen between 20 °C and 60 °C. This corrected negative gradient and corresponding $\varepsilon_1$ values now closely match the literature values calculated from the equations developed by Kaatze [66]. This also matches closely with the values seen in literature [67, 68]. The errors for these measurements were also calculated and compared with the literature values as shown in table 3.1.

| T (°C) | $\varepsilon_{1,Kaatze}$ | $\varepsilon_{1,measured}$ | Percentage difference |
|---|---|---|---|
| 25.0 | 75.46 | 75.54 | 0.11% |
| 30.0 | 74.37 | 74.43 | 0.08% |
| 35.0 | 73.14 | 73.04 | -0.13% |
| 40.0 | 71.82 | 71.67 | -0.21% |
| 45.0 | 70.44 | 70.27 | -0.24% |
| 50.0 | 69.03 | 68.91 | -0.17% |
| 55.0 | 67.60 | 67.49 | -0.17% |
| 60.0 | 66.18 | 66.18 | 0.01% |

Table 3.1 Comparison of Experimental Measurements Versus Literature Values of the Permittivity of Water at 4 GHz.

The main systematic errors accounted for include the permittivity and volume of the calibration quartz rod, and the volume of the water sample. These are approximately 2%. The random errors were negligible in comparison, less than 0.1%. As the table shows, the experimental results were well within the systematic error when compared against the literature permittivity values.

## 3.4 Conclusion

The temperature of a microwave resonant cavity can affect its resonant frequency due to thermal expansion of the metal. This can lead to unwanted systematic errors when measuring samples over a range of temperatures. Some work has been done previously based on this thermal expansion and how it affects the cavity geometry and in turn the resonant frequency. In this chapter a simpler method is proposed which takes an analytical approach. A curve fit is calculated between the reference and measurement resonant modes with an empty cavity. During a measurement the same reference mode can then be used to calculate what the empty resonant frequency would be at each sample point. This can then be used in the standard fractional frequency shift equations for calculating permittivity.

Another novel method was also described involving split degenerate modes. Some cylindrical resonant modes have two overlapping fequencies where the field patterns of one are a rotation of the other. This can be exploited by strategically placing a sample off-axis. This splits the

frequencies of the two degenerate modes apart far enough such that one can be used as a measurement mode, and the other as a reference mode. This technique was verified using water which showed very good correlation with the expected permittivity values found in the literature.

# Chapter 4

# Instrument Control Software

This thesis focuses heavily on simultaneous microwave measurements of samples while being exposed to external conditions. To reduce the amount of manual work required, and to improve repeatibility of experiments, a solution is required to automate the control of an arbritrary set of instruments. These instruments can include (but are not limited to) Vector Network Analysers (VNAs), DC power supplies and temperature probes. It should be as simple as possible to write drivers for additional instruments as required.

For the VNA measurements it's necessary to be able to divide the frequency sweep into discrete segments, each corresponding to a different mode of the microwave resonant cavity. Also the system should handle scenarios where the resonant frequency shifts outside of the current measurement window, and adjust the window accordingly. If it is still possible to track the Lorentzian peak then this adjustment is trivial, however if the resonant peak has shifted far enough that it can no longer be recognised then a more robust tracking algorithm is required.

Similarly the measurement window should be adjusted to ensure an adequate "zoom" on the Lorentzian peak. If only a small part of the peak can be seen then the visible curve may be too flat to achieve a precise curve fit. Also small frequency shifts will quickly move the peak outside the measurement window. On the other hand if the measurement window is too large then there may not be enough data points in the vincinity of the resonant peak, again reducing the precision of the measurement.

## 4.1 Existing solutions

This section summarises the existing solutions that are easily available and their limitations that resulted in a custom solution being written.

### 4.1.1 Standalone VNA

While all the solutions following this also require a VNA, is is possible to perform some limited measurements without any external system. For single datapoints the VNA can be configured to perform an $S_{21}$ measurement of the resonant cavity and optionally extract the frequency and bandwidth of the resulting Lorentzian curve using markers. These values can then be written down by hand, or the data exported to a memory stick to be processed offline.

Unfortunately a standalone VNA is limited in its ability to perform continuous time dependent measurements. On some models it is possible to write VBA scripts on the VNA itself, however this is still limited with regards to visualising the data in realtime and an inability to control external equipment such as power supplies, temperature probes etc.

### 4.1.2 Basic Track software

This is a basic cavity perturbation software which has been developed iteratively by various students at Cardiff University [60, 69]. Its simplicity allows it to be easily modified to add extra functionality such as control of additional instruments, however it has no capability of choosing the set of instruments based on a configuration file, so multiple versions of the program are required based on the experiment being performed.

### 4.1.3 Cardiff Cavity Perturbation (CCP)

This software was written in house in LabVIEW [59]. It has support for both ENA and PNA Keysight network analysers as well as temperature measurements from thermocouples attached through a National Instruments DAQ.

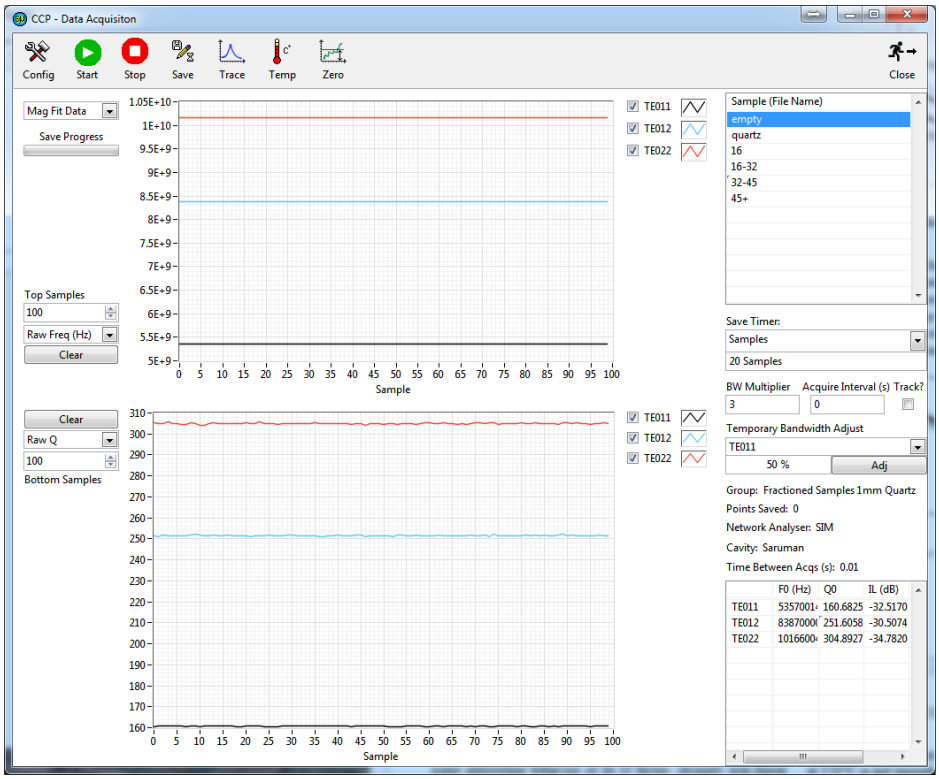


Fig. 4.1 Main acquisition window of the Cardiff Cavity Perturbation (CCP) software.

Unfortunately this software didn't have any support for additional instruments such as DC power supplies. It also relied on National Instruments' own TDMS format which can be slow and memory usage heavy when processed using familliar data analysis techniques in Python. As an example, a datafile for an overnight experiment expanded to approximately 14GB in RAM when loaded into Python.

## 4.2 Software Architecture

Based on the analysis of existing software solutions the decision was made to write a new software package using Python. Python was chosen due to my familliarity with the programming language.

Before any low level implementation details are analysed a high level architecture must be designed first. This architecture has a few requirements. Each instrument should be able to update and produce data at its own speed, and not block any other instruments from updating. The user interface updating must also be limited as to not consume too much CPU time.

The architecture that was decided upon involved creating a separate thread for each instrument, and another main thread for the user interface and datalogging. To link the instrument threads to the UI thread, queues were used to buffer the data between them. Figure 4.2 shows an overview of the architecture.

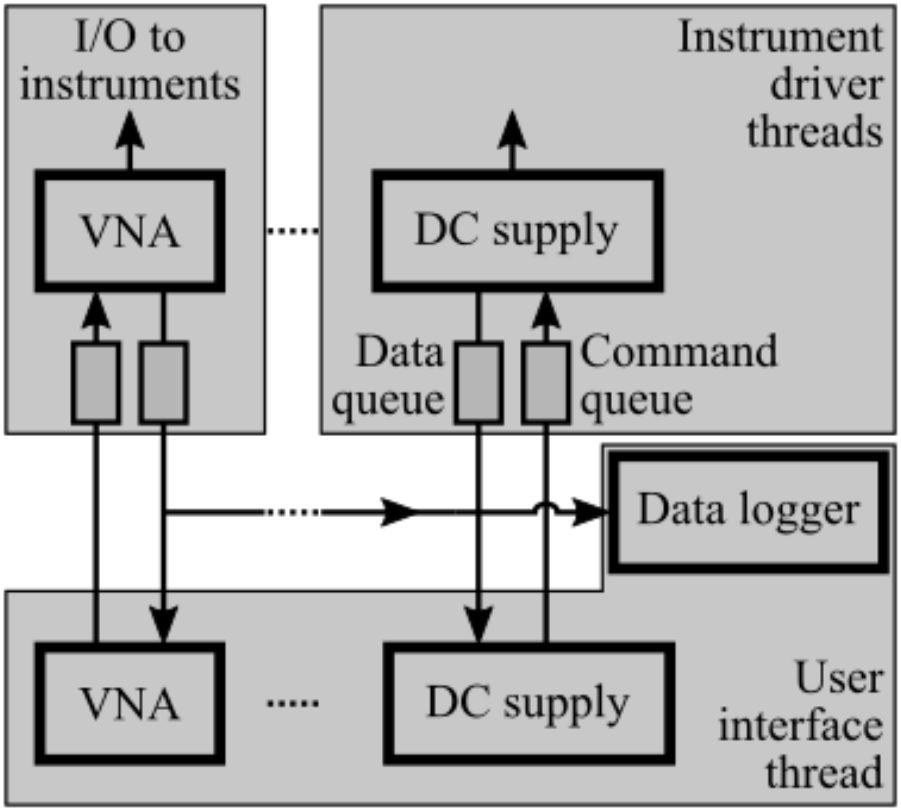


Fig. 4.2 Archtecture of the instrument control software showing two instruments and the data flow between the user interface and driver threads.

Although data logging could also be considered as blocking, it was deemed that the impact on the user interface would be imperceptible, and so it was acceptable to share the same thread. An alternative solution would be to move data logging to the same thread as the instrument it belongs to, however the instrument driver threads are more sensitive to small delays that could be caused when writing data to disk.

A backend system, not shown in the figure above, orchestrates the whole program including loading configuration files, starting/stopping the instruments and starting/stopping the data logger. The user interface then sits on top of the backend and calls appropriate methods based on user actions. The user interface can also subscribe to receive updates whenever an instrument generates new data. This is used to update graphs and other realtime data views.

When the program is first started, a configuration file needs to be loaded or created. These are files in the .json format. They contain a list of the sample names as well as a dictionary of instruments. Each instrument has a user assigned name, for example vna0, and the configuration which includes the type of instrument. The associated instrument driver knows how to interpret the specific configuration data such as the initial centre frequency and bandwidth of the segments to sweep.

Once a configuration is loaded the experiment can be started. This starts up one thread for each instrument. The data acquired by each instrument is stored into a queue and periodically the main thread will empty this queue and record it to a file if data logging is enabled. This data is also used up update any realtime graphs. The main user interface also has the ablility to change the instrument configuration whilst it's running. This is achieved by submitting a command to the command queue of the instrument. The instrument driver thread will periodically read and execute any commands in this queue.

The user interface for the instrument control software is powered by a library called Qt5. This library is originally written for C++, however it has bindings written to support Python. The main advantage of using Qt5 is the ability to quickly design user interfaces using a drag and drop software called Qt Designer. An example showing the design of the main window is shown in figure 4.3.

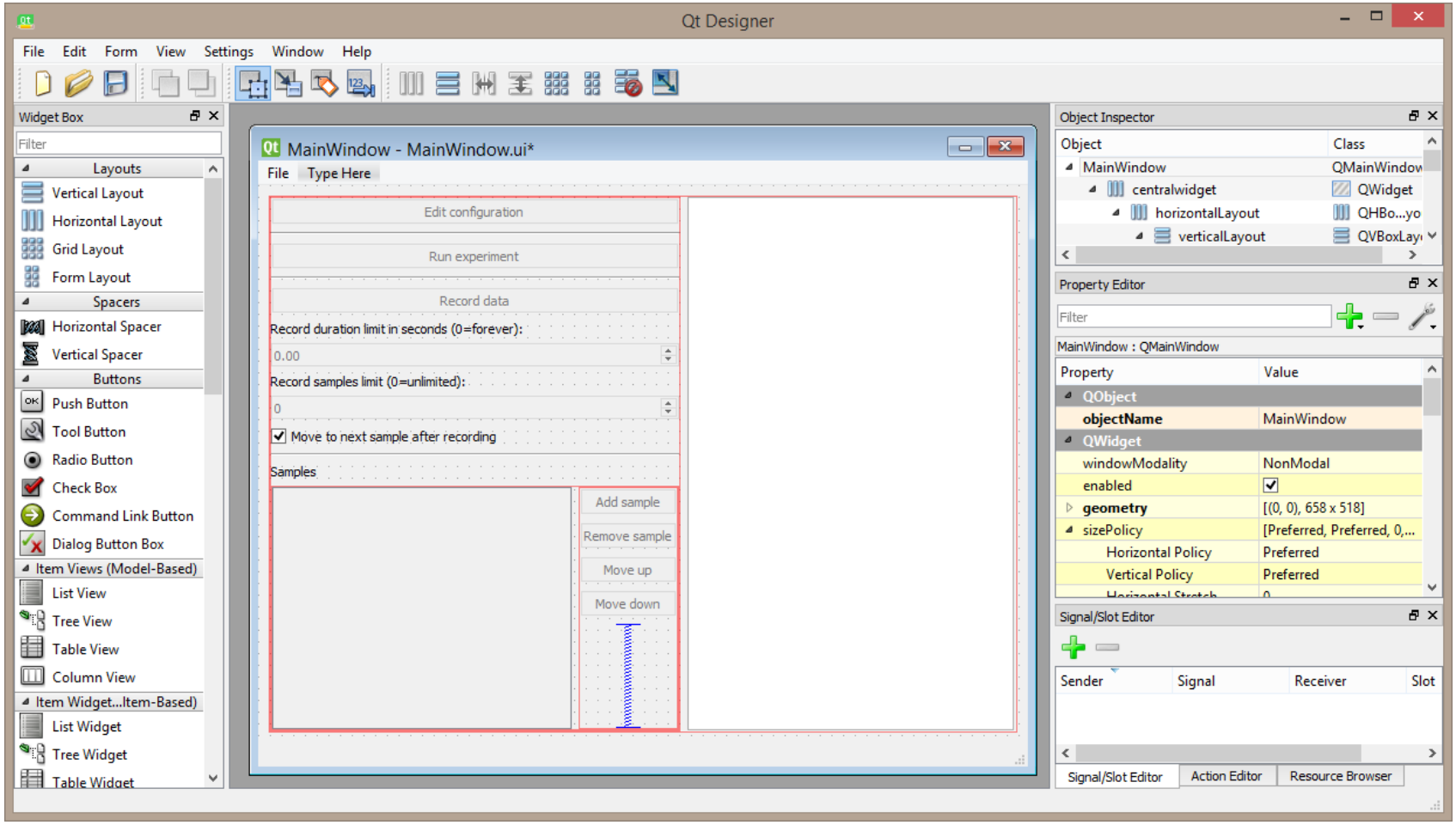


Fig. 4.3 Design of the main window using Qt Designer.

Once the user interface has been designed it can then be exported to a .ui file which internally is an XML file describing the layout. This can then be read by Python at runtime, and the functionality of the user interface can be implemented. The user interface could also theoretically be created entirely in Python, however separating the design from the function allows the visual appearance to be changed quickly without modifying any code.

## 4.3 VNA Driver

The vector network analyser driver is designed to track and record the parameters of one or more resonant modes of a microwave cavity resonator. This involves setting the centre frequency and span of the segments to track, reading the $S_{21}$ power, and fitting the curve to a lorentzian to extract resonant frequency, Q factor and insertion loss.

Currently the driver can support the E5071B/C and N5232A network analysers from Keysight as well as the S5085 USB network analyser from Copper Mountain.

To communicate with the network analysers an API called the Virtual Instrument Software Architecture (VISA) is used. The commands sent over this API are called Standard Commands for Programmable Instruments (SCPI). For the Keysight network analysers these commands are sent as plain text through the PyVISA library. The S5085 network analyser uses Microsoft's Component Object Model to send these commands.

Th method of configuring and communicating with the network analysers is similar between all of the supported models. The first step is to configure the measurement mode, triggering and sweep mode. This is shown in listing 4.1:

Listing 4.1 SCPI commands for network analyser initialisation

```
:CALC1:PAR1:DEF "S21"
:INIT1:CONT ON
:TRIG:SOUR BUS
:SENS1:SWE:TYPE SEGM
:SENS1:SWE:DELAY 0.001
:SENS1:SWE:GEN STEP
```

The segments to sweep then need to be configured. For the E5071B/C this is achieved with the :SENS1:SEGM:DATA <value> command where <value> is a list containing the centre frequency, span, points, IF bandwidth and power for each segment. Following the segment configuration, the main acquisition loop can begin. This involves triggering the instrument, waiting for data to become avaliable, reading the raw frequency and amplitude data, then

fitting the data to a Lorentzian curve. The loop can also reconfigure the frequency sweep ranges if the Lorentzian drifts too far from the centre of each segment.

The sweep window is set such that span of the sweep is some multiple of the bandwidth called the bandwidth factor. The resonant frequency is kept close to the centre frequency of the sweep. If either of these parameters fall outside a specified error then a retrack is triggered recentering and rescaling the curve. Listing 4.2 shows how this algorithm is implemented in Python:

Listing 4.2 Window tracking algorithm

```
def track_window(center, span, f0, bw, center_err=0.5,
                 span_err=0.3, bw_factor=8.0):
    #Ensure +-3dB bw markers stay within center_err of window
    ferr = math.fabs(center-f0) + bw/2
    retrackf = ferr > span*center_err*0.5

    #Ensure span is within span_err% of bw*bw_factor
    retracks = (bw*bw_factor)/span > 1 + span_err
    retracks = retracks or span/(bw*bw_factor) > 1 + span_err

    return retrackf, retracks
```

Sometimes it's possible that a change in the resonant frequency happens faster than the sample rate and the lorentzian peak is lost. In this instance the slope of the curve is calculated using a linear regression and the centre frequency is shifted in the direction of increasing amplitude.

In order to extract the resonance parameters from the raw $S_{21}$ data, a non-linear least squares cure fitting is used. The curve fitting was found to work best when the parameters were small, so the raw data is first scaled to a 0..1 range on both frequency and amplitude axes before being fit. The resulting frequency, bandwidth and insertion loss are then scaled back up to the original range. This algorithm is shown in listing 4.3:

Listing 4.3 Lorentzian curve fitting methods

```
import numpy as np
from scipy.optimize import curve_fit

def lorentz_fn(x, f0, bw, pmax, skew):
    return (pmax + skew*(x-f0))/np.sqrt(1 + (4*((x-f0)/bw)**2))
```

```
def lorentz_fit(freq, ampl, f0=0.5, bw=0.5, pmax=1.0, skew=0.0):
    # This converts lists into numpy arrays
    freq = np.array(freq)
    ampl = np.array(ampl)

    maxa = np.max(ampl)
    norma = ampl/maxa
    weights = norma*norma

    minf = np.min(freq)
    maxf = np.max(freq)
    fspan = maxf-minf
    normf = (freq-minf)/fspan

    (f0, bw, pmax, skew), pcov =
        curve_fit(lorentz_fn, normf, norma, (f0, bw, pmax, skew))

    f0 = (f0*fspan)+minf
    bw = np.fabs(bw)*fspan
    skew = (skew/fspan)*maxa
    pmax = 20*np.log10(pmax*maxa)
    return bw, f0, f0/bw, pmax, skew
```

An alternative algorithm is also provided when speed of acquisition is more important than accuracy of fitting. Instead of retrieving the full sweep data from the VNA, the 3dB and center frequency markers are tracked and returned instead. This reduces the amount of data required to be sent over USB, but also removes the need to synchronise the sweep on the VNA with the acquisition of data. The synchronisation is required to prevent partial sweeps from being returned, however with markers this is not an issue as markers are only ever recalculated at the end of a sweep.

### 4.3.1 User Interface

The main user interface to control and monitor the VNA is shown in Figure 4.4.

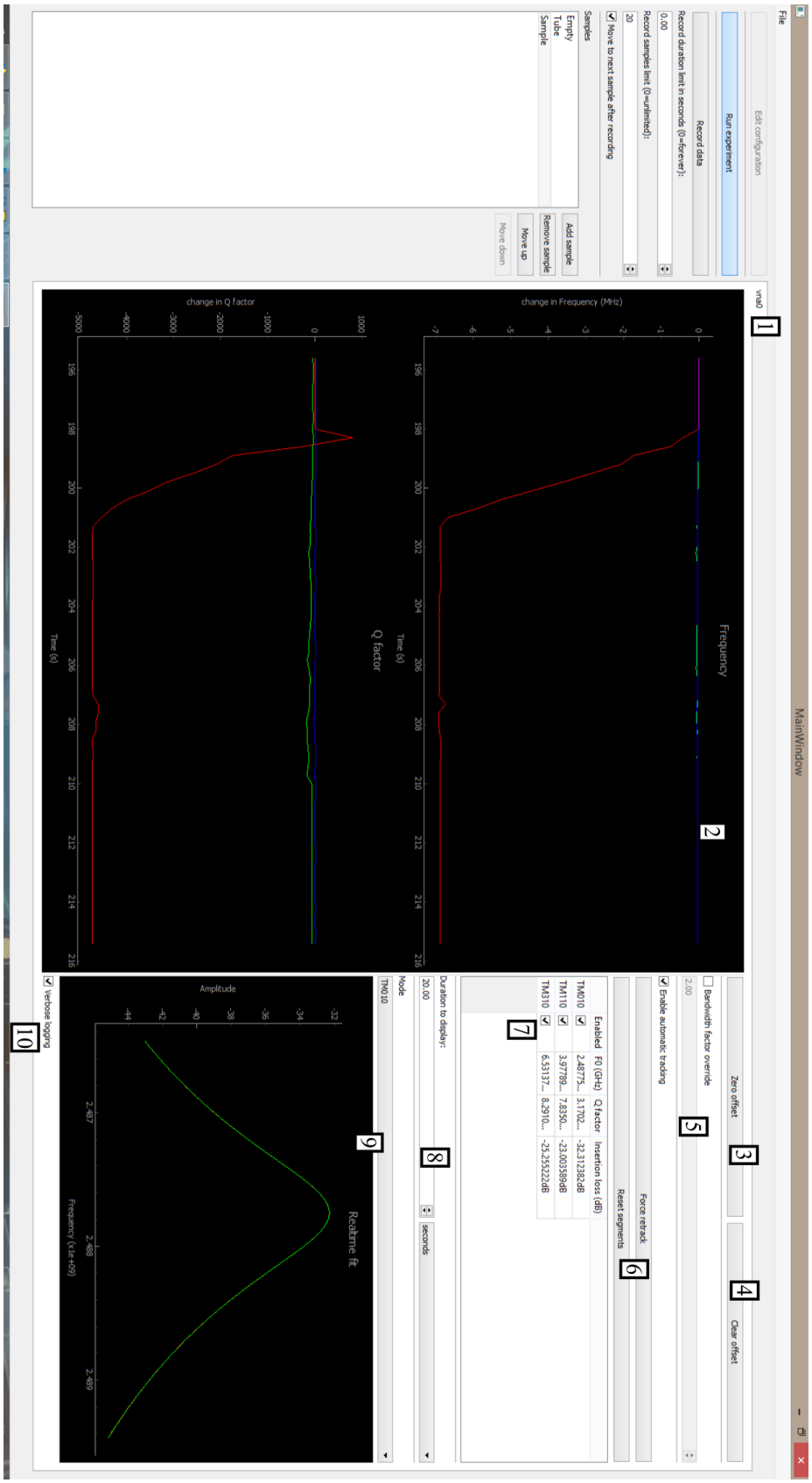


Fig. 4.4 Screenshot of the VNA control and data logging interface

The left third of the window contains generic controls for starting/stopping the experiment and choosing names for the samples when data logging. The remaining two-thirds contain the interfaces to control the instruments being used. The list below describes this inteface:

1. Each instrument's interface is displayed in it's own tab. In this case only a VNA is shown, but other instruments such as DC power supplies will appear in their own tab.
2. This is the main data view of the frequency and Q factor of the resonant modes being measured. This is updated once a second.
3. This sets the zero point on the graph as the current frequency and bandwidth for each mode. The values displayed are a delta from this point. This allows modes of vastly different frequencies to be seen on the same graph
4. This resets the graph to displaying absolute frequencies and Q factors
5. This allows the bandwidth factor to be overriden in realtime. The bandwidth factor is how many times larger the span should be compared to the bandwidth of the resonance curve being measured. This is useful if the curve develops significant skew during an experiment and needs to be fit more closely to the centre. Alternatively if the sample's properties are changing faster than expected then the span can be increased to reduce the risk of loosing track.
6. The force retrack button allow you to manually retrack the sweep segments to re-align with the center frequency and bandwidth of the lorentzian curve. The reset segments button resets the sweep segments back to the configuration state. This is useful if a segment has accidentally locked onto a different mode.
7. This allows you to modify the duration displayed on the main data window. This can range from a few seconds to several days.
8. This allows you to see how well the curve fitting is working for a particular mode in realtime. The red curve is the raw data, and the green is the fitted curve. If the curve fitting is not ideal then this will show it.
9. Verbose logging enables the logging of raw trace data. This is useful when debugging unusual results related to curve fitting, or just to record real world trace data to be inserted into a thesis.

## 4.4 Generic instrument scripting

Some microwave measurements require external stimulation to be controlled while the experiment is working, for example an external ultraviolet light source. The generic instrument scripting driver allows code to be written to control any VISA compatible instrument. Listing 4.4 shows the control of a DC power supply that waits for data recording to start, turns on the output for 10 minutes, turns off the output for 10 minutes, then beeps to signal measurement completion. If the experiment is stopped prematurely then the exception handling will ensure that the output is automatically turned off. The log statements will write a timestamped message to a datafile prefixed with the current sample name. This is useful for data alignment when processing the data.

Listing 4.4 DC Power supply automation

```
res.write("SYST:REM")
res.write("INST:SEL␣P25V")
res.write("SOUR:VOLT␣16.0V")
res.write("SOUR:CURR␣0.6A")
try:
  while True:
    record_wait()
    log("starting")
    pause(5.0)
    res.write("OUTP␣ON")
    log("output␣on")
    pause(600.0)
    res.write("OUTP␣OFF")
    log("output␣off")
    pause(600.0)
    res.write("SYST:BEEP")
    record_wait(False)
    log("finished")
except HaltException:
  res.write("OUTP␣OFF")
  raise
```

## 4.5 Temperature measurement

During microwave measurement experiments it is useful to know the ambient temperature and the temperature of the cavity. This can be used as a less accurate form of temperature correction when a reference microwave resonant mode is unavailable.

Unlike all the other instruments the temperature dataloggers used a binary serial interface instead of SCPI commands. In particular two different models are supported: the RS-pro 1365 humidity and temperature datalogger, and the RS-pro 1316 dual datalogger thermometer. The binary data format for these dataloggers is shown in Tables 4.1 and 4.2:

| Byte | Description |
|---|---|
| 0 | Start byte. Always 0x02 |
| 1 | Channel 1 thermocouple type and units (C/F/K) |
| 2 | Channel 1 high byte |
| 3 | Channel 1 low byte |
| 4 | Channel 2 thermocouple type and units |
| 5 | Channel 2 high byte |
| 6 | Channel 2 low byte |
| 7 | End byte. Always 0x00 |
| 8 | End byte. Always 0x03 |

Table 4.1 RS-pro 1316 dual datalogger thermometer binary format

| Byte | Description |
|---|---|
| 0 | Start byte. Always 0x02 |
| 2 | Temperature high byte |
| 3 | Temperature low byte |
| 5 | Humidity high byte |
| 6 | Humidity low byte |
| 8 | End byte. Always 0x03 |

Table 4.2 RS-pro 1365 datalogging humidity-temperature meter binary format

For both types of datalogger the high and low bytes form a 16 bit integer which is then divided by 10, resulting in the final decimal value.

## 4.6 Conclusion

On its own a VNA is not sufficient for realtime microwave resonant cavity perturbation measurements, thus some external software is required to control the instrument. The experiments discussed later in this thesis also required automated control of external stimuli such as light, and simultaneous measurement of temperature. Various existing solutions available at Cardiff University were analysed but unfortunately each had various limitations, resulting in the decision to write a software package from scratch.

To allow for maximum flexibility and expansion, the software was designed from the ground up using Python as the programming language and Qt5 with QtDesigner for designing the user interfaces. The software was designed to run each instrument driver in it's own thread with message queues to pass data from the driver to the main user interface thread, and commands from the UI thread to the driver.

The VNA driver was designed to support multiple models, and allow more to be easily added in the future. Currently the software supports Keysight's ENA and PNA network analysers as well as a portable USB network analyser created by Copper Mountain. On top of the network analyser abstraction were the various algorithms to control the acquisition of data. Segmented frequency sweeps allow the measurement of multiple resonant modes. Lorentzian curve fitting with first order skew correction converts the raw trace data into fit parameters. Automated re-tracking updates the measurement window when the resonant frequency or bandwidth shift too far within the current measurement window. Finally a backup re-tracking algorithm shifts the measurement window when the Lorentzian curve cannot be found based on the average slope of the visible data.

A generic instrument scripting driver was also created which allowed automated commands to be sent to any VISA compatible instrument, for example turning on/off a DC power supply after specified time intervals.

Finally a Temperature logging driver was created to interface to the RS-pro data-loggers. These are different to the other instruments in that they used a custom binary protocol, and so a lower level serial API was used to interpret the bytes received.

# Chapter 5

# Design of a Resonant Cavity for Light Exposure of Sheet Materials

## 5.1 Introduction

In order to test their pigments, Merck prepare them in a variety of ways. One of these is to disperse the pigment in a binder such as UV curing laquer, then spread the dispersed pigment over an acetate foil. This results in a sample similar to that in figure 5.1.

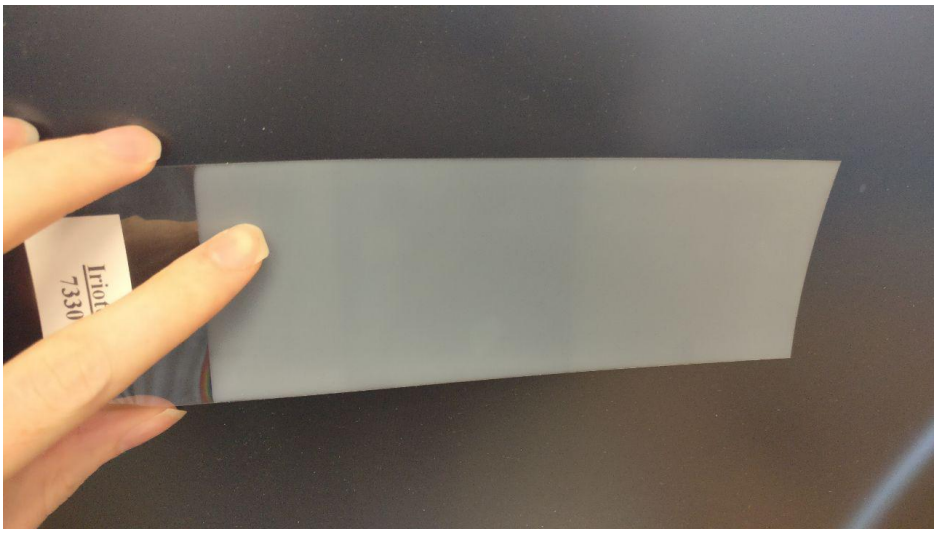


Fig. 5.1 A typical sample foil produced by Merck.

These samples are ideal for testing properties of the pigment in an environment very similar to their final application, for example antistatic flooring. Unfortunately these samples aren't

well suited to being measured in a cylindrical microwave resonant cavity due to their large aspect ratio, so a custom rectangular cavity is required instead. As these samples are reported by Merck to be light sensitive, the cavity also required a mechanism for illuminating them.

## 5.2 Resonant Cavity Design

To keep measurements simple, a primary measurement mode was chosen to be similar to the $TM_{010}$ mode used in a cylindrical cavity where the electric field is oscillating parallel to the sample. Similar to how the field patterns were derived for a cylindrical cavity, the electric and magnetic fields can be derived by applying boundary conditions to the helmholtz equations shown in equation 2.27. This results in the following equation for the electric field

$$E_y = E_0 \cos(\frac{mx\pi}{w}) \cos(\frac{ny\pi}{d}) \cos(\frac{pz\pi}{h}) \tag{5.1}$$

Where $m$, $n$ and $p$ are the mode numbers, $w$, $d$, and $h$ are the cavity dimensions and $x$, $y$, and $z$ are the coordinates along each axis respectively as shown in figure 5.2.

Due to the large aspect ratio of the sample, the electric field in the rectangular cavity needs to be stretched along the sample's width as illustrated in figure 5.2. This increases the uniformity of the electric field as well as reducing the overall magnetic field seen by the sample.

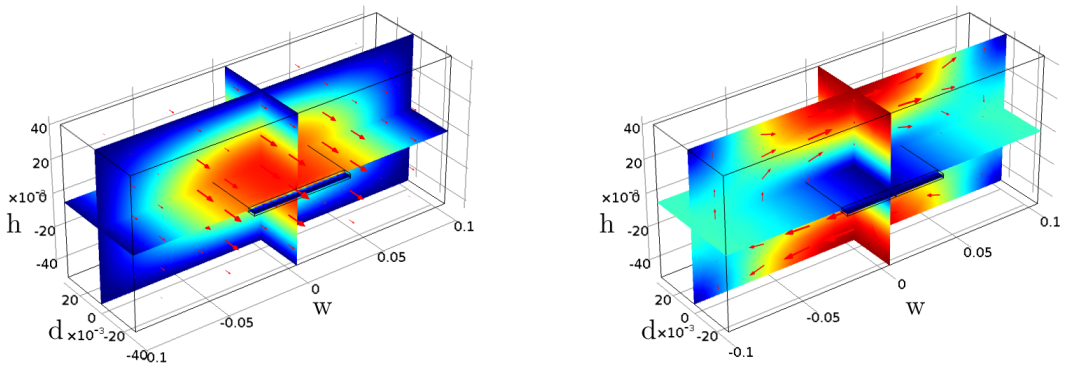


(a) Electric field (b) Magnetic field

Fig. 5.2 COMSOL simulation showing the desired electric and magnetic field of the primary measurement mode.

This stretching causes a drop in the resonant frequency of the mode to approximately 1.8GHz. A narrower sample could have been used to keep the cavity width smaller, however this

would reduce the surface area of material that can be exposed. The above geometry also potentially allows a temperature reference mode for non or weakly magnetic samples as shown in figure 5.3.

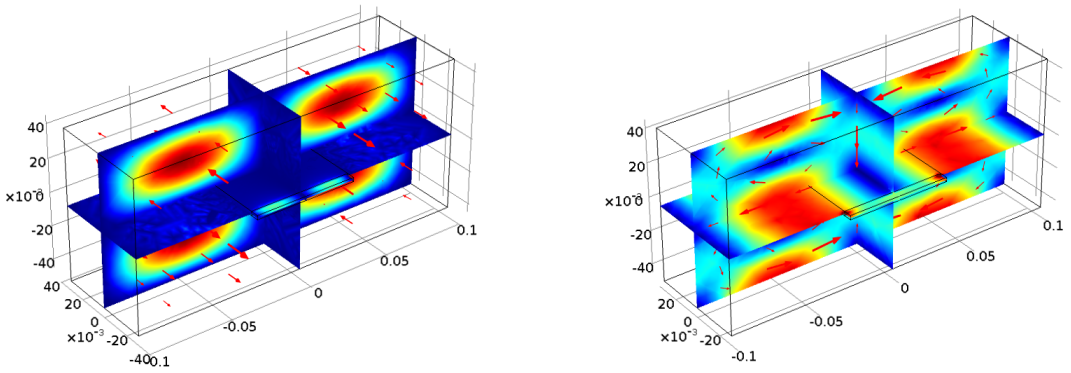


(a) Electric field

(b) Magnetic field

Fig. 5.3 COMSOL simulation showing the desired electric and magnetic field of the temperature reference mode.

The dimensions of the cavity also had to be chosen to allow uniform LED illumination of the sample. This will make analysing any colour shift easier later on. To ensure an even illumination of the sample the spacing and distance of the LEDs needed to be optimised. Using simple trigonometry and the inverse square law, the following equation can be derived for the relative illumination at a particular $x$, $y$ location on the sample:

$$I(x,y) = \sum_{n=1}^{N} \frac{L\left(\tan^{-1}\left(\frac{\sqrt{\Delta x_n^2+\Delta y_n^2}}{\Delta z_n}\right)\right)}{\Delta x_n^2+\Delta y_n^2+\Delta z_n^2} \tag{5.2}$$

Where $L(\theta)$ is the relative intensity of the LED at the angle $\theta$ from the centre and $\Delta x_n$, $\Delta y_n$, and $\Delta z_n$ are the relative distances from the point on the sample to the $n^{\text{th}}$ LED. This is illustrated in the schematic in figure 5.4.

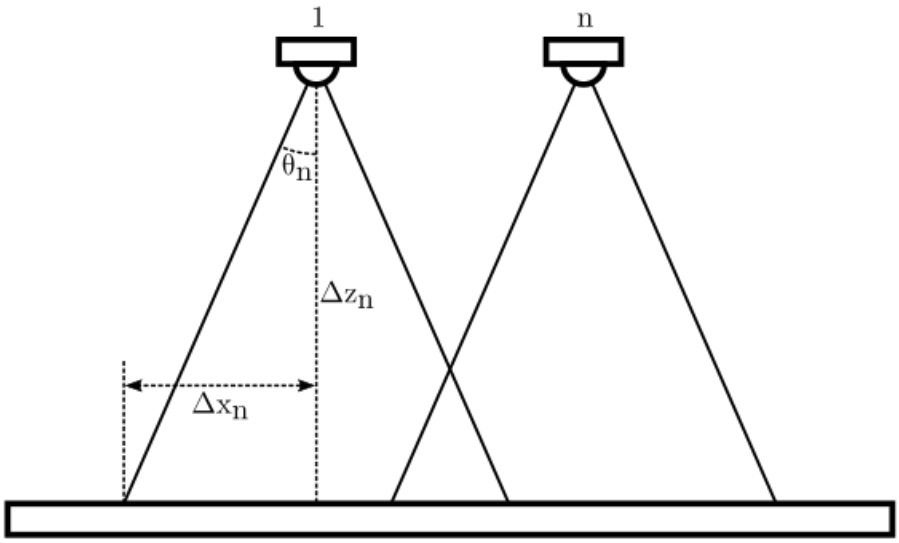


Fig. 5.4 2D schematic showing the LED positions relative to the sample and the values of $\Delta x_n$, $\Delta z_n$ and $\theta$.

The function $L(\theta)$ is shown in figure 5.5.

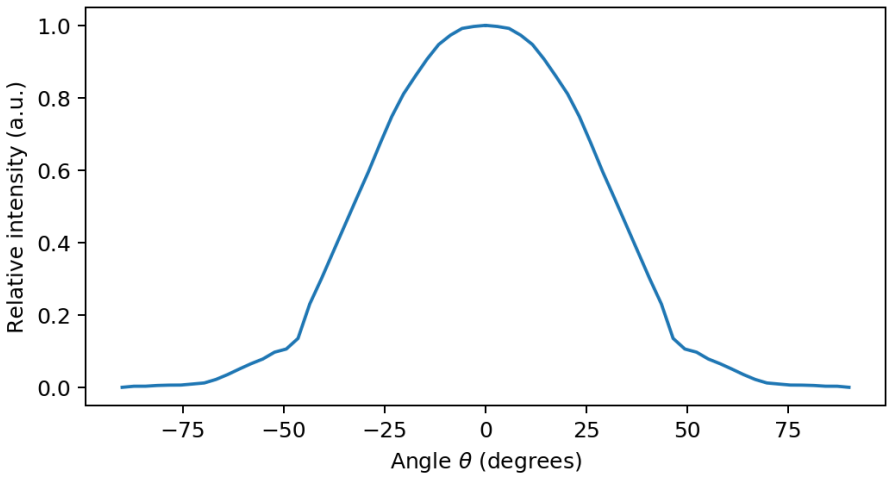


Fig. 5.5 Graph showing the relative intensity of the ultraviolet LED as a function of viewing angle $\theta$.

After tweaking the parameters, a spacing of 42mm was decided. The relative illumination pattern at this spacing is shown in figure 5.6.

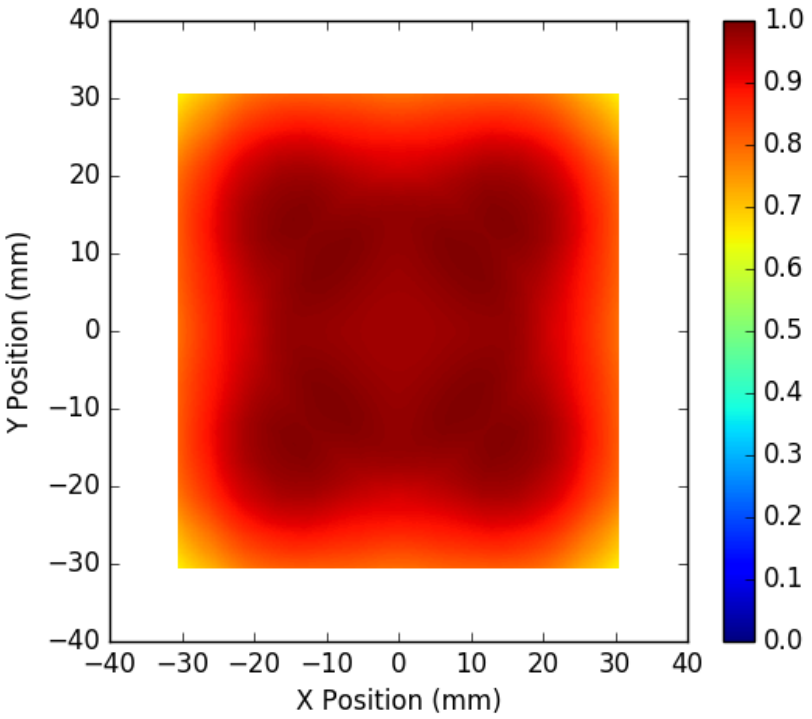


Fig. 5.6 Calculation of the relative illumination pattern 40mm from the LEDs with a spacing of 42mm between the LEDs.

Once the dimensions had been finalised, a 3D model could then be created for manufacturing. Figure 5.7 shows a render of the model.

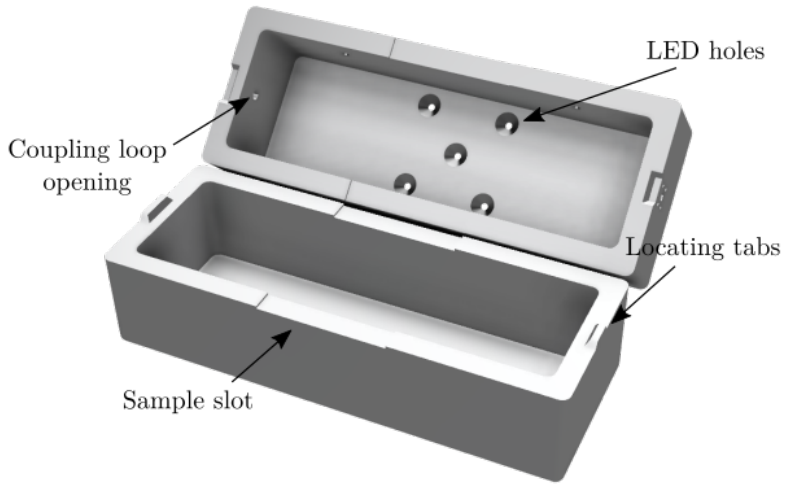


Fig. 5.7 3D render of the final microwave cavity design designed in Solidworks.

The 5 holes in the top of the cavity are for the 5 surface mount LEDs. The inside of the holes have been tapered to avoid obstructing the light whilst maintaining the overall cavity wall thickness. A simple PCB was designed in KiCad to mount the LEDs and to provide power. This is shown in figure 5.8.

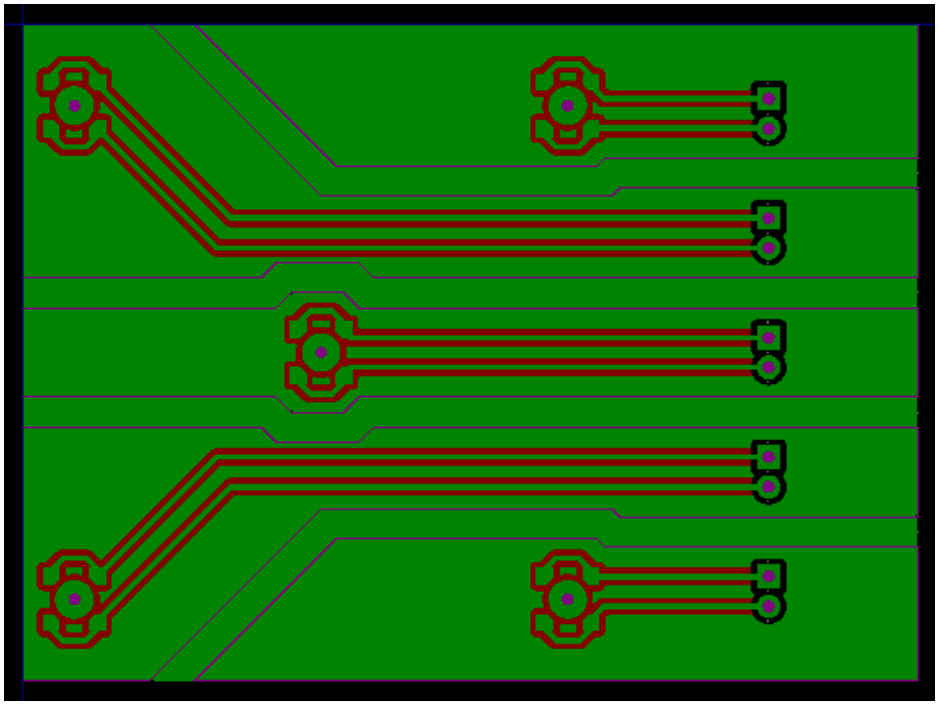

Fig. 5.8 PCB design for 5 LEDs created in KiCad. Each LED is on a separate board to allow for alignment variations.

The front green layer includes the traces and pads for the LEDs. The pad at the centre of each LED is a plated through hole which is connected to a large copper plane on the backside of the PCB, shown in red. This large copper plane is designed to dissipate the heat produced by the LEDs. The PCB is also split into 5 separate parts. This is to allow some slight misalignment when soldering the LEDs since the fit very precisely into cutouts in the microwave cavity itself.

## 5.3 Cavity Performance Testing

The final manufactured cavity is shown in figure 5.9. Four clasps have been added to the original design to ensure consistent pressure between the two halves.

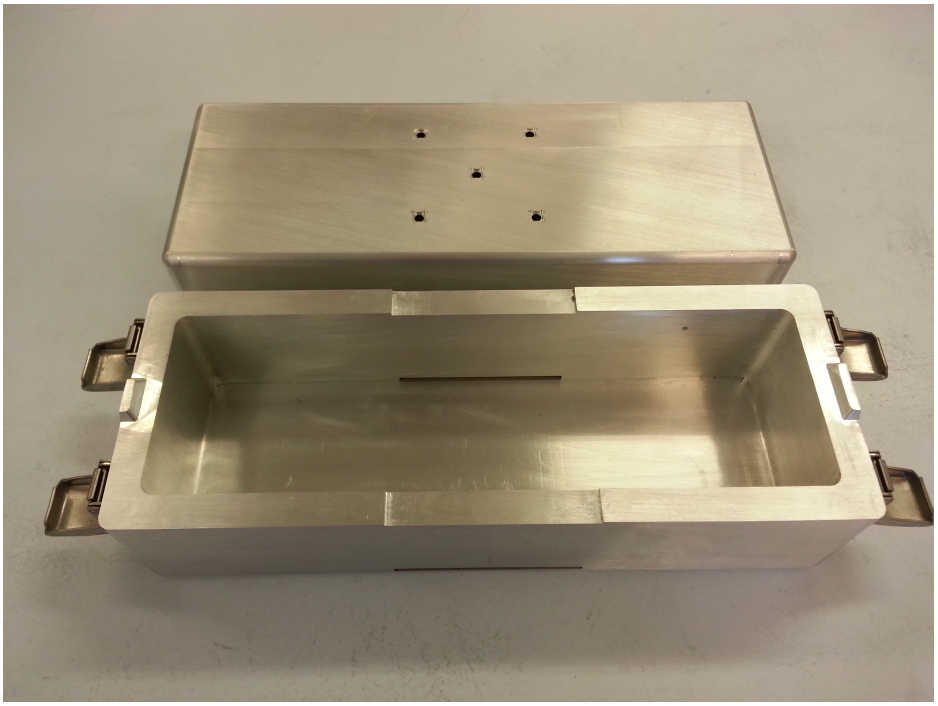

Fig. 5.9 The manufactured resonant cavity.

Aluminium was chosen over some other more conductive materials such as copper due to it being lightweight, cheaper, and easier to machine. The conductivity of Aluminium is still more than enough for this application as will be seen in the $S_{21}$ measurements in figure 5.11 later.

In order to use the cavity, some microwave coupling probes are required. These can be either a probe or a loop coupling which couple into the electric and magnetic fields respectively.

Since this cavity has the magnetic field concentrated at the edges, a loop coupling was used as shown in figure 5.10:

Fig. 5.10 Coupling loop created using an SMA connector and silver wire.

The loop sizes were adjusted until a coupling strength of roughly -20dB was achieved as shown in figure 5.11. This coupling strength is a tradeoff between sensitivity and signal to noise ratio.

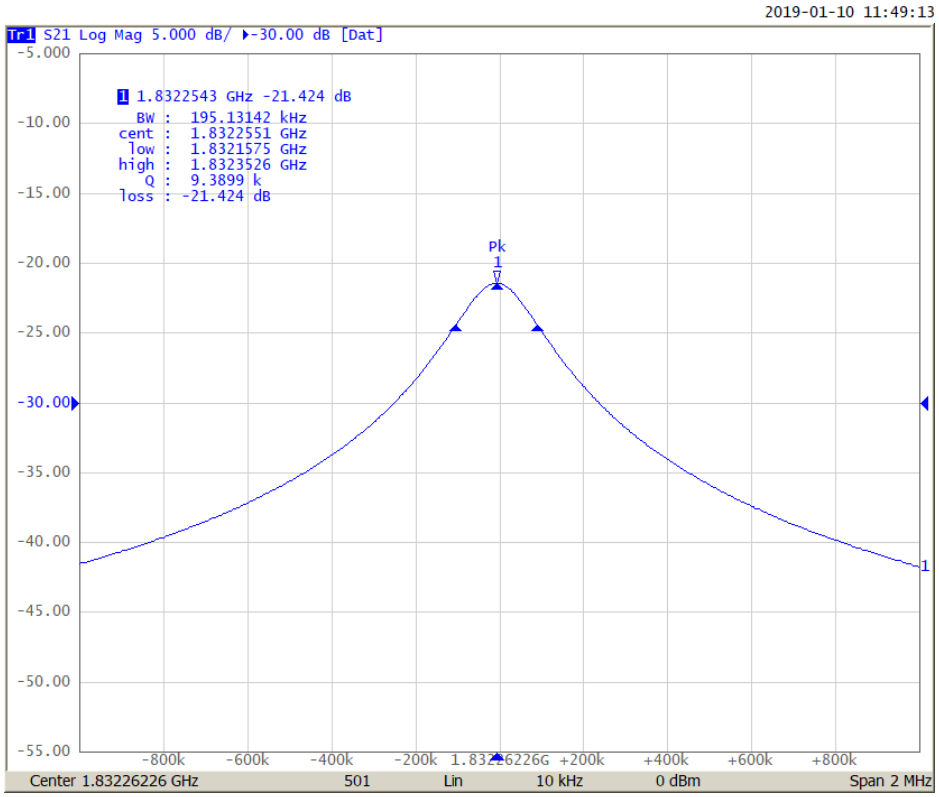


Fig. 5.11 $S_{21}$ measurement of the $TE_{110}$ mode of an empty cavity.

The Q factor is approximately 9000 which is more than adequate for low to moderate loss samples. As expected from the simulations, the frequency is around 1.8GHz. It is also important to check that the coupling strength is similar between the two probes. This is due to the approximations made when deriving equation 2.15 back in chapter 2. This can be checked by measuring the $S_{11}$ and $S_{22}$ responsed as shown in figure 5.12.

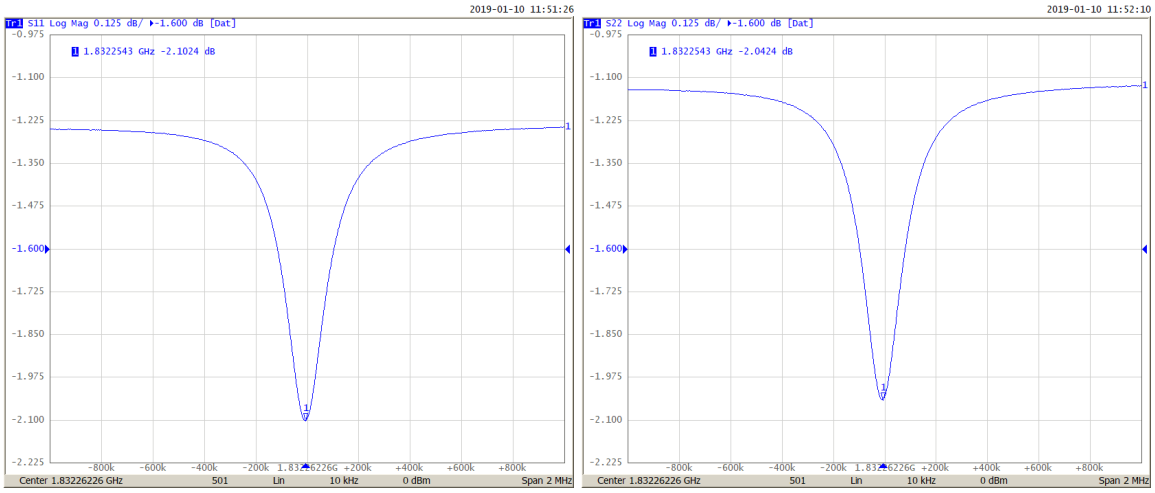


Fig. 5.12 $S_{11}$ and $S_{22}$ measurements of the empty cavity.

The rectangular cavity was also designed to potentially have some reference modes which were unaffected by the sample. Unfortunately, as shown in figure 5.13, the $TE_{120}$ mode was affected by the sample and thus can't be used. A similar result was also seen with the $TE_{220}$ mode too.

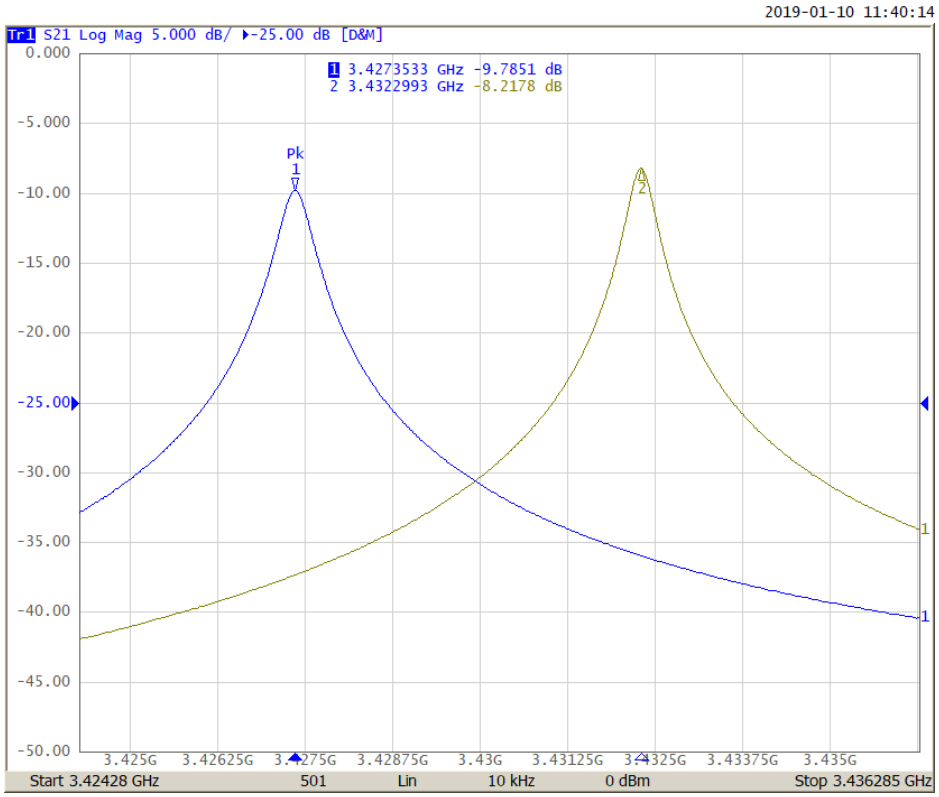


Fig. 5.13 $S_{21}$ measurement of the $TE_{120}$ mode of an empty cavity (yellow), and with a blank acetate sample (blue).

## 5.4 Conclusion

Acetate foil samples are a common geometry provided by Merck for testing their pigments dispersed in lacqueur as they are representitive of typical usage conditions. A rectangular microwave resonant cavity was designed to allow simultaneous light exposure and microwave cavity perturbation measurements to understand the properties of these pigments in realtime. The design involved microwave simulations using COMSOL multiphysics, and simulation of the LED illumination intensity across the surface of the sample to ensure even exposure. The cavity was then designed in Solidworks, and the PCB for the LEDs designed in KiCad. Finally the microwave resonant cavity was manufactured, assembled, and then tested for it's microwave performance. The primary $TE_{110}$ mode had a Q factor of approximately 9000 which is adequate for the samples that will be tested. The coupling strength was also measured to ensure that both input and output ports are symmetrically coupled as this is important for the assumptions made in the perturbation theory.

# Chapter 6

# Properties of Iriotec® 7000 Pigment Powders When Exposed to Light

Addition of conductive pigments is a useful means to provide conductive properties to otherwise non-conductive materials such as plastics. These properties are mainly required for static charge dissipation and electromagnetic/radio frequency interference shielding [70]. Graphite and metallic powders are such pigments and have been studied extensively [71–73]. More recently semiconductor based pigments such as Zinc Oxide and Tin Oxide have been studied as an alternative to pure metals and carbon [74–76]. One such pigment called Iriotec® 7000, produced by Merck KGAa, consists of antimony doped tin oxide coated onto mica sheets and quartz/talcum spheres.

Iriotec® 7000 series pigments are a range of electrically conductive pigments designed for use in applications that require electrostatically dissipative (ESD) properties. These pigments are made using a waterborne precipitation process of a conductive layer onto a dispersed substrate. Metal salts are added to the substrate dispersion, and the pH adjusted until the metal ions start precipitating in the form of hydroxides and oxides. These pigments are then filtered and washed to remove the salt solution before being dried at 110 °C and afterwards calcinated at 800 °C. Scanning electron microscopy images of the pigments can be seen in the figure 6.1:

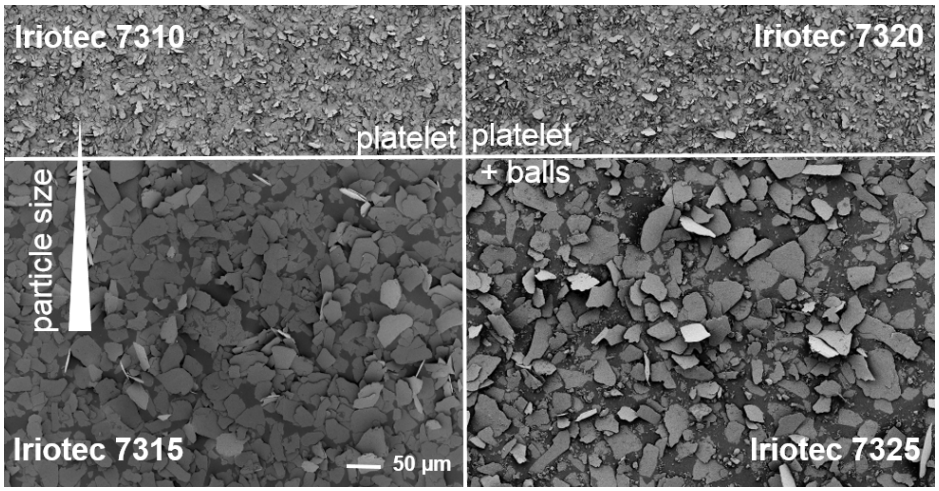


Fig. 6.1 Scanning electron microscopy images of various Iriotec® 7000 series pigments

Each batch of pigment is made with varying ratios of substrate to coating, and are also filtered to various sizes. A summary of these details is shown in table 6.1.

| Pigment | Substrate | | Coating | | | size |
|---|---|---|---|---|---|---|
| | type | % | type | % | doping % | µm |
| Iriotec 7310 | mica | 50 | ATO | 50 | 12 | 3-15 |
| Iriotec 7320 | mica/quartz 1:1 | 60 | ATO | 40 | 8 | 1-15 |
| Iriotec 7330 | mica/talcum 1:1 | 60 | ATO | 40 | 8 | 1-15 |
| Iriotec 7315 | mica | 70 | ATO | 30 | 12 | 5-60 |
| Iriotec 7325 | mica/quartz 1:1 | 70 | ATO | 30 | 8 | 5-60 |
| Iriotec 7510 | mica | 60 | ATO | 40 | 2 | 5-15 |

Table 6.1 Iriotec® sample composition

The combination of mica, quartz and talcum provide a conductive path throughout the bulk of the material which mica sheets would not provide as effectively on their own. This conduction mechanism is illustrated in figure 6.2:

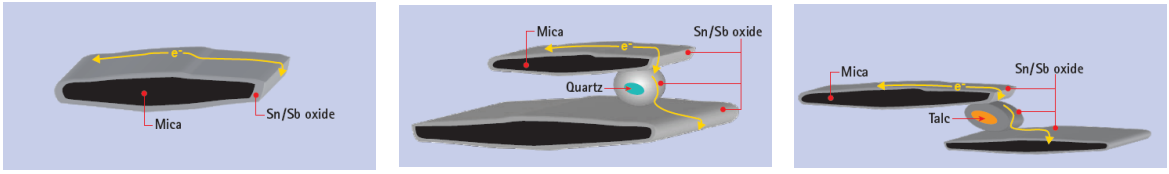


Fig. 6.2 Schematic illustration of Iriotec® 7000 pigments - mica flakes, quartz spheres and talcum flakes coated with conductive metal oxide layer.

Unfortunately it has been discovered that these pigments undergo a slight colour change when exposed to sunlight that reverts after some time. Clearly, this is undesirable in applications where they are used for aesthetic effect. Using microwave cavity perturbation measurements in combination with external light stimulation may help achieve a better understanding of these materials.

## 6.1 Method

All experiments were performed using the rectangular resonant cavity described in section 5 with 4 365nm UV LEDs. These were controlled from a serial enabled DC power supply. Due to the lack of a temperature correction mode, the temperature of the resonant cavity was measured at two locations using K type thermocouples. The samples being measured were acetate foils with the various Iriotec® 7000 pigments dispersed in a curing laqueur. A photo of this setup is shown in figure 6.3.

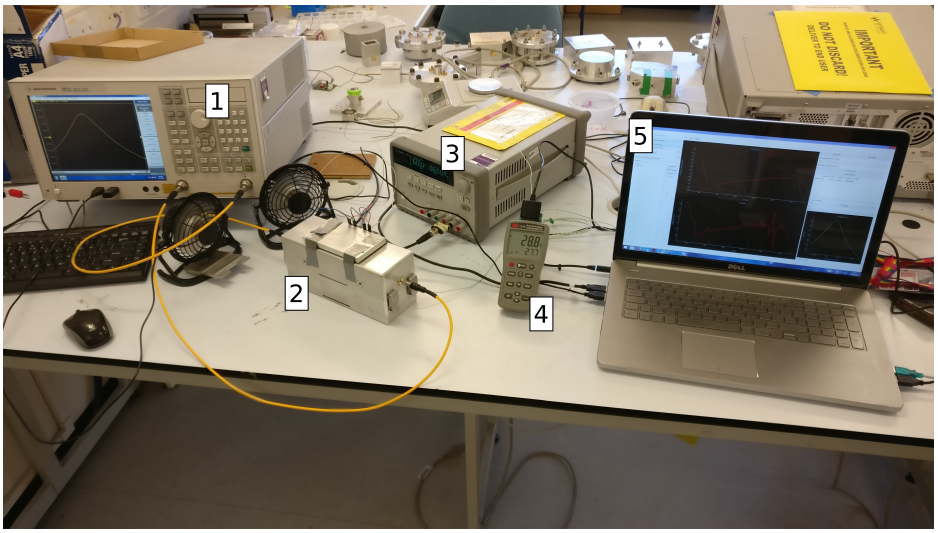


Fig. 6.3 Measurement setup showing the VNA (1), rectangular resonant cavity (2), DC power supply (3), temperature datalogger (4) and laptop controlling the whole system (5).

Each sample was exposed for 10 minutes, after which measurement continued for another 10 minutes. The samples were also photographed using a flatbed scanner to analyse any change in colour after the experiment. Throughout the sample measurements, reference measurements were also taken using blank foils with only lacqeur. These were used to construct a lookup graph for tempeature correction, similar to the technique explained in chapter 3. The difference between this experiment and the technique described in the

Temperature Correction chapter is that we do not have a reference measurement mode available. Instead we need to rely on temperature measurements from the thermocouples attached to the microwave cavity. As seen in figure 6.4, this does result in reduced precision and accuracy, however the measurements turn out to be adequate for the results shown later.

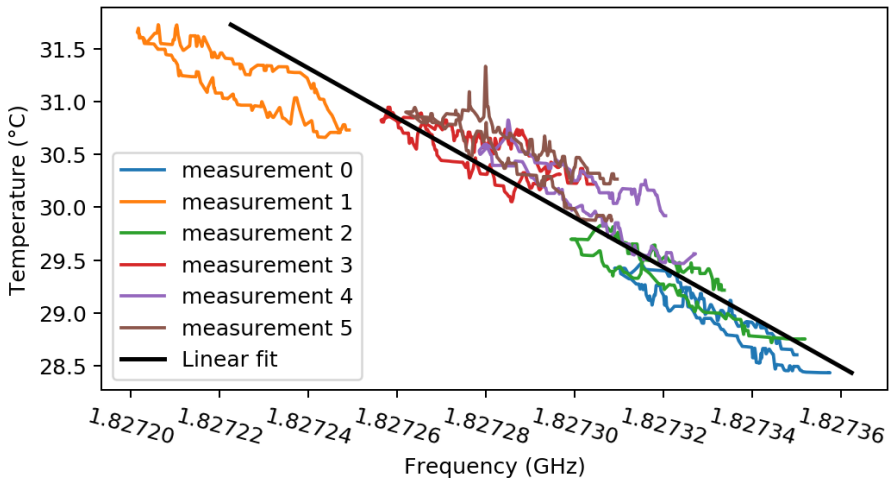


Fig. 6.4 Linear fitting to the 5 reference measurements taken at various times between the sample measurements.

Another experiment was performed to investigate the effects of temperature on the exposed samples. The coated foils were split into two halves A and B. Both halves were measured with microwaves and scanned before being exposed to UV light for 15 minutes. The samples were then left for approximately 5 hours before being measured again. This is to allow the microwave cavity temperature to stabilize. The B half of the samples were placed in an oven for 20 hours at 100°C. Both the A and B halves were then measured for a final time.

## 6.2 Results

The raw perturbation measurements result in a lorentzian response similar to that shown in figure 6.5.

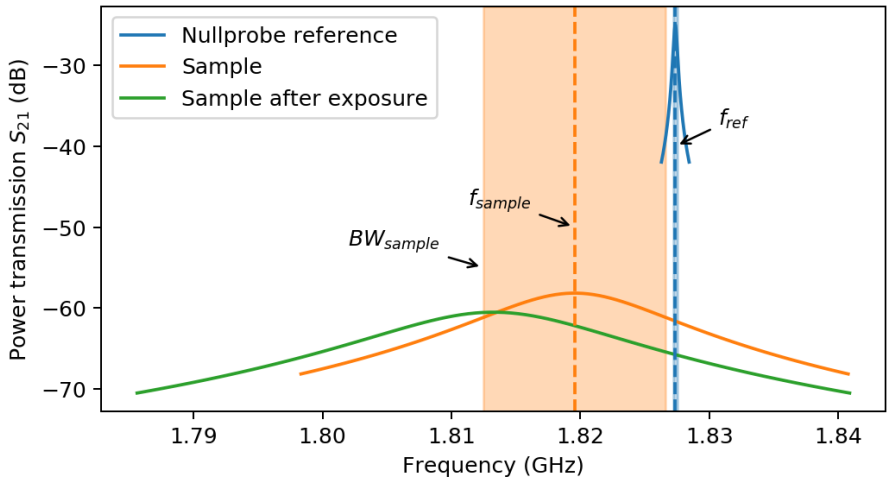


Fig. 6.5 Lorentzian response of a blank foil and of the Iriotec® 7315 foil before and after exposure. The extracted resonant frequency and bandwidth are illustrated.

Using the instrument control software discussed in chapter 4, the resonant frequency and bandwidth of the response are extracted. The relative shifts compared to an uncoated foil are then plotted over time as shown in figures 6.6 and 6.7.

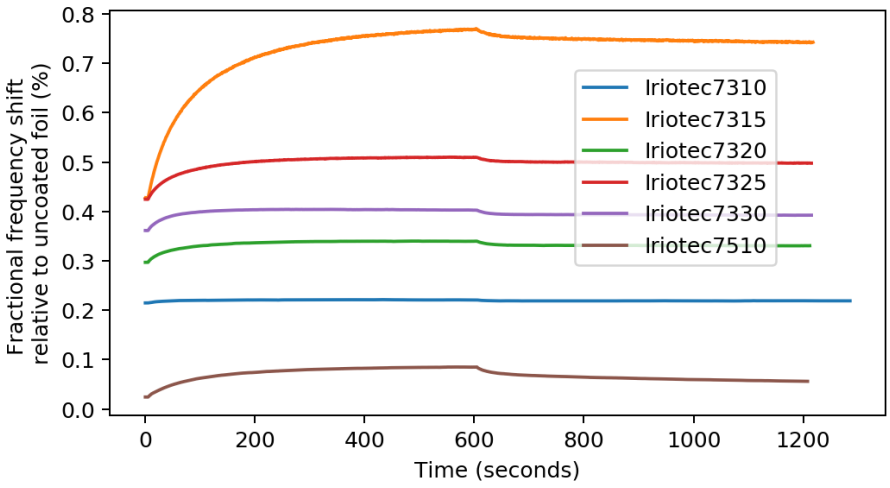


Fig. 6.6 Fractional frequency shift of all samples relative to an uncoated foil. The equation is $(f_{ref} - f_{sample})/f_{ref} \times 100\%$

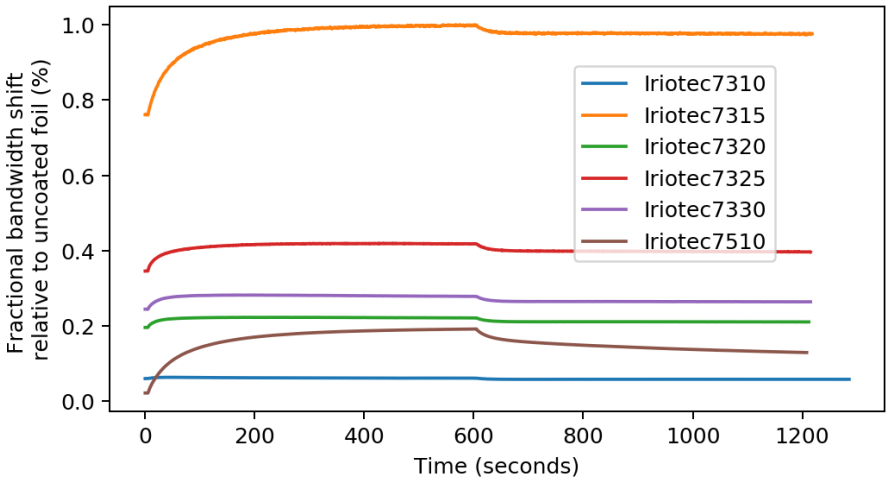


Fig. 6.7 Fractional bandwidth shift of all samples relative to an uncoated foil. The equation is $(BW_{sample} - BW_{ref})/BW_{ref} \times 100\%$

In order to analyse the samples further, a curve fit can be applied. This is shown for the Iriotec® 7330 foil in figure 6.8. The raw uncorrrected for temperature results are also shown.

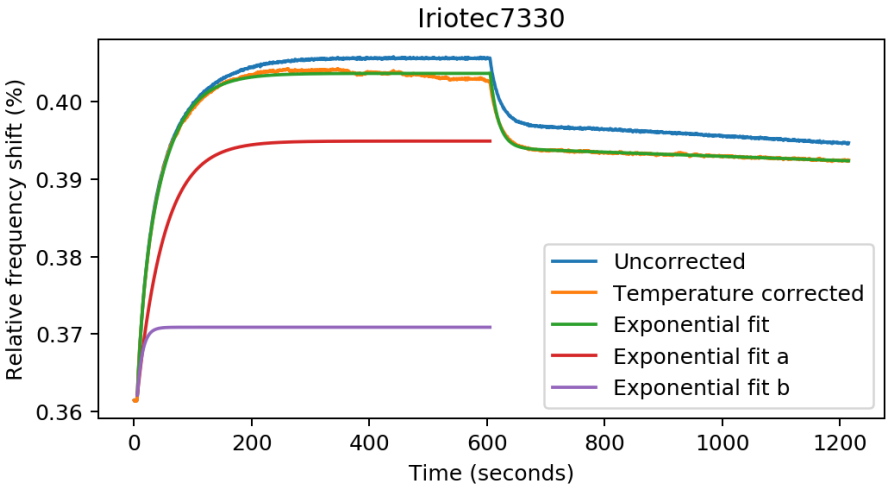


Fig. 6.8 Relative frequency shift of the Iriotec® 7320 foil sample with and without temperature correction, and with an exponential curve fit. The rise exponential is a double exponential which is split into a and b parts.

As can be seen, the temperature correction has a small, but noticeable effect. The curve uncorrected has an almost linear drift once the primary rise and fall exponentials have reached saturation. Once the correction is applied, the exponentials flatten out to a horizontal line.

For the rising curve a single exponential did not fit adequately. Through trial and error a double exponential described by the equation below appeared to fit well.

$$\begin{aligned} y = &(y_{1a} - y_0)\left(1 - e^{-(t-t_0)/\tau_a}\right) + \\ &(y_{1b} - y_0)\left(1 - e^{-(t-t_0)/\tau_b}\right) + y_0 \end{aligned} \tag{6.1}$$

where $t_0$ and $y_0$ are an initial point on the curve, $y_{1a,1b}$ are the positions at $t = \infty$, and $\tau_{a,b}$ are the times to reach $1/e$ the initial value. The exponential fits a and b in 6.8 are this equation separated into two separate exponentials. An exaggerated example is shown in figure 6.9 to further illustrate how the two exponentials combine.

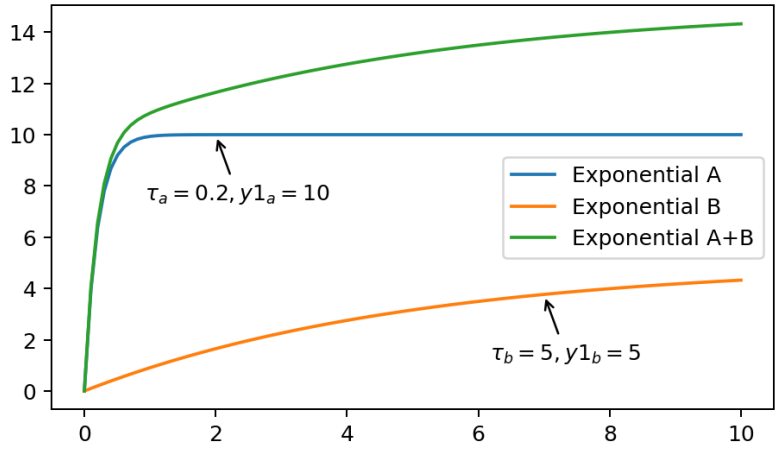


Fig. 6.9 Example of how two exponentials with different time constants and amplitudes combine.

Some of the falling exponentials also had a small slope after temperature correcting, so this was added as a term to the falling exponential equation:

$$y = (y_{1a} - y_0)\left(1 - e^{-(t-t_0)/\tau_a}\right) + y_0 + (t - t_0)k_{slope} \tag{6.2}$$

A summary of the rise and fall times are shown in figure 6.10.

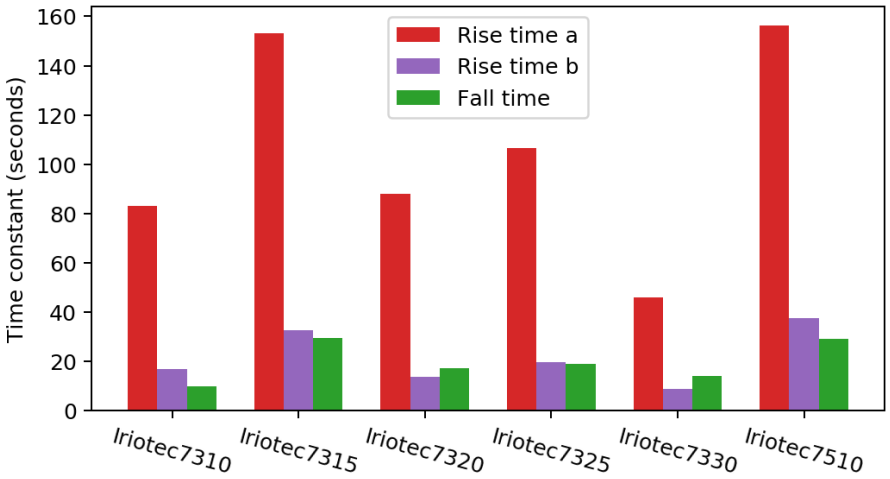


Fig. 6.10 Summary of the rise and fall times for all samples

This figure shows that all of the samples have a major rise exponential with a significantly longer rise time than the minor rise exponential. In all of the samples, the minor exponentials were not insignificant either, with the smallest being 0.25 times as large as the major exponential for Iriotec 7330. The largest minor exponential was for Iriotec 7310, however this also had the smallest response when compared to figure 6.6. Another observation from figure 6.10 is that the fall times are always closer to the minor exponential than the major.

A final comparison was to look at the ratio between the total rise exponential amplitude and the fall exponential. This gives a measure of how permanent the change from UV exposure is.

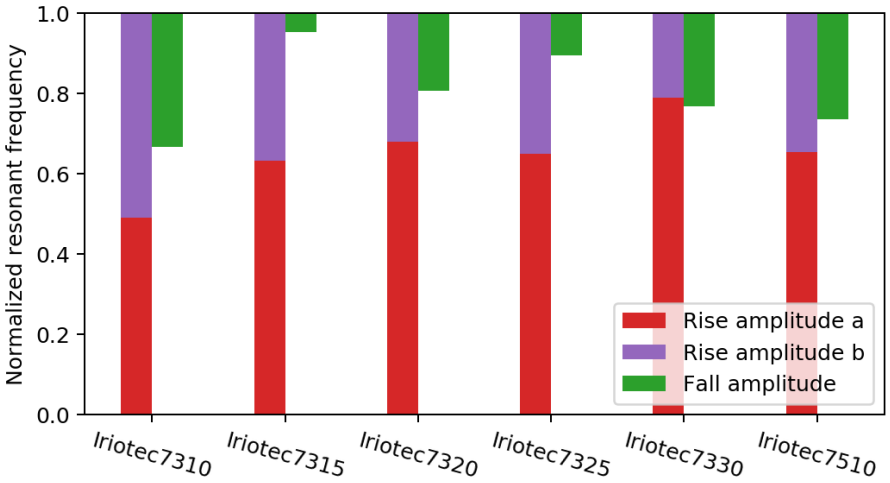


Fig. 6.11 Ratio of total rise exponential amplitude to fall exponential

This shows that there is not a consistent relationship between these two exponentials, however comparing to figure 6.6 it appears that both the major and minor exponentials become part of the semi-permanent change once the light is removed.

After performing the experiments it was observed that the samples had a subtle colour change as a result of the UV exposure. Scans of these samples are shown in figure 6.12. Due to how subtle the changes were, the contrast was enhanced by raising the normalised RGB values to the power of 5.

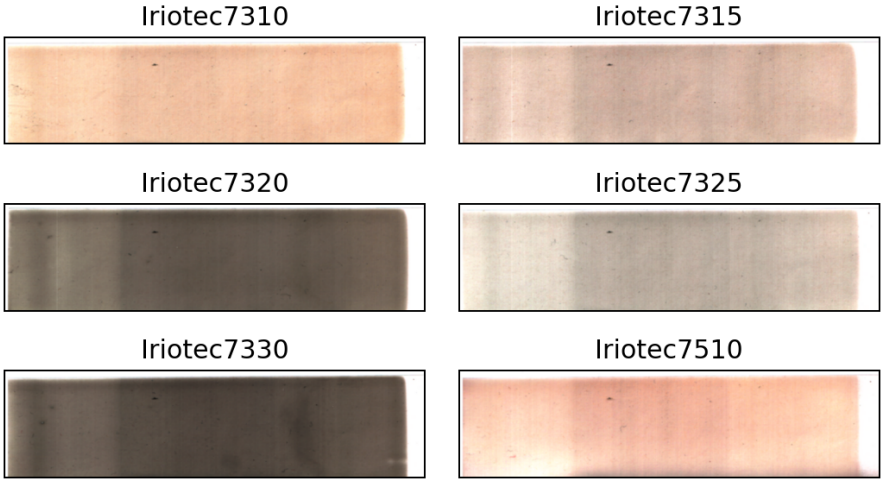


Fig. 6.12 Scanned images of the various Iriotec foils.

Because of the previous results another experiment was performed to investigate if heat could restore the samples back to their original state. To check that the changes aren't being caused by the lacqeur, a lacqeur only foil was also subjected to the same treatment. This reference is shown in figure 6.13.

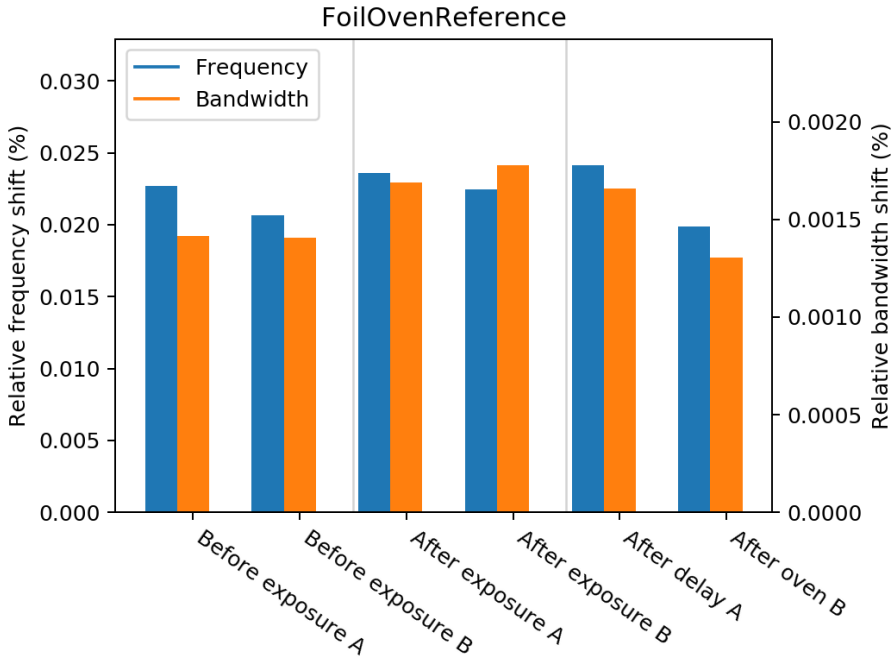


Fig. 6.13 Oven experiment results for the nullprobe reference foil. Shifts are relative to an uncoated foil

There is a small shift in relative frequency and bandwidth. To reduce any bias in the following results caused by this shift, all the sample frequency/bandwidth shifts will be relative to the associated lacqeur only foil. For example a sample exposed to heat will be relative to the half of lacqeur only foil also exposed to heat. The inverse luminance in figures 6.14 to 6.19 is calculated using the following equation:

$$L_{inv} = 100 - (R \times 21.26 + G \times 71.52 + B \times 7.22) \tag{6.3}$$

The full Red/Green/Blue data can be found in appendix B.

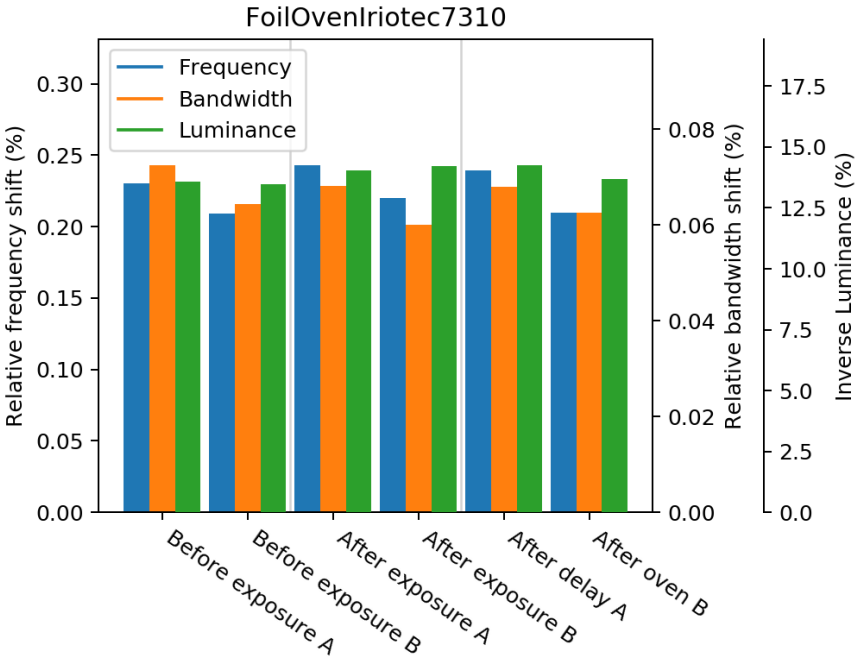


Fig. 6.14 Oven experiment results for Iriotec 7310.

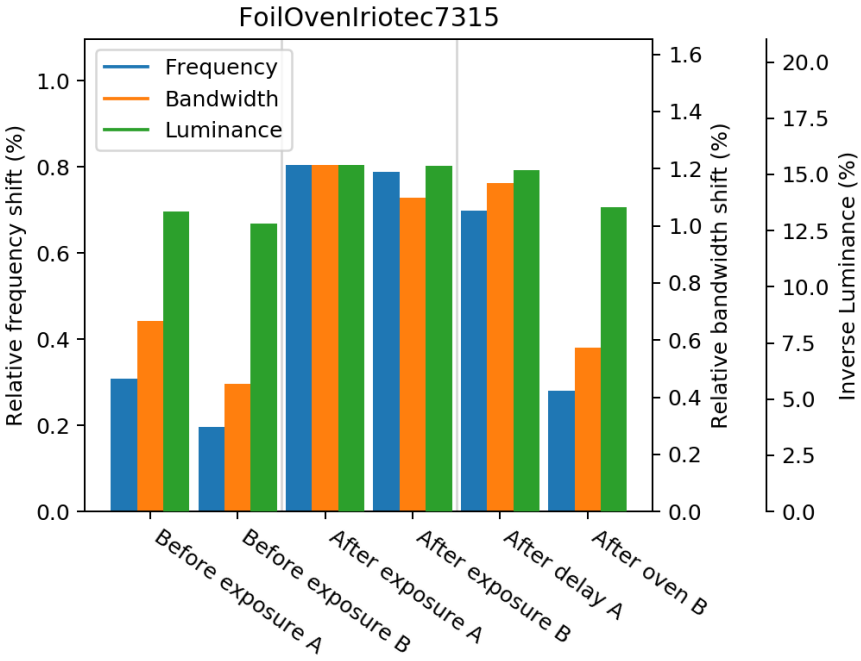


Fig. 6.15 Oven experiment results for Iriotec 7315.

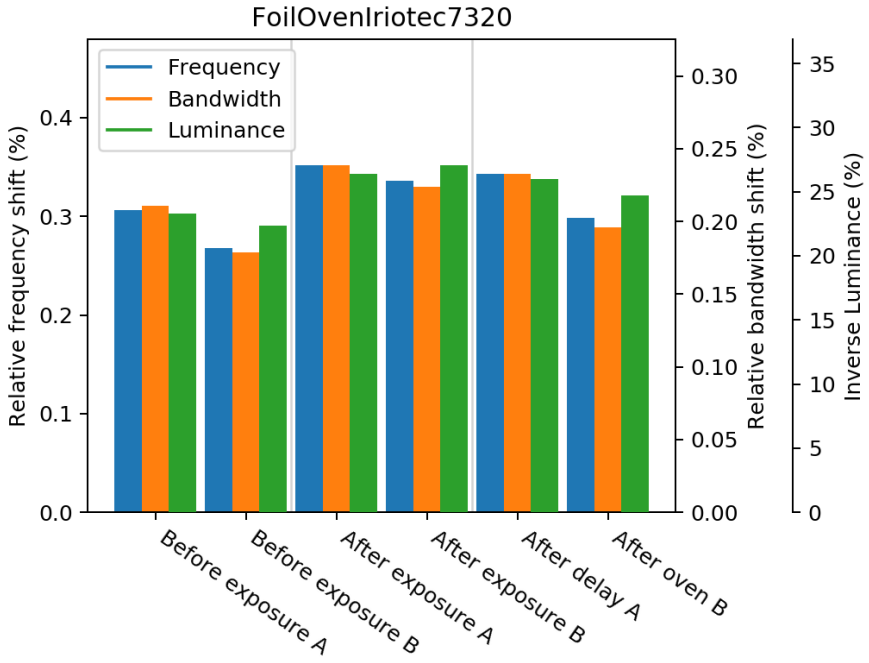


Fig. 6.16 Oven experiment results for Iriotec 7320.

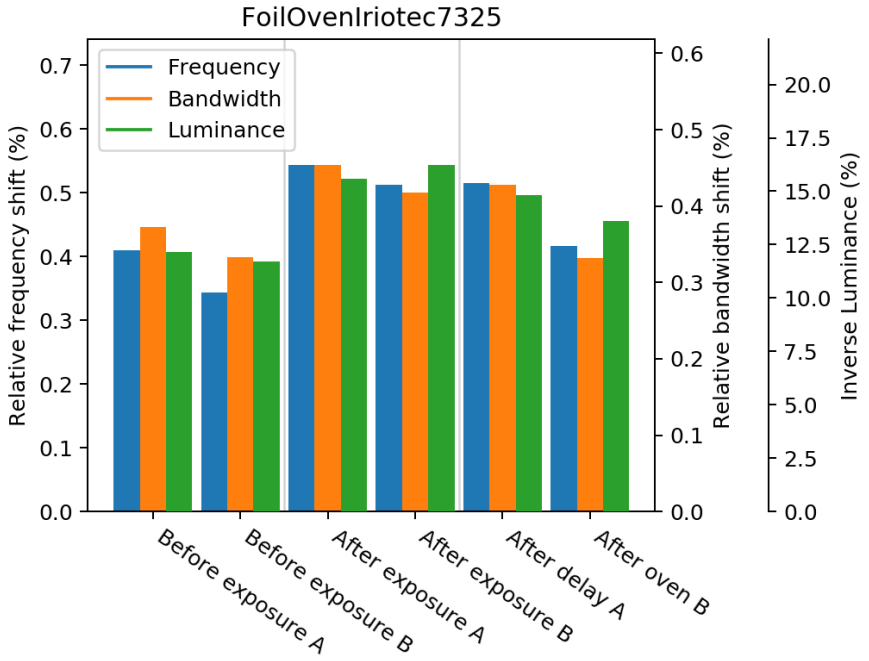


Fig. 6.17 Oven experiment results for Iriotec 7325.

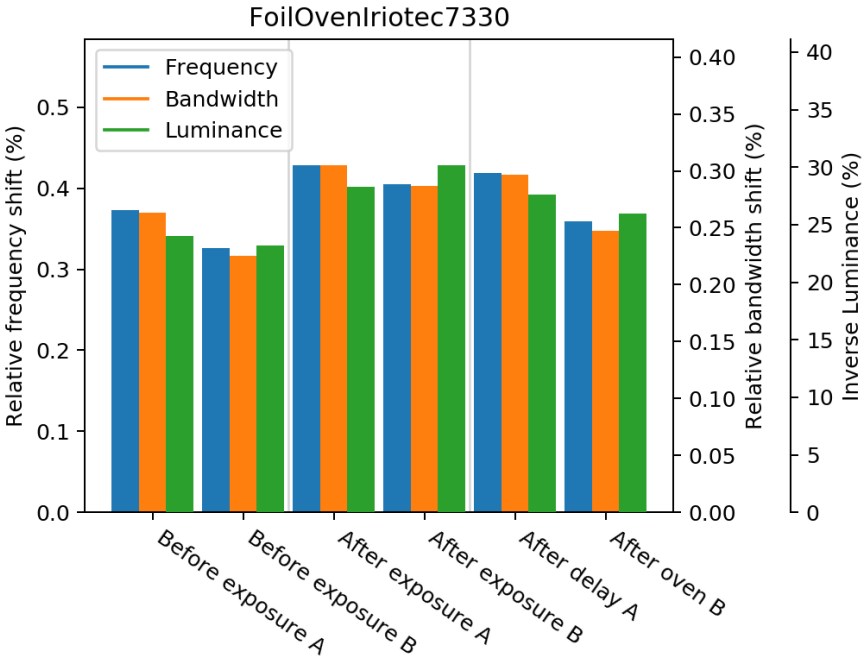


Fig. 6.18 Oven experiment results for Iriotec 7330.

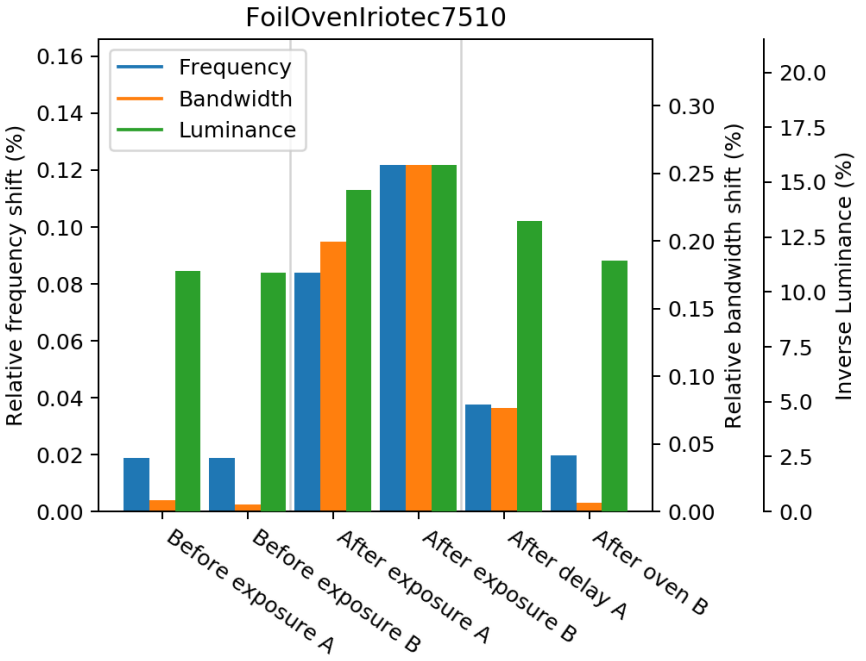


Fig. 6.19 Oven experiment results for Iriotec 7510.

## 6.3 Discussion

### 6.3.1 Effects of Sample Composition on Static Properties

The easiest observation to make is the effect of particle size on the loss of the samples. In general the larger particles show a larger absolute loss value. The larger particles also have a larger substrate to coating ratio. A possible explanation for this is a reduced depolarization effect of the larger aspect ratio samples. Depolarization is caused by the electrons at the surface of the material resulting in a reduced electric field within the sample, and thus a lower measured loss. For a larger aspect ratio sample this depolarization has less of an effect as illustrated in figure 6.20.

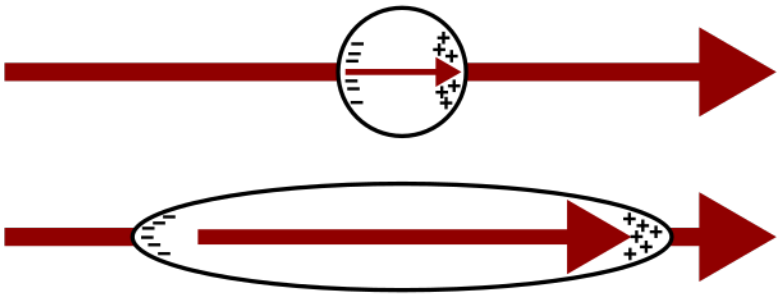

Fig. 6.20 Depolarization caused by low and high aspect ratio particles. The lower aspect ratio particle is more effective at shielding the electric field from within the sample than the high aspect ratio one.

Unfortunately it's not possible to draw any conclusions regarding the effect of doping on the conductivity of the samples under static conditions, however as explained in the next section it is possible to explain the effects of doping on the dynamic properties.

### 6.3.2 Change in Properties Over Time

From figures 6.6 and 6.7 it can be seen that all of the samples exhibit some changes when exposed to ultraviolet light. In a typical semiconductor, light exposure of a wavelength below the material's bandgap will cause the generation of electron-hole pairs, however this generation, and subsequent recombination, are usually on the order of nano or picoseconds. The effects seen here occur over several minutes. This is a known issue in oxide based

semiconductors where the photoconductivity can occur for several hours which can be problematic when used as a photosensor [77], and some experiments have been done to show this as seen in figure 6.21.

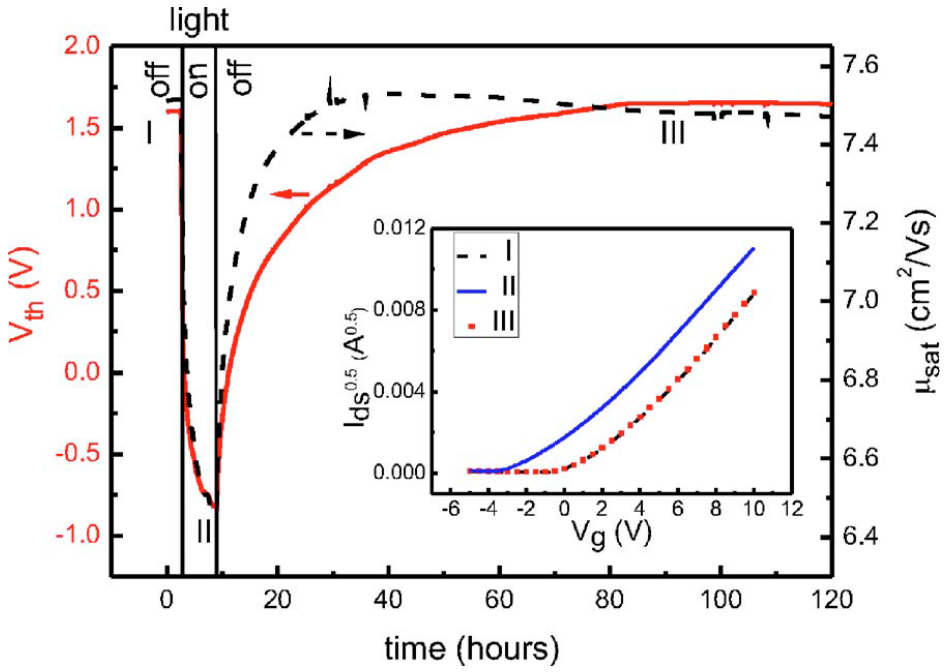


Fig. 6.21 Effects of violet irradiation $\lambda = 425nm$ and $I = 250\mu W/cm^2$ on $V_{th}$ and $\mu_{sat}$ of ZTO TFTs. Inset: transfer characteristics before (black), during (blue), and several hours after (red) irradiation [78].

As an aside the article for figure 6.21 above notes that the measurements are only taken every 500 seconds to keep the bias stress of the measurement itself as small as possible. The non-contact microwave measurements do not suffer from this issue, and measurements can be taken as fast as the hardware and software will allow.

It can be clearly seen that this issue is not unique to these ATO based Iriotec® 7000 pigments. Some parallels have been made to the study of bias stress in thin film transistors which attribute these mechanisms to charge trapping in the dielectric and defect creation in the channel material [79–82]. In the case of the Iriotec® pigments, it is possible that charge is being trapped in the non-conductive laqueur and mica/quartz/talcum substrates at the interface to the ATO semiconductor. When looking at the effects from the semiconductor itself, many reports have found the surface properties to be particularly important [83–85]. For example in ZnO it is found that the conductivity changes as oxygen is absorbed and desorbed from the surface during UV illumination.

The above mechanisms explain the increased conductivity of the samples, however they don't yet explain the darkening of the samples. This darkening effect when exposed to EM radiation is known as photochromism, and is usually seen in applications such as transition lenses. These however are usually manufactured using organic compounds [86]. The change in colour of a material is often associated with a change in the bandgap of a material, and this can occur for multiple reasons. One possible cause is a change from one oxidation state to another. Some research has been performed on Tungsten Oxide films which show an increase in absorbtion in the visible region when exposed to ultraviolet light, and has attributed the changes to this [87–89]. Another possible cause is something known as the Moss–Burstein effect [90–93]. This is a phenomenon where the apparent band gap of a semiconductor is increased as states close to the conduction band are populated, pushing the absorbtion edge to higher energy levels. This is illustrated in figure 6.22.

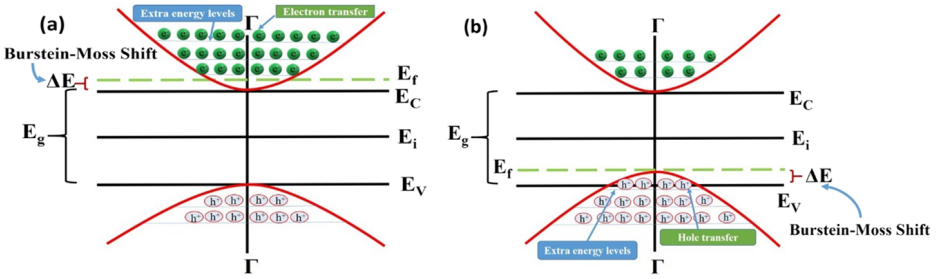


Fig. 6.22 Band diagram for positive (a) and negative (b) Burstein-Moss shift for extrinsic semiconductors [94].

The other interesting results were the high temperature annealing of the samples. The results showed that the relaxation of the samples back to their initial state was far quicker at 100°C than at room temperature. Again, research has been performed on other metal oxides such as ZnO and $TiO_2$ which show changes over the course of hours/days [95, 96]. Both of these papers attribute the slow changes of these samples to the thermally driven relaxation of the trapped holes that are preventing the recombination with electrons and thus resulting in increased conductivity. It would make sense then that at a higher temperatures this thermal relaxation is going to happen faster.

What hasn't been discussed yet is the effect of doping on the response of the samples. From the selection of Iriotec® samples available it can be seen that the very low doping of 2% of the Iriotec® 7310 has a large relative change compared to those with higher doping levels. Antimony doping introduces additional free electrons into the material making it n-type where there are more free electrons than holes. Since the mechanisms described in the temperature annealing theory are thought to be caused by trapped holes, it makes sense

that the lower doping levels should show the largest changes. What complicates this is that Iriotec® 7315 also shows a large response despite having the highest doping of 12%. It does however have the largest particle sizes and initial conductivity, so the percentage change is still smaller than that of Iriotec® 7310. While this is a possible explanation, unfortunately there are a lot of variables at play and the full explanation is likely more complicated than this.

## 6.4 Conclusion

This chapter has shown that the new rectangular microwave resonant cavity is an effective device for measuring the change in electromagnetic properties of foil samples under exposure to ultraviolet light. Six Iriotec® foils were measured. These contain ATO coated onto various substrates such as mica sheets and quartz/talcum spheres, all dispersed in a lacqeur. It was observed that the larger particle sizes were the most dominant contribution towards increased conductivity, however the platelet/sphere interaction did provide a small increase too.

The realtime response of the samples was also analysed and a combined exponential response was observed during the exposure of the samples indicating two different mechanisms. It is suspected that this is a combination of charge being trapped in the substrate/lacqeur and surface defects in the ATO coating causing oxygen vacancies which will also act as traps. It was also observed that the lowest doped sample showed a far greater proportional change compared to the higher doping levels. This is likely due to fewer free electrons that will want to recombine with the generated holes before they are scavenged.

A semi-permanent change was also observed in the samples, both in the microwave measurements and a colour change in the samples. Another experiment was performed where the samples were exposed for 15 minutes before placing one half in the oven at 100°C overnight. It was found that the oven exposed samples relaxed to near their initial state whereas the unexposed samples remained mostly unchanged. It is suspected that this increase in conductivity and colour change are the result of a higher oxidation state, but could also be related to the Moss–Burstein effect. Since the relaxation is a thermally driven process, it is of no surprise that the thermal treated samples relaxed faster than the untreated ones.

# Chapter 7

# Light Exposure of Titanium Dioxide

Titanium Dioxide ($TiO_2$) is a white material which can be used as either a pigment, or a photocatalyst. Pigment grade $TiO_2$ is useful for its UV blocking properties, whereas photocatalytic grade $TiO_2$ is used for its ability to absorb light energy to catalyse chemical reactions.

Without additional dopands or impurities, titanuim dioxide can occur in 3 crystalline phases: rutile, anatase and brookite. Rutile and anatase phases are the most common due to brookite being difficult to produce. These crystal structures are shown in figure 7.1.

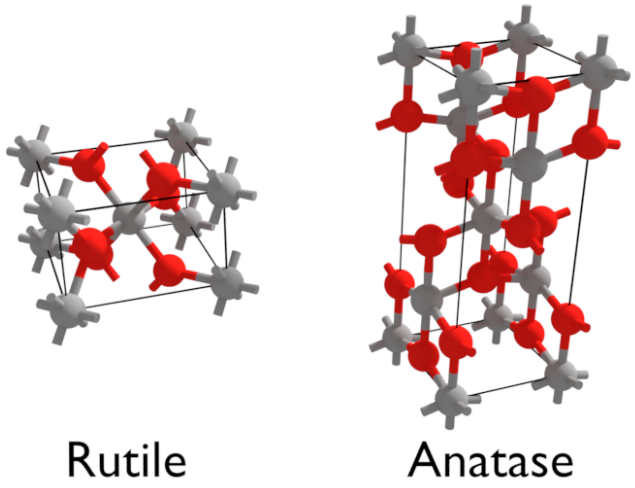


Fig. 7.1 Crystal structure of anatase and rutile phases of $TiO_2$.

The pure white optical properties of $TiO_2$ arise from its bandgaps of 3.05eV and 3.29eV for rutile and anatase, respectively. These bandgaps correspond to absorption bands at free

space wavelengths of <415 nm for rutile and <385 nm for anatase, which are in the violet and ultraviolet part of the visible light spectrum, respectively [1, 97].

As mentioned before, $TiO_2$ can be used as a photocatalyst. The mechanism for this is a result of charge carrier generation upon absorbtion of ultraviolet light. These charge carriers (electrons and holes) can then participate in other reactions. Typically the anatase polymorph of $TiO_2$ has greater photocatalytic activity than rutile [98]. A schematic of this mechanism is shown in figure 7.2.

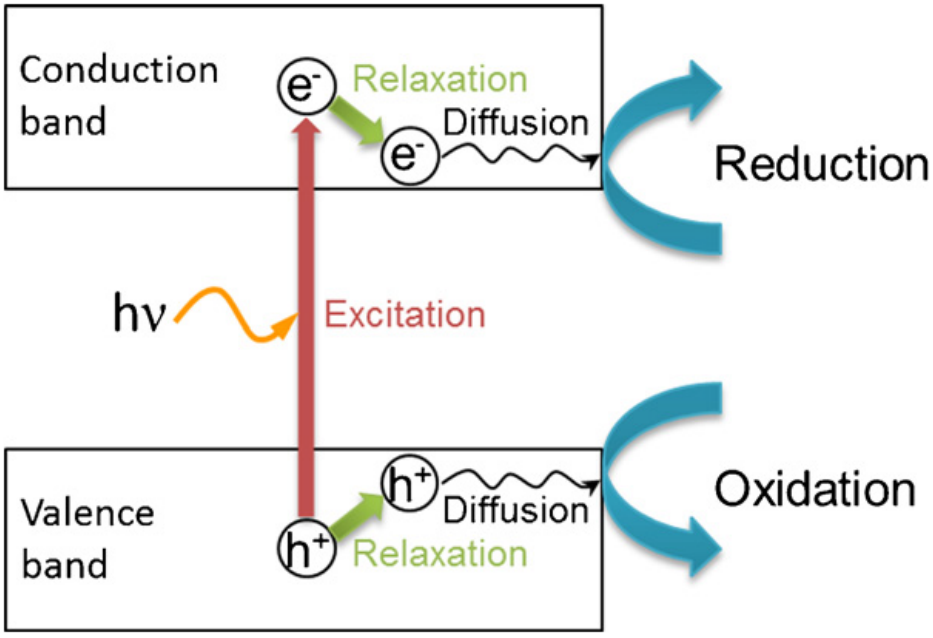


Fig. 7.2 Schematic illustration of the formation of photogenerated charge carriers (hole and electron) upon absorption of ultraviolet (UV) light [99].

The actual chemical reactions are slightly more complicated and usually involve intermediate trapped states. For example, in the degredation of methyl orange, a common method of measuring photocatalytic activity, the generated charge carriers first react with hydroxyl groups or water to produce $^{\bullet}OH$ radicals. These radicals have a high reactivity towards decomposing organic compounds like azo-dyes [100]. In addition, a minor amount of other oxidative species, such as $^{\bullet}O_2^-$ and $H_2O_2$ can be generated through the capture of electrons in the conduction band [101, 102]

## 7.1 Optimising $TiO_2$ for Photocatalysis

Numerous methods have been adopted to modify $TiO_2$ to improve its efficiency. These can be split into two categories: improving the UV efficiency, and sensitising to visible light wavelengths.

### 7.1.1 Increasing UV Efficiency

The main limiting factor when using $TiO_2$ as a photocatalyst is the rate at which electrons and/or holes are scavenged after being generated. If no suitable scavengers are available then the electrons and holes will recombine within nanoseconds and dissipate the energy as heat [103, 104]. One such scavenger is the $^{\bullet}OH$ radical who's yield depends on the substrate concentration, pH, oxygen concentration and more when preparing the $TiO_2$ [101]. To a lesser extent the total surface area of the $TiO_2$ can also affect the scavenging rate. The simplest parameter to control is the crystalline size. Smaller crystals have been shown to be better photocatalysts than larger ones [105]. This is expected since the smaller crystals will have a larger surface area to volume ratio. More complicated techniques can also be used to improve photocatalytic activity. For example Degussa P25 has an unusual microstructure with a coexistence of amorphous, anatase, and rutile phases of $TiO_2$ which has been found to have unusually high photocatalytic activity [106]. $TiO_2$ can also be engineered into more complicated shapes such as hollow spheres, nanotubes and sheets [99]. All these shapes aim to increase the surface area to volume ratio.

### 7.1.2 Visible Light Sensitisation

As well as increasing the sensitivity to UV light, $TiO_2$ can also be sensitised to other wavelengths. One common method is to dope or surface treat the $TiO_2$ with other elements such as N [107–112], C [113–116], or with metals [117]. These dopants result in a lower band gap which extends the absorbtion into the visible light region.

$TiO_2$ can also be combined with other oxides such as $SiO_2$ and $Al_2O_3$. This combines the adsorptive properties of the $SiO_2$ and $Al_2O_3$ with the photocatalytic properties $TiO_2$, resulting in an overall enhanced photocatalyst [118, 119]. Organic materials such as salicylic acid do not readily adsorb onto $TiO_2$ alone. The thin layer of $SiO_2$ and $Al_2O_3$ keeps the organic material in close proximity to the $TiO_2$ and reduces the chance of wasted electron-hole recombinations.

Another technique involves using a material to upconvert a longer wavelength of light into a lower wavelength. For example $YF_3$:$Yb^{3+}$, $Tm^{3+}$ can be used to upconvert near-infrared into ultraviolet and blue emissions [120]. $TiO_2$ can then be coated onto cores of this material to make use of the upconverted near ir light [121]. The mechanism behind this conversion involves pumping electrons up through multiple energy states with each jump being a lower energy differential than that of the incoming photons. When the electrons eventually relax again they have a chance of falling past multiple energy states and thus emitting a lower wavelength of light.

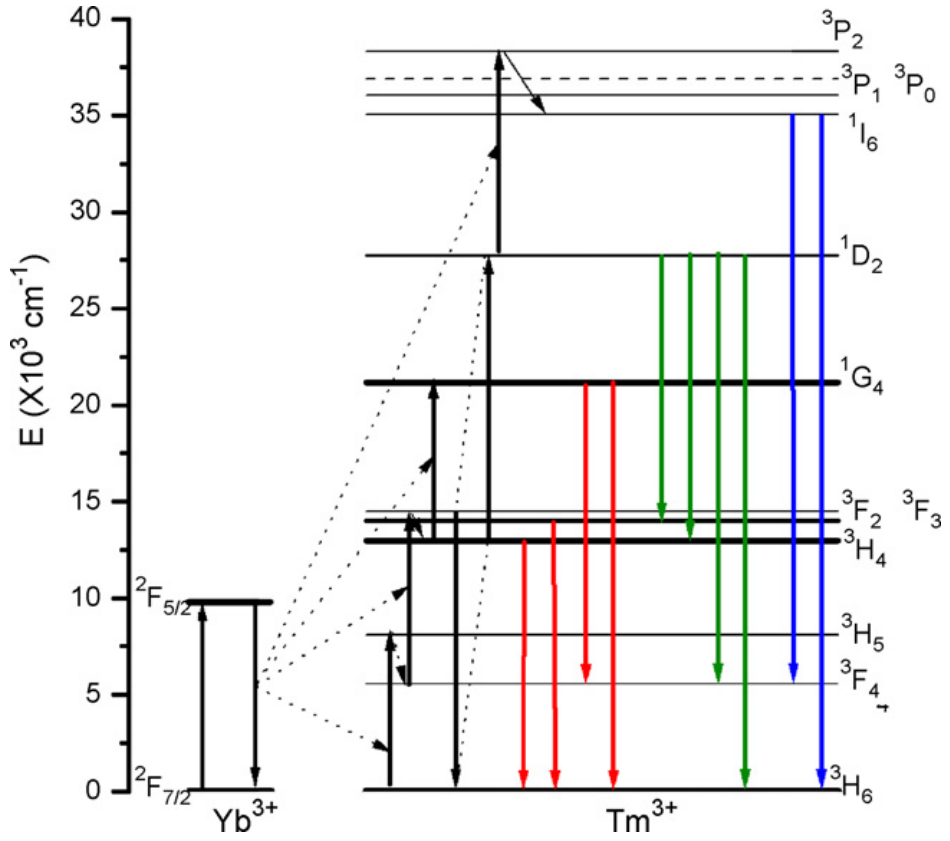


Fig. 7.3 Upconversion mechanism of $Yb^{3+}$-sensitized $Tm^{3+}$ emissions in $YF_3$:$Yb^{3+}$(20%)/$Tm^{3+}$(1%) nanobundles [120]. Absorbtion of multiple photons pushes the energy of the electron through multiple states (black). They can then later fall through multiple states emitting a lower wavelength photon (red, green and blue).

## 7.2 Desensitisation of $TiO_2$

For certain applications we are only interested in the optical properties of $TiO_2$ such as its ability to block UV light, but the photocatalytic properties are undesirable as this can cause

discolouration of the pigment as well as degredation of the binder. Discolouration is caused by a particular reduction reaction which leads to the formation of $Ti^{3+}$ centers. Since $Ti^{3+}$ is a violet coloured species some discolouration, otherwise known as graying, might be observable [122–124]. To reduce this activity there are a few treatments available [124]:

- Coating the surface of titanium dioxide particles with dense dielectric layer to prevent the charge transfer from $TiO_2$ surface to the binder molecule.
  - $SiO_2$ [13, 125, 126]
  - Phosphates of some metals [127]
- Coating the surface of titanium dioxide particles with materials, providing the capture of $TiO_2$ photocatalytic activity products ($^{\bullet}OH$, $^{\bullet}O_2{}^{-}$, $^{\bullet}O_2H$ radicals) and their subsequent mutual annihilation.
  - Metal oxides / hydroxides, e.g., Zr [128]
  - Phosphates of some metals [122]
- Doping of $TiO_2$ lattice with atoms of other elements to create traps for excitons (migrating electron-hole pairs within the crystal) with a view to reduce the number of excitons reaching the surface of titanium dioxide particles.
- Introducing inhibitors to pigments to prevent the formation of $Ti_3{}^{+}$.

## 7.3 Method

This experiment focuses on a range of $TiO_2$ materials including both rutile and anatase phases, and varying pigmentary properties. These are all provided by Kronos, and a photo as well as a summary of the powder properties is shown in figure 7.4.


Fig. 7.4 Photograph of various $TiO_2$ powders.

| Name | Phase | Purity | Description |
|---|---|---|---|
| Kronos 3000 | Anatasae | >99% | Granular anatase without pigmentary properties. |
| Kronos 1002 | Anatase | >99% | Pigment grade anatase. |
| Kronos 1171 | Anatase | >99% | Food safe anatase pigment. |
| KronoClean 7000 | Anatase | >87.5% | Optimised for high photoactivity, including visible light. |
| Kronos 3025 | Rutile | >99% | Coarse rutile without pigmentary properties. |
| Kronos 2220 | Rutile | >92.5% | Surface treatment of aluminium, silicon and polysiloxane compunds. Designed for high durability and very good optical properties. |

Table 7.1 Summary of $TiO_2$ pigments

The samples were scanned by Merck using a scanning electron microscope to understand their morphology. These images are shown in figure 7.5.

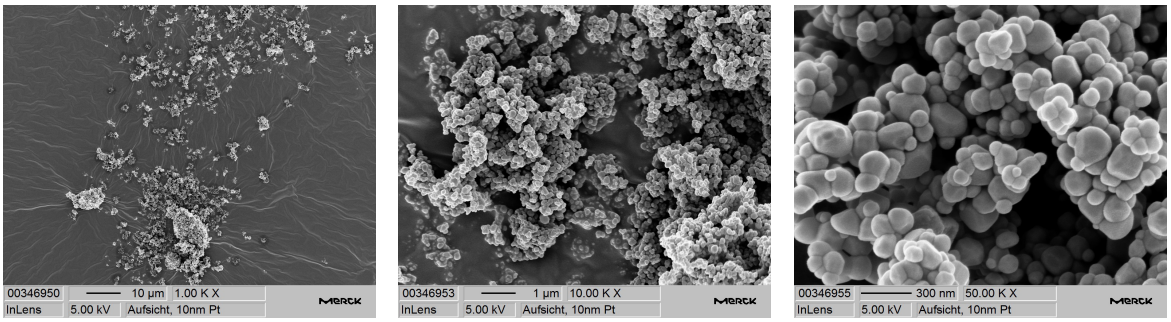


Fig. 7.5 SEM images of Kronos 3000.

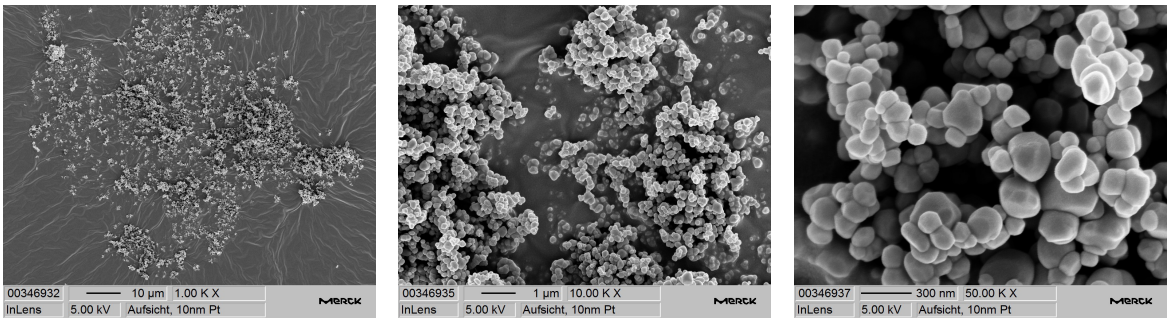


Fig. 7.6 SEM images of Kronos 1002.

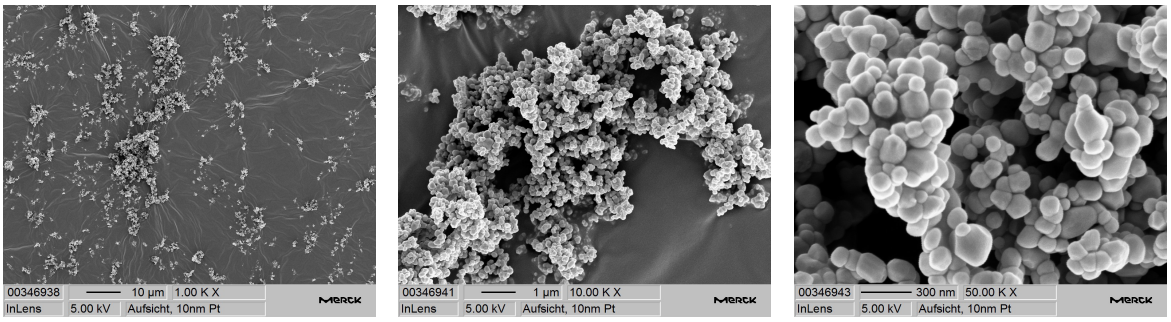


Fig. 7.7 SEM images of Kronos 1171.

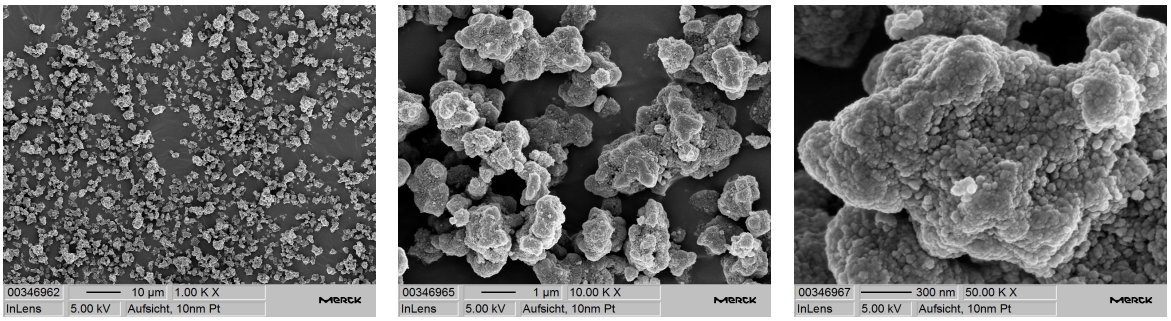


Fig. 7.8 SEM images of Kronoclean 7000.

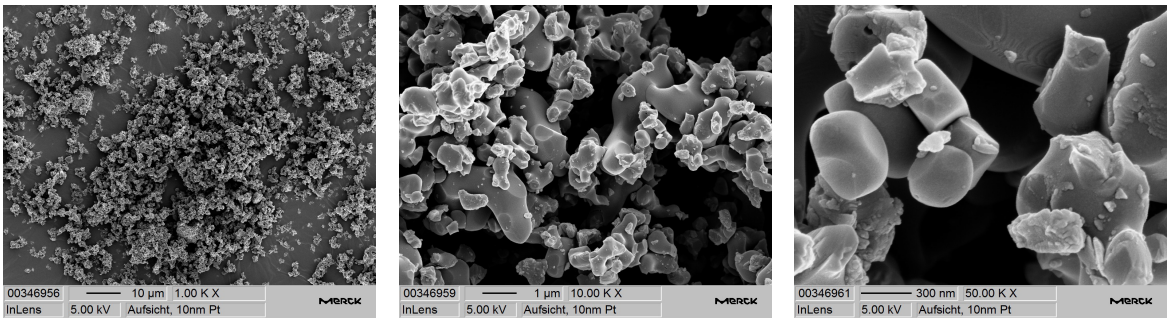


Fig. 7.9 SEM images of Kronos 3025.

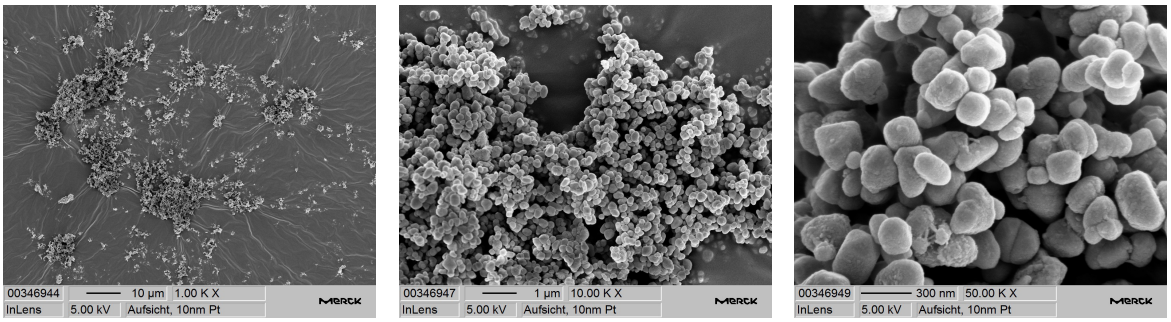


Fig. 7.10 SEM images of Kronos 2220.

Merck also provided UV-vis data of the samples, shown in figure 7.11.

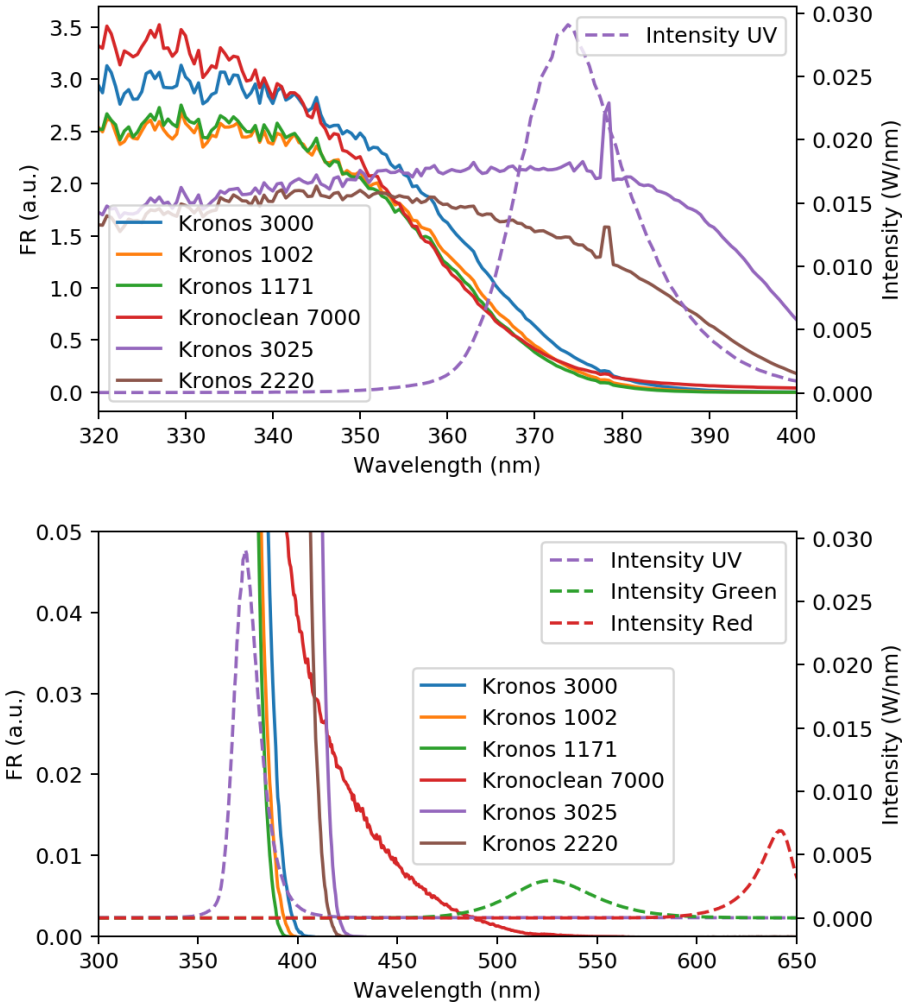


Fig. 7.11 UV Vis transmission measurements of the $TiO_2$ powders.

To further understand the sample composition, 3 of the powders were kindly analysed using X-Ray Powder Diffraction (XRD) by Andrea Folli's team from Cardiff University's Chemistry department. The full XRD plots are shown in appendix C, however a summary is shown below:

**Kronos 3000** Anatase is the only detectable phase and the crystallite size (i.e. primary particle size) is 105 +/- 2 nm.

**Kronos 3025** Rutile is the only detectable phase and the crystallite size is 157 +/- 2 nm.

**Kronoclean 7000** Anatase is the only detectable phase and the crystallite size is 22 +/- 2 nm. This sample also has C doping.

It's noted that the error on the particle size is not indicative of the actual particle size distribution, rather the error in the calculation of the particle size when the experimental patterns were fitted. Also of interest is that the XRD pattern of rutile Kronos 3025 could be refined with isotropic particle geometry (aka sphere-like particles), however the two anatase samples had to be refined considering anisotropy of the particle morphology. In particular for the Kronoclean 7000 morphology seems to be typical of crystals elongated along one preferred crystal direction.

The pigment powders are loosely packed into 2.0mm inner diameter quartz tubes bought from CM Scientific and settled using vibrations. One tube is prepared for each combination of pigment and exposure wavelength to ensure that all samples started at the same known state. The following wavelengths were used:

- 365nm Ultraviolet
- 523nm Green
- 623nm Red

To account for any changes in the microwave cavity temperature, the temperature correction technique from chapter 3 was used. Figure 7.12 shows the first order linear curve fit of the reference measurements taken after each batch of samples:

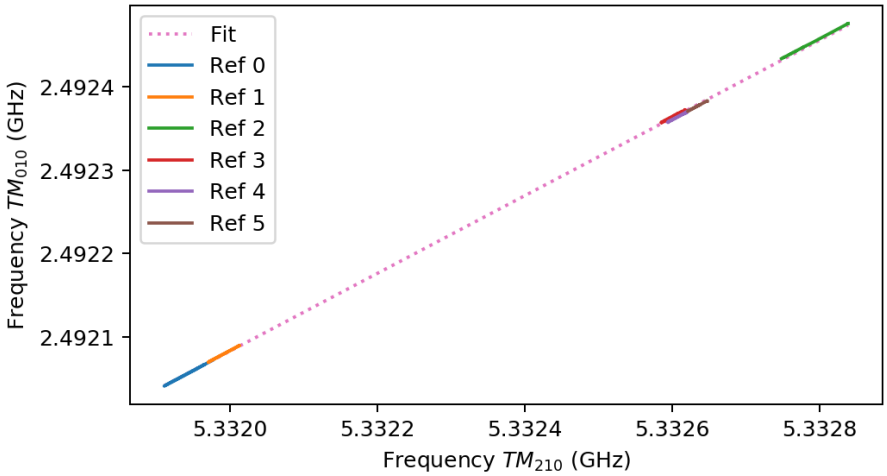


Fig. 7.12 Curve fit of reference measurements to calculate the empty $TM_{010}$ state from $TM_{210}$

As expected there is a very good correlation between the $TM_{210}$ and $TM_{010}$ modes which should yield a good temeprature correction. It unfortunately won't be able to account for

any changes in the tempearture of the samples themselves as this is intrinsically linked to the sample properties.

For each measurement the samples are exposed for 5 minutes, and then left to rest for 10 minutes. Measurements will be happening continuously throughout.

The samples were also exposed to humidity using the setup shown in figure 7.13. A saturated solution of potassium nitrate was used to bring the humidity to 95%. Once the value had been reached, data logging was started and the saturated salt was replaced with dry lithium chloride to dry the air as quickly as possible. Measurements continued until changes in the sample properties had stabilized.

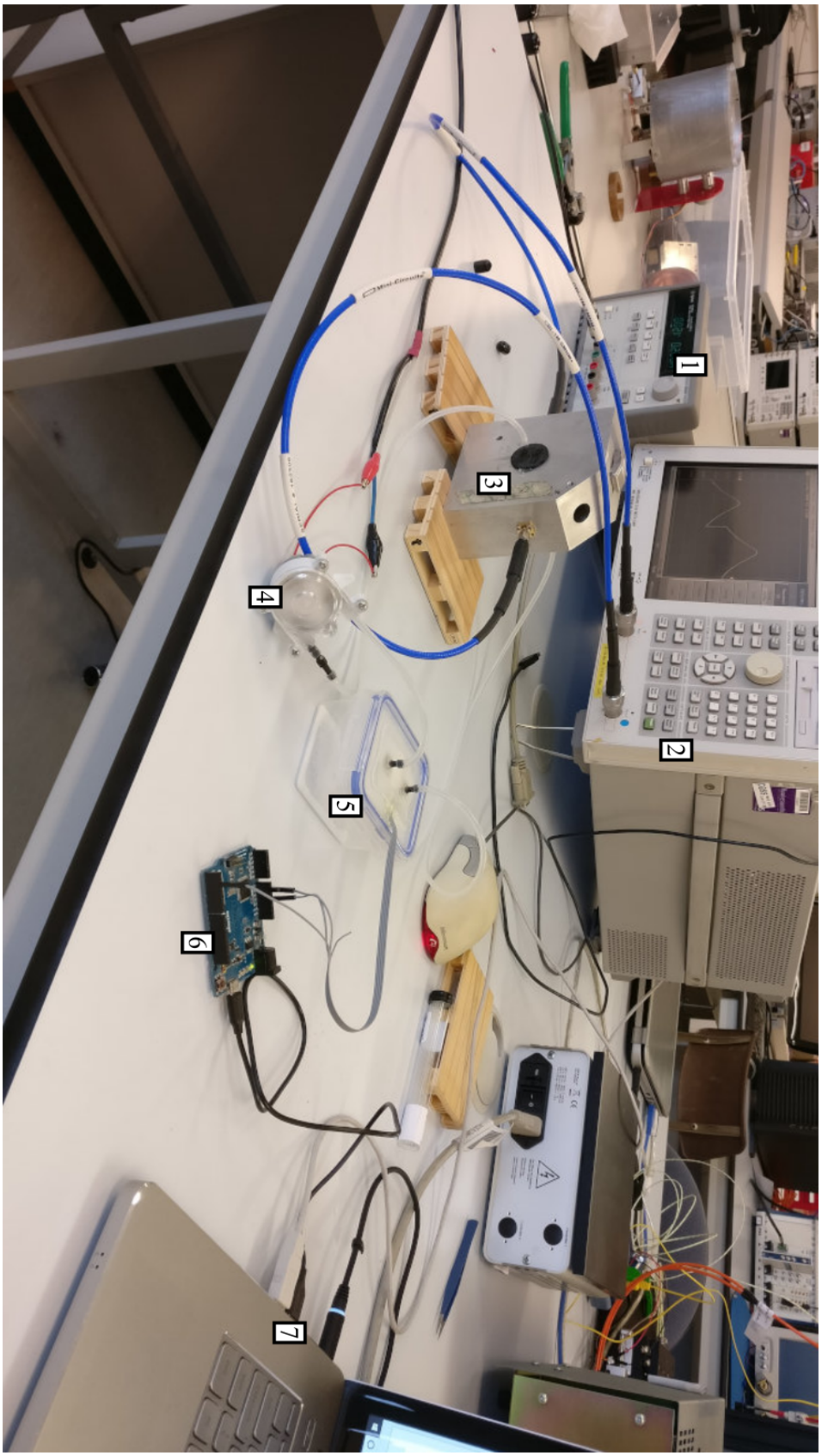


Fig. 7.13 Humidity experiment setup.

The components of the setup are detailed below:

1. DC power supply.
2. Vector Network Analyser.
3. Microwave resonant cavity with quartz sample tube through centre. The sample tube was plugged with quartz wool to contain the powder, but to allow air to pass through.
4. Peristaltic pump with input connected to the quartz sample tube and output connected to the salt container.
5. Salt container for various saturated or dried salts depending on desired humidity. The container also includes a DHT22 humidity and temperature sensor with the power and data lines sealed into the lid.
6. Arduino Leonardo to convert the DHT22 sensor readings into a serial output which can then be datalogged by the instrument control software.
7. Laptop for running the instrument control software which orchestrates the entire experiment.

## 7.4 Results

### 7.4.1 Light Measurements

The absolute permittivity changes are shown in figure 7.14.

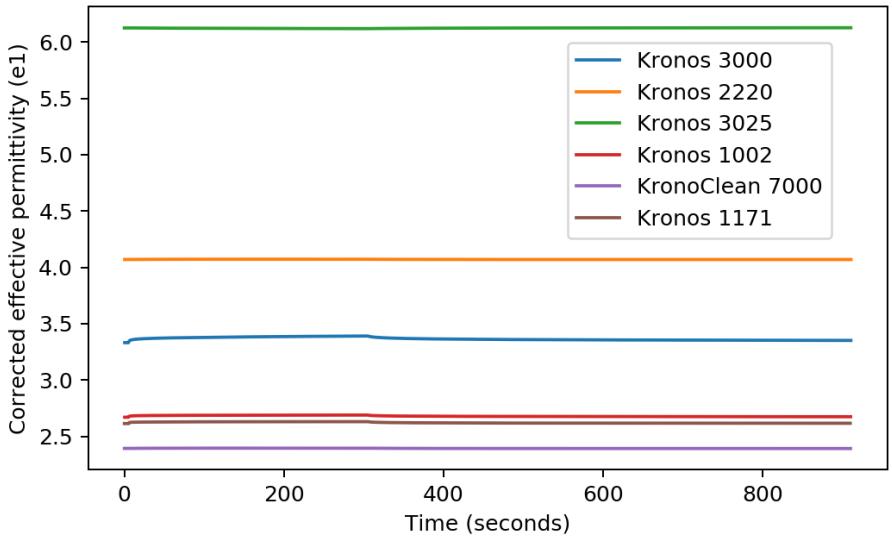


Fig. 7.14 Corrected absolute change in effective permittivity when exposed to ultraviolet light.

Unfortunately due to the large variations in initial permittivity, it is difficult to see the changes in the samples over time. For this reason, all the following permittivity figures are plotted as percentage changes relative to the sample's initial permittivity at time $t = 0$.

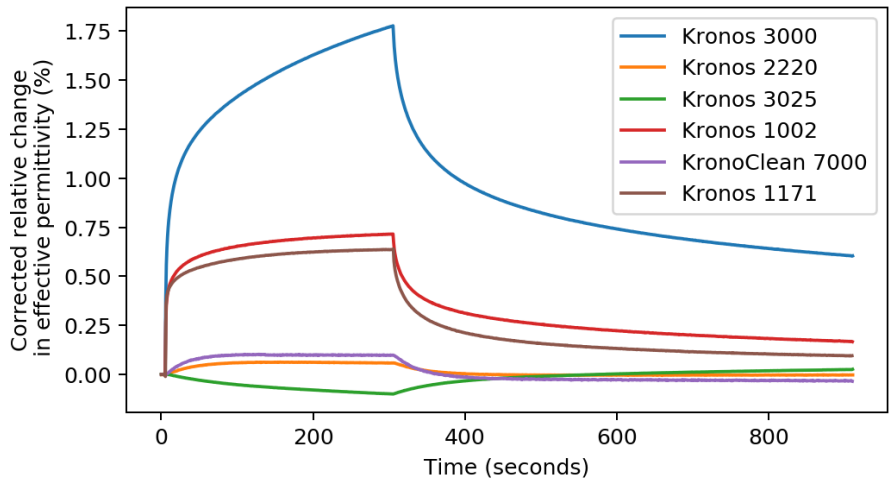


Fig. 7.15 Corrected relative change in effective permittivity when exposed to ultraviolet light.

Here, Kronos 3000 was the most reactive followed by Kronos 1002 and 1171. Kronos 3025 showed an unusual inverse response to the UV light. Kronos 2220 and Kronos 7000 showed the smallest response.

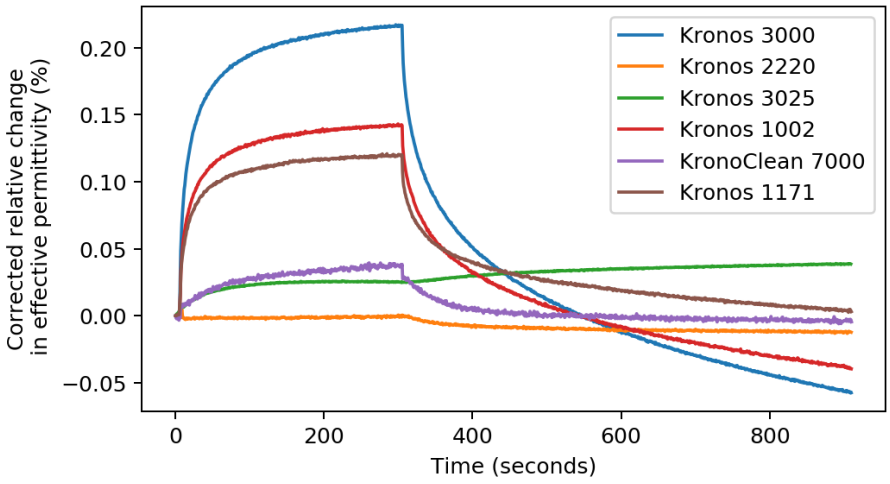


Fig. 7.16 Corrected relative change in effective permittivity when exposed to green light.

The response to green light is an order of magnitude smaller overall than for the UV light. Kronos 3025 is again showing some unusual behaviour.

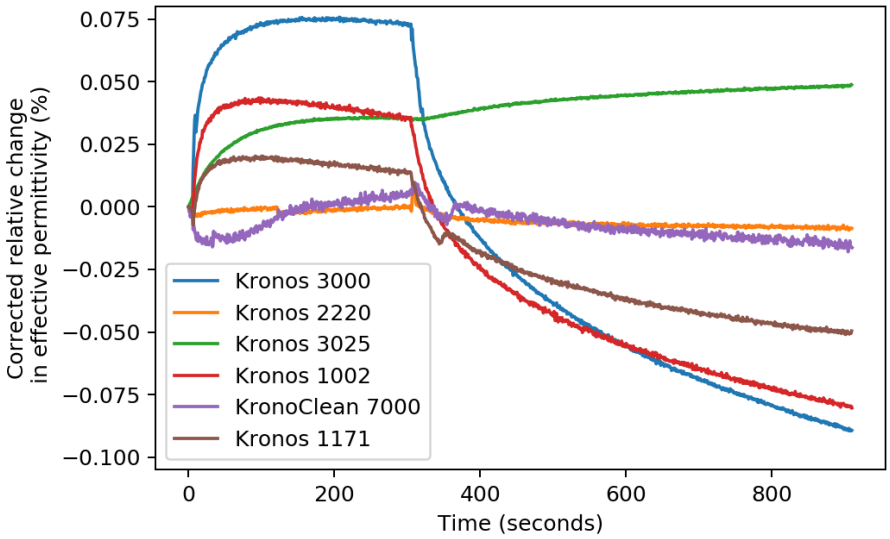


Fig. 7.17 Corrected relative change in effective permittivity when exposed to red light.

Finally, red light shows the smallest change of them all except for Kronos 3025 which is similar to the response to green light. A lot of the samples also end up with a larger permittivity than what they started with.

We can also look at the change in loss of the samples. This represents how much of the microwave energy is being absorbed by the sample.

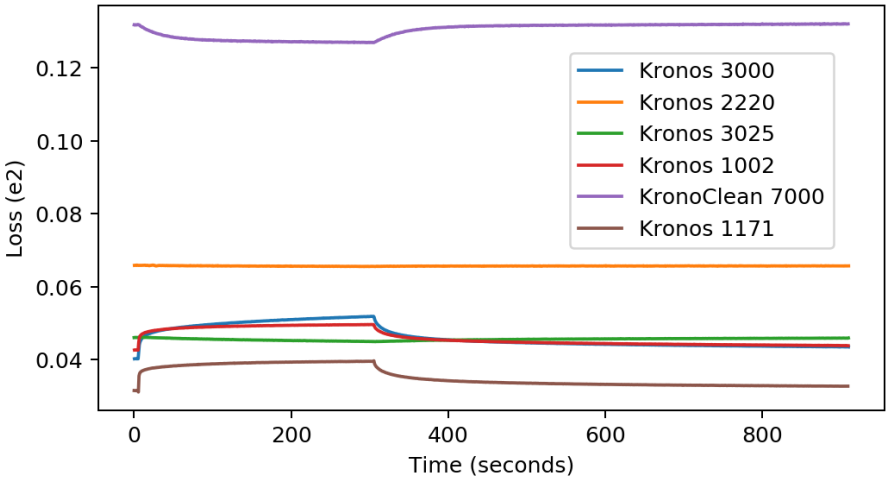


Fig. 7.18 Absolute loss value when exposed to ultraviolet light.

Again, to be able to see the changes more clearly all the following figures are plotted as percentage changes relative to the sample's loss at time $t = 0$.

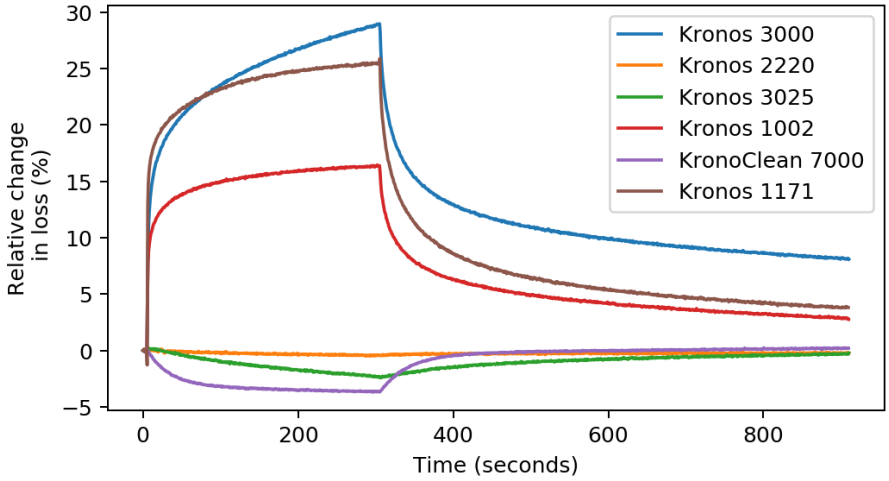


Fig. 7.19 Relative change in loss when exposed to ultraviolet light.

When exposed to ultraviolet light Kronos 3000 is again the most reactive, however Kronos 1171 has a faster response time. KronoClean 7000 and Kronos 3025 both show a reduction in loss when exposed, and Kronos 2220 is mostly unchanged.

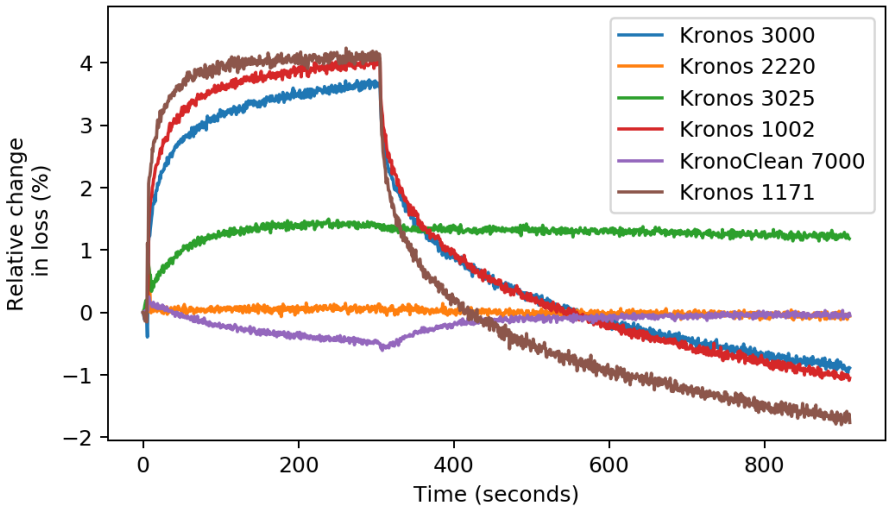


Fig. 7.20 Relative change in loss when exposed to green light.

When exposed to green light, again most samples have a response an order of magnitude smaller than ultraviolet light. Kronos 3025 now shows an increase in loss. Also Kronos 3000, 1002 and 1171 all have a final loss smaller than their initial value.

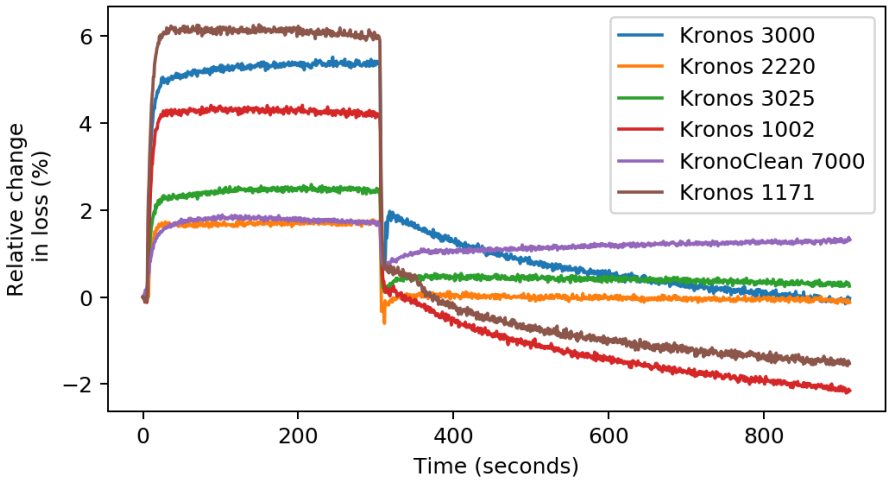


Fig. 7.21 Relative change in loss when exposed to red light.

When exposed to red light the response times are faster than with green or ultraviolet light with some slight overshoot in the Kronos 3000, Kronos 2220 and KronoClean 7000 samples when the light is turned off.

### 7.4.2 Heat Measurements

The samples were also exposed to heat via a hot air gun to attempt to separate thermal from optical properties. The relative permittivity and loss results are shown in figures 7.22 and 7.23.

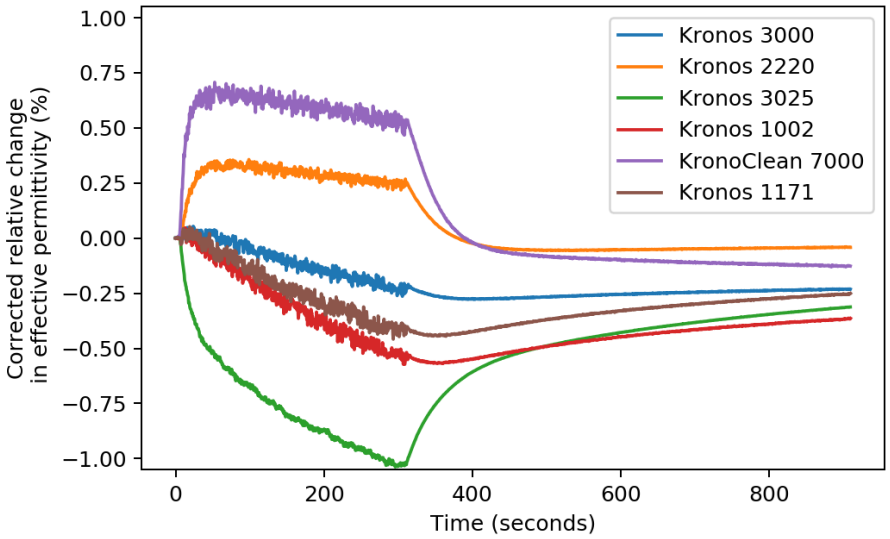


Fig. 7.22 Corrected relative change in effective permittivity when exposed to heat.

Both Kronoclean 7000 and Kronos 2220 showed an increase in effective permittivity when exposed to heat whereas all the other samples showed a decrease with Kronos 3025 being the most significant. The noise seen during the heating stage is likely due to the turbulent hot air in the cavity.

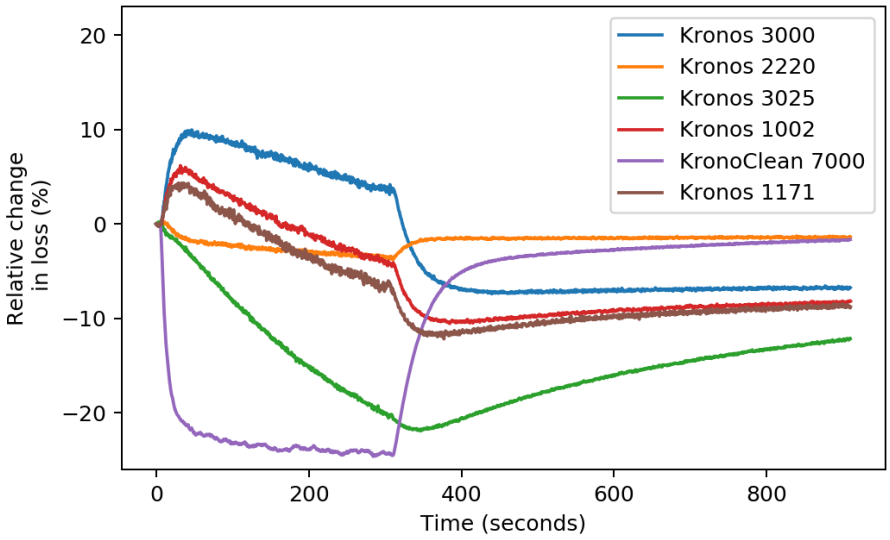


Fig. 7.23 Relative change in loss when exposed to heat. Heat was applied at time $t = 0$ and removed at time $t = 300$.

All 3 of the pure anatase samples showed an initial increase in loss before slowly decreasing again. Kronos 2220 showed an initial decrease before stabilizing, and a rise again when the heat was removed. Kronos 3025 showed a steady decrease in loss during heat exposure, then a slower recovery. Kronoclean 7000 was the most dramatic of all the samples showing an almost 25% sharp drop in loss on application of heat. The recovery was slower, but still got close to the sample's initial starting contition.

### 7.4.3 Humidity Measurements

Humidity is also a factor which can affect the samples, and so this was also analysed using the setup described in the method section.

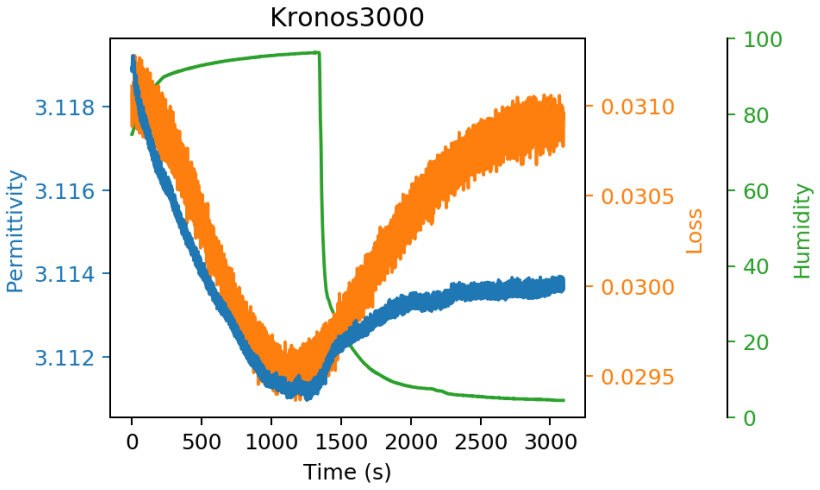


Fig. 7.24 Change in permittivity and loss in Kronos 3000 as a function of humidity.

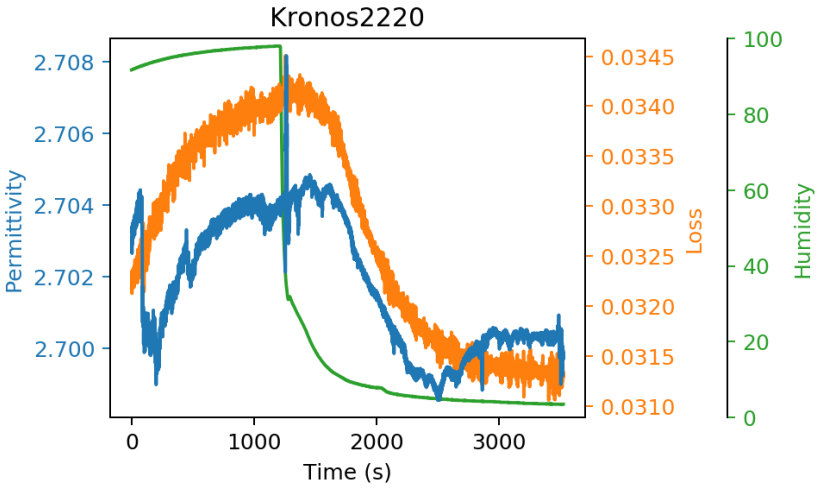


Fig. 7.25 Change in permittivity and loss in Kronos 2220 as a function of humidity.

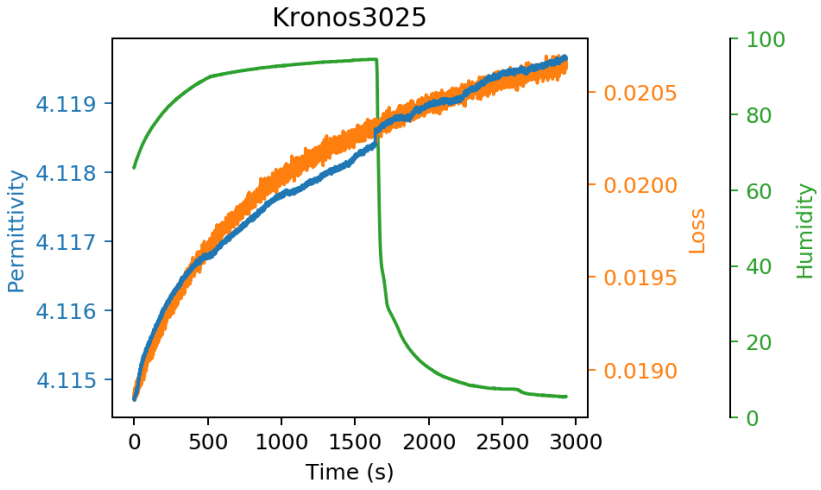


Fig. 7.26 Change in permittivity and loss in Kronos 3025 as a function of humidity.

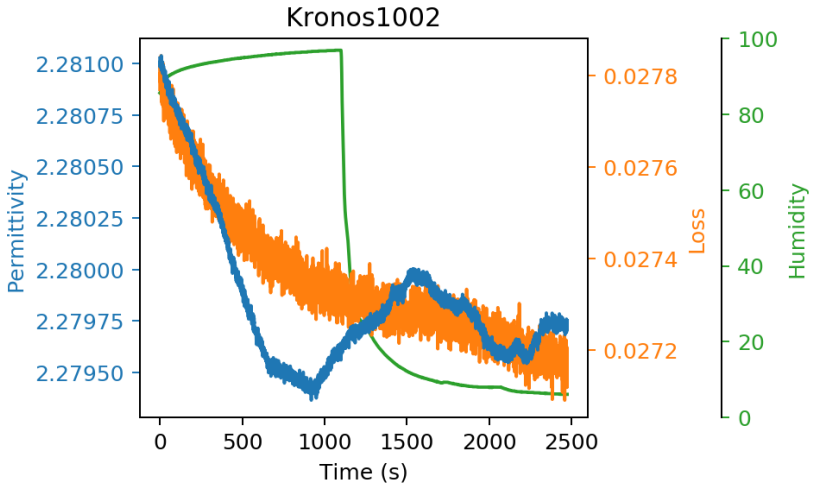


Fig. 7.27 Change in permittivity and loss in Kronos 1002 as a function of humidity.

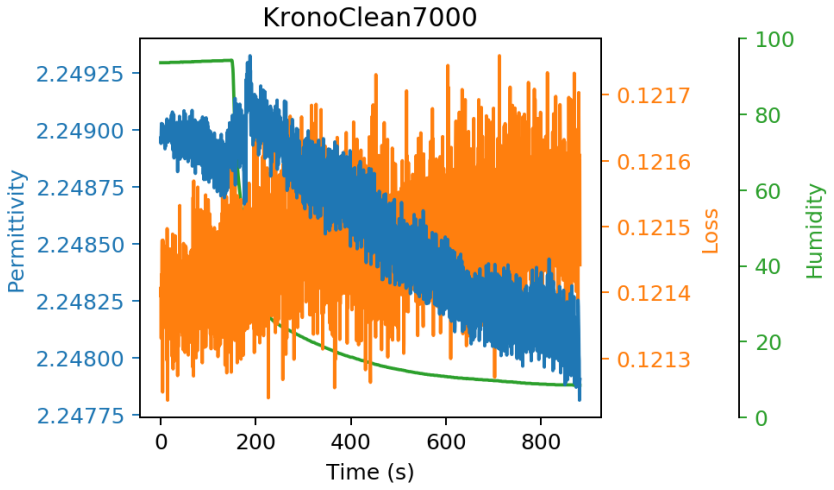


Fig. 7.28 Change in permittivity and loss in Kronoclean 7000 as a function of humidity.

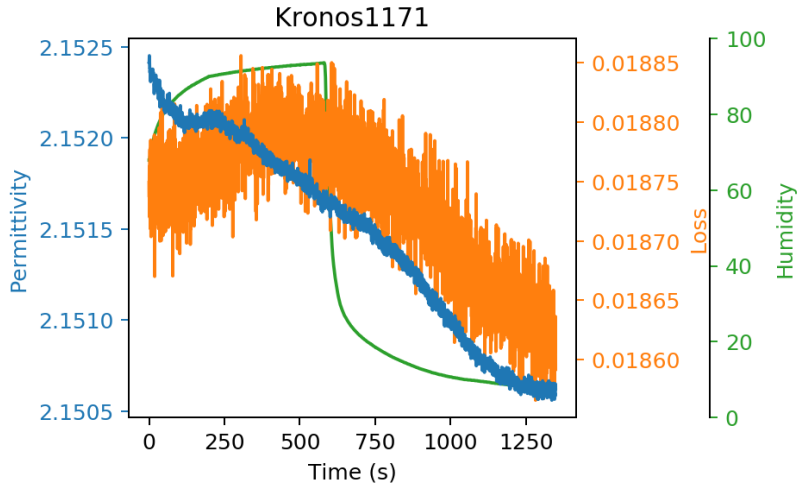


Fig. 7.29 Change in permittivity and loss in Kronos 1171 as a function of humidity.

Unfortunately the previous graphs were mostly inconclusive. Firstly many of the samples had not reached equilibrium when the humidity was as its highest, so it's not possible to know the true starting humidity of the sample. Also some samples such as Kronos 3025 continued to show an increase in permittivity and loss completely independently of the humidity suggesting other systematic errors are seriously interfering with the results. This could be ambient temperature fluctuations, or possibly even the airflow through the sample causing movement of the powder grains.

## 7.5 Discussion

### 7.5.1 Pure Anatase Versus Pure Rutile

It is generally accepted in the literature that pure anatase is a more effective photocatalyst than pure rutile. For example, an experiment by Tim Luttrell measured the photocatalytic activity $TiO_2$ by measuring the decomposition rate of methyl orange [98]. Rajesh J. Tayade also looked at the degredation of acetophenone, nitrobenzene and malachite green, and found similar results [129].

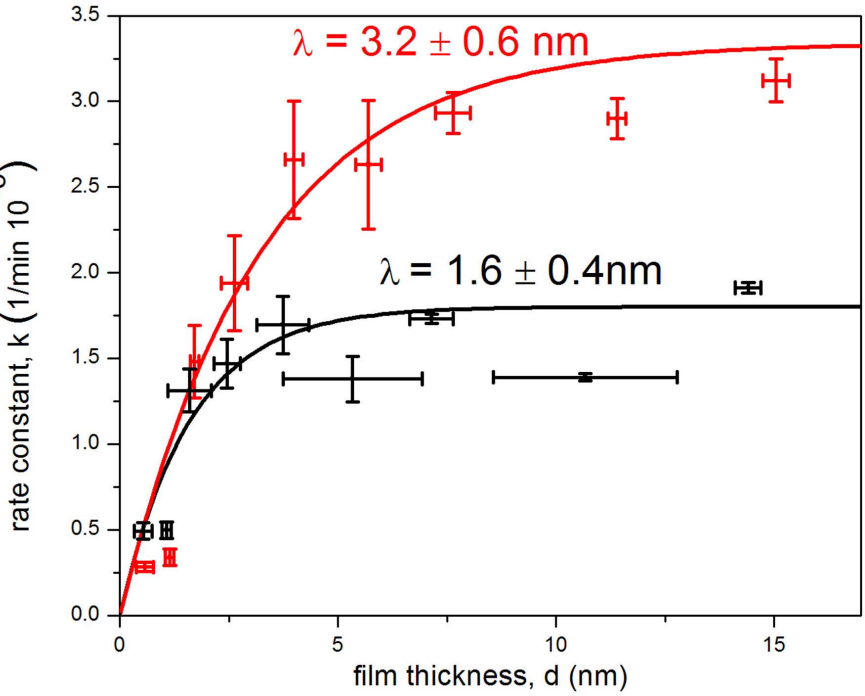


Fig. 7.30 Film thickness vs reaction rate of anatase (red) and rutile (black) thick films [98].

This correlates with the microwave measurements of the pure anatase and rutile under UV light, especially figure 7.19 which shows a larger increase in loss of Kronos 3000, 1002 and 1171 compared to Kronos 3025. An increase in loss is suggestive of an increase in conductivity which is expected due to the increased number of charge carriers when exposed to ultraviolet light. Kronos 3025 actually shows a decrease in loss when exposed to UV light, however this may also be thermal effects as shown in figure 7.23.

### 7.5.2 Semi-permanent Changes Under UV Light

All of the pure anatase samples showed a semi-permanent change when exposed to UV light. The rutile samples and the photocatalytic grade $TiO_2$ on the other hand mostly returned to their original state. The most likely cause of these changes is the formation of $Ti^{3+}$. That being said, literature has shown $Ti^{3+}$ generation in rutile samples too [130], however it may be the the duration of the experiment is not long enough for these effects to become visible. It would also be interesting to repeat these experiments in an oxygen free environment to see if these semi-permanent changes are still present. It is expected that the lack of oxygen will enhance the formation of the $Ti^{3+}$ centres, and if this is the cause of the semi-permanent changes then the samples should reach an excited state sooner [131].

### 7.5.3 Photocatalytic Grade $TiO_2$ Results

From the XRD measurements it is shown that Kronoclean 7000 is a pure anatase pigment with approximately 22nm particle size and C doping. As discussed in section 7.1.2 C doping is one such technique for sensitising $TiO_2$ to visible light. This can be seen in the UV-Vis data in figure 7.11 where the Kronoclean 7000 shows absorbtion up to 500nm. Rather surprisingly is that the relative changes in permittivity and loss are rather small in comparison to other anatase samples. That being said, when we analyse the absolute loss value in figure 7.18 it can be seen that Kronoclean 7000 has a far higher loss than any other sample. This indicates that the sample is alredy in a highly excited state, and so additional illumination provides minimal additional charge carriers. In figure 7.19 the loss is also shown to be decreasing during exposure, however this is also seen in the thermal only results in figure 7.23. This suggests that the thermal heating caused by the UV exposure is outweighing any increase in conductivity from additional carrier generation.

Unfortunately there were very minimal changes observed when exposed to green and red light, however when analysing the UV-vis results in figure 7.11 this comes as no surprise since both these wavelengths are just outside the absorbtion range of the Kronoclean 7000 sample. In hindsight it would have been useful to analyse another wavelength between the UV and green LEDs to see if this nitrogen doping does indeed provide visible light photocatalysis.

### 7.5.4 Surface Treated Rutile

The surface treated rutile samples behaved as expected, showing almost no change in loss when exposed to UV light. There was a small change in permittivity, however this could be due to thermal effects as seen in figure 7.22. It would be interesting to perform this experiment over a longer duration, for example a few days to see if this is still the case as some literature has alluded to the common modifications not being suitable for long term exposure [122].

### 7.5.5 Effects of Humidity on the Electrical Properties of $TiO_2$

Unfortunately most of the humidity measurements were inconclusive. These experiemnts were performed in a darkened microwave resonant cavity, so it's likely that chemisorption of water was minimal. If this experiment were to be performed again then better control of the initial parameters is required, in particular complete drying of the $TiO_2$ samples at an elevated temperature. It would also be interesting to investigate the effect of humidity on the change in electrical properties during UV exposure since $H_2O$ does play a role in the photocatalytic reactions [101].

## 7.6 Conclusion

This chapter has investigated the electrical properties of various $TiO_2$ samples when exposed to light, heat and humidity. The samples were placed in the electric field of a microwave resonant cavity and measured at 2.5GHz. During exposure to UV light for 10 minutes, pure anatase was found to be more photoactive than pure rutile. N doped anatase with a smaller crystal size didn't show a significant change to UV light however its initial loss was far greater than the other samples which suggests the samples was alredy saturated from the ambient light. This can be seen in the UV vis results where the samples is absorbing up to 500nm. The changes from red and green light for all samples were significantly lower than that of UV.

The heat measurements on their own were not particularly useful, however they were able to explain some unusual behaviour where the samples's loss decreased instead of increasing since the temperature results also showed the same trend during heating. This suggests that the LEDs are heating the samples to some extent.

Unfortunately the humidity results were not very conclusive. More controlled experiments need to be performed including full drying of the sample beforehand. It would also be interesting to investigate the effect of humidity on the UV exposure measurements.

# Chapter 8

# Final Remarks

## 8.1 Chapter conclusions

### 8.1.1 Microwave Measurement Theory

Chapter 2 introduces the concepts of microwave measurement theory. This includes how a material responds to an applied electric field where electron movement results in a reduced electric field within the sample as well as absorbtion of some of the field energy. This polarization and loss can be measured by placing the sample within a microwave resonant cavity. The electric and magnetic field patterns can be controlled by modifying the cavity geometry. A sample inserted into the resonant cavity at a region of high electric field will cause a shift in resonant frequency and bandwidth of the resonant mode which, after calibration, can be used to calculate the permittivity and loss of the sample.

### 8.1.2 Temperature Correction Methodology

Chapter 3 presents a simplified approach to temperature correcting microwave resonant cavity measurements. Traditionally temperature correction would rely on the relationship between the cavity dimensions and resonant frequency, however this gets complicated when accounting for unexpected cavity distortion such as splits and dissimilar metals. The simplified technique takes an analytical approach by plotting the relationship between a measurement mode and unperturbed reference mode during an empty cavity sweep. A curve fit function can then be calculated and used during measurements to calculate the corrected relative frequency shift which is required for calculating effective permittivity.

Another novel temperature correction method was described which places a sample off-axis in a cylindrical resonant cavity. This causes the two frequencies of a degenerate resonant mode to separate, of which one can be used for sample measurement, and the other as a reference. This was verified using water which showed the technique to be very effective.

### 8.1.3 Instrument Control Software

Chapter 4 describes the design of an instrument control program which can be used to control multiple instruments simultaneously, for example a VNA, DC power supply and temperature probe. The software architecture was designed to place each instrument in a separate thread, and use queues to pass data and commands to/from the main user interface thread. The UI thread also periodically saves the data to a standard csv file format.

The VNA driver was described which supports a range of hardware. Multiple frequency ranges can be measured and a tracking algorithm was described which ensures that the resonant peak always remains in the centre of the measurement window.

The generic instrument scripting driver was described which allowed automated commands to be sent to any VISA compatible instrument such as a DC power supply.

Finally a temperature logging driver was described which interfaces with the RS-pro data-loggers and uses a custom binary protocol.

### 8.1.4 Design of a Resonant Cavity for Light Exposure of Sheet Materials

Chapter 5 describes the design of a custom rectangular microwave resonant cavity designed for measuring foil samples, lacquer with pigment coated onto acetate sheets, while being exposed to light of various wavelengths. Microwave simulations and light intensity calculations were performed to verify the design before being manufactured. After manufacturing, the performance of the cavity was measured to ensure it would work as expected during measurements of the real samples.

### 8.1.5 Properties of Iriotec® 7000 Pigment Powders When Exposed to Light

Chapter 6 uses the previously described rectangular resonant cavity to measure six Iriotec® 7000 foils. These contain ATO coated onto various substrates such as mica sheets and quartz/talcum spheres, all dispersed in a lacqeur. It was observed that the larger particle sizes were the most dominant contribution towards increased conductivity, however the platelet/sphere interaction did provide a small increase too.

The realtime response of the samples was also analysed, and it was discovered that two separate mechanisms were in effect during exposure. It is suspected that this is a combination of charge being trapped in the substrate/lacqeur and surface defects in the ATO coating causing oxygen vacancies which will also act as traps. The lowest doped sample showed a far greater proportional change compared to the higher doping levels which is likely due to a larger chance of holes being scavenged due to fewer free electrons.

A semi-permanent change was also observed in the samples, both in the microwave measurements and a colour change in the samples. Heating of the samples restored them to their original state which is explained by a higher oxidation state being a thermally driven relaxation process.

### 8.1.6 Light Exposure of Titanium Dioxide

Chapter 7 exposed various $TiO_2$ samples to light, heat and humidity. Pure anatase was found to be more photoactive than pure Rutile, and a surface treated Rutile for high stability showed almost no change whatsoever. An N doped Anatase pigment also didn't show much change to UV light, however it had a far higher loss indicating it was already fully excited from ambient light.

The heat measurements explained any anomalies caused by temperature changes induced by the LEDs. Unfortunately the humidity measurement were not very conclusive, most likely due to poorly controlled initial conditions.

## 8.2 Future Work

Both the $TiO_2$ and Iriotec® 7000 experiments described in this thesis involve interactions between carrier generation and trapped states. Electron Paramagnetic Resonance (EPR)

spectroscopy is a method for studying materials with unpaired electrons, and would be ideal for analysing the trapped states of these materials. EPR systems consist of a large electromagnet to vary the magnetic field strength through the sample and a microwave resonant cavity to store microwave energy which is used to excite the electrons between their two spin states. A schematic of this is shown in figure 8.1.

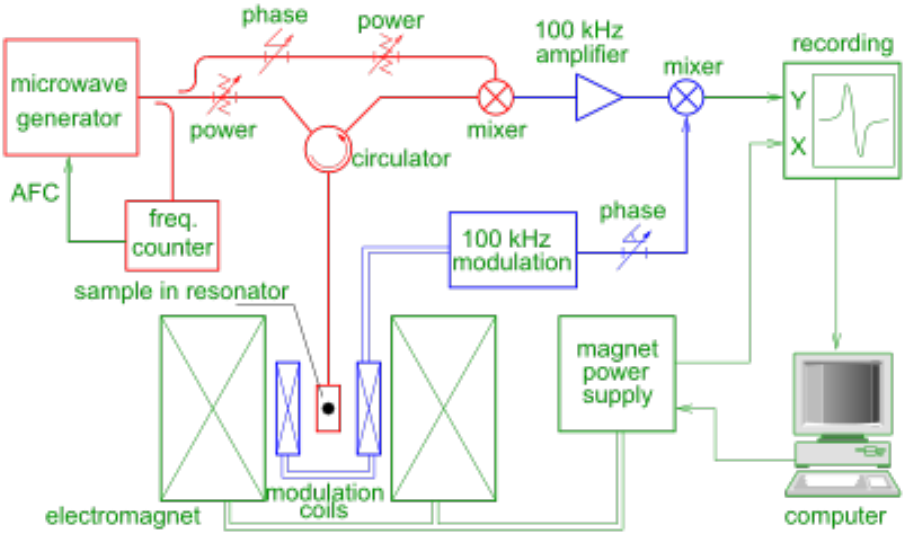


Fig. 8.1 Schematic showing a typical continuous wave EPR spectrometer setup [132].

It may be possible to modify this technique to perform simultaneous EPR and microwave cavity perturbation measurements using multiple resonant modes. Typically a waveguide is used to supply electromagnetic energy to and from the resonant cavity. A suitable waveguide dimension can be chosen to act as a high pass filter, preventing a lower frequency perturbation mode from interfering with the EPR measurement.

It would also be interesting to analyse the effect of environmental conditions on the samples during exposure. In particular the oxygen concentration and humidity. The literature has shown that both of these play some role in photocatalysis, and so it would be intersting to see if the lack of oxygen and or moisture results in a reduced sample response as well as a reduction in any semi-permanent changes. The humidity setup in figure 7.13 of chapter 7 can be modified to introduce an argon or other inert gas feed to purge oxygen out of the system. A schematic of this is shown in figure 8.2.

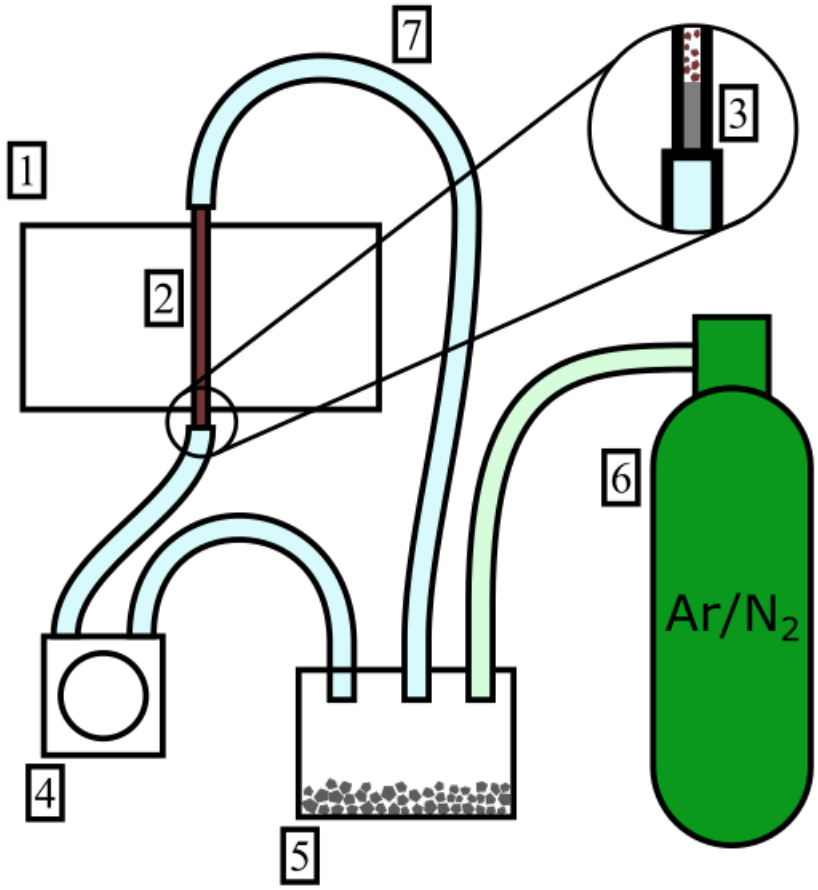


Fig. 8.2 Microwave cavity resonator setup with dry and oxygen free air flowing through sample tube.

- Cylindrical microwave resonant cavity.
- Quartz capillary containing sample to be measured.
- Quartz wool plug to prevent powder from falling out of the tube while allowing air to pass through.
- Peristaltic pump to slowly circulate air through the system.
- Container with dessicant or saturated salt depending on desired humidity.
- Argon or Nitrogen cylinder to purge oxygen out of the system. The pressure should be set to slightly above atmospheric to prevent oxygen from entering through any leaks.
- Silicone tubing to connect the various components of the system. 2mm ID tubing fits snugly over 2.5mm OD quartz capillaries.

Finally it would be interesting to perform a more focused analysis of the doping level of the Iriotec® 7000 pigments on the electrical response during exposure. The experiments suggested that lower n-type doping levels resulted in a larger response, however this was only two samples and they were not directly comparable. As well as n-type doping it would also be interesting to investigate how p-type doping with materials such as Indium affects the samples, and whether an excess of holes results in a larger electrical response during UV exposure.

# References


[1] Gerhard Auer, Wolf-Dieter Griebler, and Burkhardt Jahn. *Industrial Inorganic Pigments, Third Edition*. Ed. by Gunter Buxbaum and Gerhard Pfaff. 3rd ed. Wiley-VCH Verlag GmbH & Co. KGaA, 2005. Chap. 2, pp. 51–97.

[2] Delgado Vargas, O Paredes López, and Francisco Delgado-vargas. *Natural Colorants for Food and Nutraceutical Uses*. Vol. 14. 10. 2003, p. 438.

[3] Devagi Kanakaraju, Beverley D. Glass, and Michael Oelgemöller. "Titanium dioxide photocatalysis for pharmaceutical wastewater treatment". In: *Environmental Chemistry Letters* 12.1 (2014), pp. 27–47.

[4] I. Michael et al. "Solar Fenton and solar $TiO_2$ catalytic treatment of ofloxacin in secondary treated effluents: Evaluation of operational and kinetic parameters". In: *Water Research* 44.18 (2010), pp. 5450–5462.

[5] Peng Sun et al. "Photocatalyst of organic pollutants decomposition: $TiO_2$ /glass fiber cloth composites". In: *Catalysis Today* 274 (2016), pp. 2–7.

[6] R. Bauer. "The photo-fenton reaction and the $TiO_2$/UV process for waste water treatment - novel developments". In: *Catalysis Today* 53.1 (1999), pp. 131–144.

[7] Changseok Han et al. "Innovative visible light-activated sulfur doped $TiO_2$ films for water treatment". In: *Applied Catalysis B: Environmental* 107.1-2 (2011), pp. 77–87.

[8] Erika Iveth Cedillo-González et al. "Self-cleaning glass prepared from a commercial $TiO_2$ nano-dispersion and its photocatalytic performance under common anthropogenic and atmospheric factors". In: *Building and Environment* 71 (2014), pp. 7–14.

[9] Y. Paz et al. "Photooxidative self-cleaning transparent titanium dioxide films on glass". In: *Journal of Materials Research* 10.11 (1995), pp. 2842–2848.

[10] Kazuhito Hashimoto, Hiroshi Irie, and Akira Fujishima. "$TiO_2$ Photocatalysis: A Historical Overview and Future Prospects". In: *Japanese Journal of Applied Physics* 44.12 (2005), pp. 8269–8285.

[11] Frank N. Jones, Mark E. Nichols, and Socrates Peter Pappas. *Organic Coatings: Science and Technology*. 4th. Wiley, 2017, p. 512.

[12] Kamil Wojciechowski et al. "Effect of $TiO_2$ on UV stability of polymeric binder films used in waterborne facade paints". In: *Progress in Organic Coatings* 85 (2015), pp. 123–130.

[13] Iqbal Ahmed Siddiquey et al. "Control of the photocatalytic activity of $TiO_2$ nanoparticles by silica coating with polydiethoxysiloxane". In: *Dyes and Pigments* 76.3 (2008), pp. 754–759.

[14] Michael Barter et al. “Temperature Correction Using Degenerate Modes for Cylindrical Cavity Perturbation Measurements”. In: *IEEE Transactions on Microwave Theory and Techniques* 67.2 (2019), pp. 800–805.

[15] David M. Pozar. *Microwave Engineering*. 3rd ed. John Wiley & Sons, 2004.

[16] K.M. Smith and P. Holroyd. *Electrical Properties of Materials*. 10th ed. OUP Oxford, 2013, pp. 165–174.

[17] G. Roussy and J.A. Pearce. *Foundations and industrial applications of microwaves and radio frequency fields*. 1st ed. Wiley, 1995.

[18] A.C. Metaxas and R.J. Meredith. *Industrial Microwave Heating*. Peter Peregrinus Ltd, 1983.

[19] Ari Sihvola. *Electromagnetic Mixing Formulas and Applications*. IET, 1999.

[20] R. B. Piejak et al. “The hairpin resonator: A plasma density measuring technique revisited”. In: *Journal of Applied Physics* 95.7 (2004), pp. 3785–3791.

[21] Paul A. Anderson et al. “Rubidium doped zeolite rho: Structure and microwave conductivity of a metallic zeolite”. In: *Journal of the Chemical Society. Dalton Transactions* 4.19 (2004), pp. 3122–3128.

[22] R. L. Stenzel. “Microwave resonator probe for localized density measurements in weakly magnetized plasmas”. In: *Review of Scientific Instruments* 47.5 (1976), pp. 603–607.

[23] Adrian Porch, Daniel I Odili, and Peter A Childs. “Microwave characterisation of carbon nanotube powders”. In: *Nanoscale Research Letters* 7.1 (2012), p. 429.

[24] Plamen Dankov et al. “Hairpin-resonator probe design and measurement considerations”. In: *Journal of Physics: Conference Series* 207 (2010), p. 012015.

[25] Jon Robert Hartley. “Simultaneous structural and dielectric measurement of ammonia storage materials”. PhD thesis. Cardiff University, 2015.

[26] Jake S. Bobowski. “Using Split-Ring Resonators to Measure Complex Permittivity and Permeability”. In: *2015 Conference on Laboratory Instruction Beyond the First Year*. American Association of Physics Teachers, 2015, pp. 20–23.

[27] Heungjae Choi et al. “Design of continuous non-invasive blood glucose monitoring sensor based on a microwave split ring resonator”. In: *Conference Proceedings - 2014 IEEE MTT-S International Microwave Workshop Series on: RF and Wireless Technologies for Biomedical and Healthcare Applications, IMWS-Bio 2014* (2015), pp. 1–3.

[28] Chieh-Sen Lee and Chin-Lung Yang. “Complementary Split-Ring Resonators for Measuring Dielectric Constants and Loss Tangents”. In: *IEEE Microwave and Wireless Components Letters* 24.8 (2014), pp. 563–565.

[29] B.R. Jean, E.C. Green, and M.J. McClung. “A microwave frequency sensor for non-invasive blood-glucose measurement”. In: *2008 IEEE Sensors Applications Symposium*. IEEE, 2008, pp. 4–7.

[30] D. C. Dube et al. “Dielectric measurements on substrate materials at microwave frequencies using a cavity perturbation technique”. In: *Journal of Applied Physics* 63.7 (1988), pp. 2466–2468.

[31] Jyh Sheen. “Measurements of microwave dielectric properties by an amended cavity perturbation technique”. In: *Measurement: Journal of the International Measurement Confederation* 42.1 (2009), pp. 57–61.

[32] Mi Lin and Mohammed N. Afsar. “A new cavity perturbation technique for accurate measurement of dielectric parameters”. In: *IEEE MTT-S International Microwave Symposium Digest* 4 (2006), pp. 1630–1633.

[33] Daniel Slocombe et al. “Microwave properties of nanodiamond particles”. In: *Applied Physics Letters* 102.24 (2013), pp. 1–5.

[34] Shihe Li, C. Akyel, and R.G. Bosisio. “Precise Calculations and Measurements on the Complex Dielectric Constant of Lossy Materials Using $TM_{010}$ Cavity Perturbation Techniques”. In: *IEEE Transactions on Microwave Theory and Techniques* 29.10 (1981), pp. 1041–1048.

[35] Heungjae Choi et al. “A novel concentration detection method of hydrogen peroxide using microwave cavity perturbation technique”. In: *2014 44th European Microwave Conference*. 1. IEEE, 2014, pp. 632–635.

[36] H.L. Thal. “Cylindrical $TE_{011}$/$TM_{111}$ Mode Control by Cavity Shaping”. In: *IEEE Transactions on Microwave Theory and Techniques* 27.12 (1979), pp. 982–986.

[37] S. B. COHN and K. C. KELLY. “Microwave Measurement of High-Dielectric-Constant Materials”. In: *IEEE Transactions on Microwave Theory and Techniques* 14.9 (1966), pp. 406–410.

[38] T. T. Grove, M. F. Masters, and R. E. Miers. “Determining dielectric constants using a parallel plate capacitor”. In: *American Journal of Physics* 73.1 (2005), pp. 52–56.

[39] Y. Kobayashi and M. Katoh. “Microwave Measurement of Dielectric Properties of Low-Loss Materials by the Dielectric Rod Resonator Method”. In: *IEEE Transactions on Microwave Theory and Techniques* 33.7 (1985), pp. 586–592.

[40] Yoshio Kobayashi and Tomohiro Senju. “Resonant Modes in Shielded Uniaxial-Anisotropic Dielectric Rod Resonators”. In: *IEEE Transactions on Microwave Theory and Techniques* 41.12 (1993), pp. 2198–2205.

[41] B.W. Hakki and Paul D. Coleman. “A Dielectric Resonator Method of Measuring In-ductive Capacities in the Millimeter Range”. In: *IRE Transactions on Microwave Theory and Techniques* 8.4 (1960), pp. 402–410.

[42] N.I. Sheen and I.M. Woodhead. “An Open-ended Coaxial Probe for Broad-band Permittivity Measurement of Agricultural Products”. In: *Journal of Agricultural Engineering Research* 74.2 (1999), pp. 193–202.

[43] Mingzhong Wu, Xi Yao, and Liangying Zhang. “Improved coaxial probe technique for measuring microwave permittivity of thin dielectric materials”. In: *Measurement Science and Technology* 11.11 (2000), pp. 1617–1622.

[44] Alessandra La Gioia et al. “Open-Ended Coaxial Probe Technique for Dielectric Measurement of Biological Tissues: Challenges and Common Practices”. In: *Diagnostics* 8.2 (2018), p. 40.

[45] A. García et al. “Dielectric properties of grape juice at 0.2 and 3 GHz”. In: *Journal of Food Engineering* 48.3 (2001), pp. 203–211.

[46] Jerome A. Cuenca et al. “Investigating the Broadband Microwave Absorption of Nanodiamond Impurities”. In: *IEEE Transactions on Microwave Theory and Techniques* 63.12 (2015), pp. 4110–4118.

[47] Moongi Jeong et al. “Non-Resonant Waveguide Technique for Measurement of Microwave Complex Permittivity of Ferroelectrics and Related Materials”. In: *Journal of the Korean Ceramic Society* 42.7 (2005), pp. 449–454.

[48] Jaroslaw Uher and Wolfgang J R Hoefer. “Tunable microwave and millimeter-wave band-pass filters”. In: *IEEE Transactions on Microwave Theory and Techniques* 39.4 (1991), pp. 643–653.

[49] S.J. Fiedziuszko. “Dual-Mode Dielectric Resonator Loaded Cavity Filters”. In: *IEEE Transactions on Microwave Theory and Techniques* 30.9 (1982), pp. 1311–1316.

[50] R.S. Kwok and Ji-Fuh Liang. “Characterization of high-Q resonators for microwave filter applications”. In: *IEEE Transactions on Microwave Theory and Techniques* 47.1 (1999), pp. 111–114.

[51] Hiroshi H. Kobayashi and Seiya Ogawa. “Dielectric constant and conductivity measurement of powder samples by the cavity perturbation method”. In: *Japanese Journal of Applied Physics* 10.3 (1971), pp. 345–350.

[52] Yong Guan and Yoshio Nikawa. “Measurement of temperature-dependent complex permittivity for materials using cylindrical resonator under microwave irradiation”. In: *Electronics and Communications in Japan, Part II: Electronics (English translation of Denshi Tsushin Gakkai Ronbunshi)* 90.11 (2007), pp. 1–8.

[53] Maik Eichelbaum et al. “The microwave cavity perturbation technique for contact-free and in situ electrical conductivity measurements in catalysis and materials science”. In: *Physical Chemistry Chemical Physics* 14.3 (2012), pp. 1302–1312.

[54] R.G. Carter. “Accuracy of microwave cavity perturbation measurements”. In: *IEEE Transactions on Microwave Theory and Techniques* 49.5 (2001), pp. 918–923.

[55] Hirokazu Kawabata et al. “Measurement accuracy of a $TM_{0m0}$ mode cavity method to measure complex permittivity of rod samples”. In: *2006 Asia-Pacific Microwave Conference*. IEEE, 2006, pp. 1465–1470.

[56] H.E. Bussey and A.J. Estin. “Errors in Dielectric Measurements Due to a Sample Insertion Hole in a Cavity”. In: *IEEE Transactions on Microwave Theory and Techniques* 8.6 (1960), pp. 650–653.

[57] R.A. Waldron. “Perturbation theory of resonant cavities”. In: *Proceedings of the IEE Part C: Monographs* 107.12 (1960), p. 272.

[58] Markus Dietrich et al. “A Laboratory Test Setup for in situ Measurements of the Dielectric Properties of Catalyst Powder Samples under Reaction Conditions by Microwave Cavity Perturbation: Set up and Initial Tests”. In: *Sensors* 14.9 (2014), pp. 16856–16868.

[59] Nicholas Clark. “Microwave Methods for Additive Layer Manufacturing”. PhD thesis. Cardiff University, 2017.

[60] Jon Hartley, Adrian Porch, and Martin Jones. “A non-invasive microwave method for assessing solid-state ammonia storage”. In: *Sensors and Actuators B: Chemical* 210.9 (2015), pp. 726–730.

[61] Jerzy Krupka et al. “A dielectric resonator for measurements of complex permittivity of low loss dielectric materials as a function of temperature”. In: *Measurement Science and Technology* 9.10 (1998), pp. 1751–1756.

[62] Joaquín Mollá et al. “Dielectric Property Measurement System at Cryogenic Temperatures and Microwave Frequencies”. In: *IEEE Transactions on Instrumentation and Measurement* 42.4 (1993), pp. 817–821.

[63] Nidhi Verma and Bhavana Jharia. “A New Temperature Compensation Method For Circular Cavity Resonator Using Low Conductivity Cooling Water System Based On Convection Heat Transfer”. In: *International Journal of Advanced Research in Computer Science and Electronics Engineering* 1.4 (2012), pp. 43–47.

[64] Jerome A. Cuenca, Daniel R. Slocombe, and Adrian Porch. “Temperature Correction for Cylindrical Cavity Perturbation Measurements”. In: *IEEE Transactions on Microwave Theory and Techniques* 65.6 (2017), pp. 2153–2161.

[65] Jerome A. Cuenca, Daniel R. Slocombe, and Adrian Porch. “Corrections to "Temperature Correction for Cylindrical Cavity Perturbation Measurements" [Jun 17 2153-2161]”. In: *IEEE Transactions on Microwave Theory and Techniques* 65.12 (2017), pp. 5078–5078.

[66] Udo Kaatze. “Complex permittivity of water as a function of frequency and temperature”. In: *Journal of Chemical and Engineering Data®* 34.4 (1989), pp. 371–374.

[67] W. J. Ellison. “Permittivity of pure water, at standard atmospheric pressure, over the frequency range 0-25 THz and the temperature range 0-100 °C”. In: *Journal of Physical and Chemical Reference Data* 36.1 (2007), pp. 1–18.

[68] M. Merabet and T. K. Bose. “Dielectric measurements of water in the radio and microwave frequencies by time domain reflectometry”. In: *The Journal of Physical Chemistry* 92.21 (1988), pp. 6149–6150.

[69] Jerome Cuenca. “Characterisation of Powders using Microwave Cavity Perturbation”. PhD thesis. Cardiff University, 2015.

[70] S. Syed Azim et al. “Studies on graphite based conductive paint coatings”. In: *Progress in Organic Coatings* 55.1 (2006), pp. 1–4.

[71] Taosheng Wang et al. “Study on the graphite nanosheets/resin shielding coatings”. In: *Progress in Organic Coatings* 59.2 (2007), pp. 101–105.

[72] Kristin Topp et al. “Coatings with metallic effect pigments for antimicrobial and conductive coating of textiles with electromagnetic shielding properties”. In: *Journal of Coatings Technology and Research* 11.6 (2014), pp. 943–957.

[73] H. Marchebois et al. “Zinc-rich powder coatings corrosion in sea water: Influence of conductive pigments”. In: *Progress in Organic Coatings* 45.4 (2002), pp. 415–421.

[74] T. Izumi et al. “Preparation of electrically conductive nano-powder of zinc oxide and application to transparent film coating”. In: *Journal of Alloys and Compounds* 480.1 (2009), pp. 123–125.

[75] R. N. Jagtap, P. P. Patil, and S. Z. Hassan. “Effect of zinc oxide in combating corrosion in zinc-rich primer”. In: *Progress in Organic Coatings* 63.4 (2008), pp. 389–394.

[76] Peiwei Hu Huaming Yang. "Controlled coating of antimony-doped tin oxide nanoparticles on kaolinite particles". In: *Applied Clay Science* 48.3 (2010), pp. 368–374.

[77] Sanghun Jeon et al. "Gated three-terminal device architecture to eliminate persistent photoconductivity in oxide semiconductor photosensor arrays". In: *Nature Materials* 11.4 (2012), pp. 301–305.

[78] P. Görrn et al. "The influence of visible light on transparent zinc tin oxide thin film transistors". In: *Applied Physics Letters* 91.19 (2007), pp. 2005–2008.

[79] Karim S. Karim et al. "Drain-bias dependence of threshold voltage stability of amorphous silicon TFTs". In: *IEEE Electron Device Letters* 25.4 (2004), pp. 188–190.

[80] M. J. Powell et al. "Bias dependence of instability mechanisms in amorphous silicon thin-film transistors". In: *Applied Physics Letters* 51.16 (1987), pp. 1242–1244.

[81] Stephan Lany and Alex Zunger. "Anion vacancies as a source of persistent photoconductivity in II-VI and chalcopyrite semiconductors". In: *Physical Review B - Condensed Matter and Materials Physics* 72.3 (2005), pp. 1–13.

[82] H. X. Jiang and J. Y. Lin. "Percolation transition of persistent photoconductivity in II-VI mixed crystals". In: *Physical Review Letters* 64.21 (1990), pp. 2547–2550.

[83] Jens Reemts and Achim Kittel. "Persistent photoconductivity in highly porous ZnO films". In: *Journal of Applied Physics* 101.1 (2007), p. 013709.

[84] X. Y. Xue et al. "Extremely high oxygen sensing of individual $ZnSnO_3$ nanowires arising from grain boundary barrier modulation". In: *Applied Physics Letters* 91.2 (2007), p. 022111.

[85] Q H Li et al. "Adsorption and desorption of oxygen probed from ZnO nanowire films by photocurrent measurements". In: *Applied Physics Letters* 86.12 (2005), p. 123117.

[86] J. C. Crano et al. "Photochromic compounds: Chemistry and application in ophthalmic lenses". In: *Pure and Applied Chemistry* 68.7 (2007), pp. 1395–1398.

[87] Tao He and Jiannian Yao. "Photochromic materials based on tungsten oxide". In: *Journal of Materials Chemistry* 17.43 (2007), pp. 4547–4557.

[88] Shoutian Li and M. Samy El-Shall. "Synthesis and characterization of photochromic molybdenum and tungsten oxide nanoparticles". In: *Nanostructured Materials* 12.1 (1999), pp. 215–219.

[89] Andreas Georg et al. "Switchable windows with tungsten oxide". In: *Vacuum* 82.7 (2008), pp. 730–735.

[90] Elias Burstein. "Anomalous Optical Absorption Limit in InSb". In: *Physical Review* 93.3 (1954), pp. 632–633.

[91] V. Senthilkumar et al. "Effects of annealing temperature on structural, optical, and electrical properties of antimony-doped tin oxide thin films". In: *Philosophical Magazine Letters* 90.5 (2010), pp. 337–347.

[92] J. Wu et al. "Effects of the narrow band gap on the properties of InN". In: *Physical Review B* 66.20 (2002), p. 201403.

[93] Alex T. Vai et al. "The Transition to the Metallic State in Polycrystalline n -type Doped ZnO Thin Films". In: *Zeitschrift für anorganische und allgemeine Chemie* 640.6 (2014), pp. 1054–1062.

[94] Ali Hassan et al. “Acceptor-modulated optical enhancements and band-gap narrowing in ZnO thin films”. In: *AIP Advances* 8.3 (2018), p. 035212.

[95] S. A. Studenikin, Nickolay Golego, and Michael Cocivera. “Optical and electrical properties of undoped ZnO films grown by spray pyrolysis of zinc nitrate solution”. In: *Journal of Applied Physics* 83.4 (1998), pp. 2104–2111.

[96] Nickolay Golego, S. A. Studenikin, and Michael Cocivera. “Spray pyrolysis preparation of porous polycrystalline thin films of titanium dioxide containing Li and Nb”. In: *Journal of Materials Research* 14.3 (1999), pp. 698–707.

[97] K Madhusudan Reddy, Sunkara V Manorama, and A Ramachandra Reddy. “Bandgap studies on anatase titanium dioxide nanoparticles”. In: *Materials Chemistry and Physics* 78.1 (2003), pp. 239–245.

[98] Tim Luttrell et al. “Why is anatase a better photocatalyst than rutile? - Model studies on epitaxial $TiO_2$ films”. In: *Scientific Reports* 4 (2015), pp. 1–8.

[99] Kazuya Nakata and Akira Fujishima. “$TiO_2$ photocatalysis: Design and applications”. In: *Journal of Photochemistry and Photobiology C: Photochemistry Reviews* 13.3 (2012), pp. 169–189.

[100] Lihong Yu et al. “The degradation mechanism of methyl orange under photo-catalysis of $TiO_2$”. In: *Physical Chemistry Chemical Physics* 14.10 (2012), p. 3589.

[101] Yikui Du and Joseph Rabani. “The Measure of $TiO_2$ Photocatalytic Efficiency and the Comparison of Different Photocatalytic Titania”. In: *The Journal of Physical Chemistry B* 107.43 (2003), pp. 11970–11978.

[102] Lizhong Sun and James R. Bolton. “Determination of the Quantum Yield for the Photochemical Generation of Hydroxyl Radicals in $TiO_2$ Suspensions”. In: *The Journal of Physical Chemistry* 100.10 (1996), pp. 4127–4134.

[103] Guido Rothenberger et al. “Charge carrier trapping and recombination dynamics in small semiconductor particles”. In: *Journal of the American Chemical Society* 107.26 (1985), pp. 8054–8059.

[104] Michael R. Hoffmann et al. “Environmental Applications of Semiconductor Photocatalysis”. In: *Chemical Reviews* 95.1 (1995), pp. 69–96.

[105] Norman S. Allen et al. “The effect of crystalline phase (anatase, brookite and rutile) and size on the photocatalytic activity of calcined polymorphic titanium dioxide ($TiO_2$)”. In: *Polymer Degradation and Stability* 150.January (2018), pp. 31–36.

[106] Aaron Wold. “Photocatalytic properties of titanium dioxide ($TiO_2$)”. In: *Chemistry of Materials* 5.3 (1993), pp. 280–283.

[107] Andrea Folli et al. “Photogenerated Charge Carriers and Paramagnetic Species in (W,N)-Codoped $TiO_2$ Photocatalysts under Visible-Light Irradiation: An EPR Study”. In: *The Journal of Physical Chemistry C* 117.42 (2013), pp. 22149–22155.

[108] Andrea Folli et al. “Improving the Selectivity of Photocatalytic $NO_x$ Abatement through Improved $O_2$ Reduction Pathways Using $Ti_{0.909}W_{0.091}O_2N_x$ Semiconductor Nanoparticles: From Characterization to Photocatalytic Performance”. In: *ACS Catalysis* 8.8 (2018), pp. 6927–6938.

[109] Ye Cong et al. “Synthesis and Characterization of Nitrogen-Doped $TiO_2$ Nanophotocatalyst with High Visible Light Activity”. In: *The Journal of Physical Chemistry C* 111.19 (2007), pp. 6976–6982.

[110] Stefano Livraghi et al. “Origin of Photoactivity of Nitrogen-Doped Titanium Dioxide under Visible Light”. In: *Journal of the American Chemical Society* 128.49 (2006), pp. 15666–15671.

[111] Shanmugasundaram Sakthivel and Horst Kisch. “Photocatalytic and Photoelectrochemical Properties of Nitrogen-Doped Titanium Dioxide”. In: *ChemPhysChem* 4.5 (2003), pp. 487–490.

[112] Clemens Burda et al. “Enhanced Nitrogen Doping in $TiO_2$ Nanoparticles”. In: *Nano Letters* 3.8 (2003), pp. 1049–1051.

[113] Cristiana Di Valentin, Gianfranco Pacchioni, and Annabella Selloni. “Theory of Carbon Doping of Titanium Dioxide”. In: *Chemistry of Materials* 17.26 (2005), pp. 6656–6665.

[114] Shanmugasundaram Sakthivel and Horst Kisch. “Daylight Photocatalysis by Carbon-Modified Titanium Dioxide”. In: *Angewandte Chemie - International Edition* 42.40 (2003), pp. 4908–4911.

[115] Yu Huang et al. “Effect of Carbon Doping on the Mesoporous Structure of Nanocrystalline Titanium Dioxide and Its Solar-Light-Driven Photocatalytic Degradation of $NO_x$”. In: *Langmuir* 24.7 (2008), pp. 3510–3516.

[116] Li-Wu Zhang, Hong-Bo Fu, and Yong-Fa Zhu. “Efficient $TiO_2$ Photocatalysts from Surface Hybridization of $TiO_2$ Particles with Graphite-like Carbon”. In: *Advanced Functional Materials* 18.15 (2008), pp. 2180–2189.

[117] Hyunwoong Park et al. “Surface modification of $TiO_2$ photocatalyst for environmental applications”. In: *Journal of Photochemistry and Photobiology C: Photochemistry Reviews* 15.1 (2013), pp. 1–20.

[118] Shaozheng Hu, Fayun Li, and Zhiping Fan. “Composite Materials with Enhanced Photocatalytic Activity Under UV Light”. In: *Bulletin of the Korean Chemical Society* 33.6 (2012), pp. 1895–1899.

[119] Carl Anderson and Allen J. Bard. “Improved Photocatalytic Activity and Characterization of Mixed $TiO_2$ /$SiO_2$ and $TiO_2$ /$Al_2O_3$ Materials”. In: *The Journal of Physical Chemistry B* 101.14 (1997), pp. 2611–2616.

[120] Guofeng Wang et al. “Size-dependent upconversion luminescence in $YF_3$:$Yb^{3+}$/$Tm^{3+}$ nanobundles”. In: *Journal of Fluorine Chemistry* 129.11 (2008), pp. 1110–1113.

[121] Weiping Qin et al. “Near-infrared photocatalysis based on $YF_3$:$Yb^{3+}$,$Tm^{3+}$/$TiO_2$ core/shell nanoparticles”. In: *Chemical Communications* 46.13 (2010), p. 2304.

[122] John George et al. “Modification of $TiO_2$ surface for improved light fastness”. In: *International Journal of Industrial Chemistry* 6.3 (2015), pp. 133–141.

[123] Akihiro Hosokawa and Yoshiteru Kato. “Factors affecting color strength of printing on film-coated tablets by UV laser irradiation: $TiO_2$ particle size, crystal structure, or concentration in the film, and the irradiated UV laser power”. In: *Drug Development and Industrial Pharmacy* 37.8 (2011), pp. 901–906.

[124] Andriy Gonchar and Viktor Troshchylo. “Next Generation of TiO 2 Pigments. Project RC-8828: Titanium Dioxide Grade with Superior+ Durability, High Hiding Power, Excellent Dispersibility and High Initial Gloss.” In: *12th International Scientific-Technical Conference ACT'16*. November. 2016.

[125] Yu-Lan Lin, Ting-Jie Wang, and Yong Jin. “Surface characteristics of hydrous silica-coated $TiO_2$ particles”. In: *Powder Technology* 123.2-3 (2002), pp. 194–198.

[126] Ulrich Gesenhues. “Coprecipitation of Hydrous Alumina and Silica with $TiO_2$ Pigment as Substrate”. In: *Journal of Colloid and Interface Science* 168.2 (1994), pp. 428–436.

[127] S.M.A. Shibli and Francis Chacko. “Development of nano $TiO_2$-incorporated phosphate coatings on hot dip zinc surface for good paintability and corrosion resistance”. In: *Applied Surface Science* 257.7 (2011), pp. 3111–3117.

[128] Yunsheng Zhang et al. “Evolution of zirconia coating layer on rutile $TiO_2$ surface and the pigmentary property”. In: *Journal of Physics and Chemistry of Solids* 71.10 (2010), pp. 1458–1466.

[129] Rajesh J. Tayade et al. “Photocatalytic degradation of dyes and organic contaminants in water using nanocrystalline anatase and rutile $TiO_2$”. In: *Science and Technology of Advanced Materials* 8.6 (2007), pp. 455–462.

[130] T. Le Mercier et al. “Formation of $Ti^{3+}$ ions at the surface of laser-irradiated rutile”. In: *Applied Surface Science* 86.1-4 (1995), pp. 382–386.

[131] Martin Owen-Jones. *Viva conversation*.

[132] V. Kudrle et al. “Plasma diagnostics using electron paramagnetic resonance”. In: *Journal of Physics D: Applied Physics* 43.12 (2010), p. 124020.

# Appendix A

# Microwave Cavity Resonance derivations

## A.1 Derivation of ${S_{21}}^2$ equation from cavity resonator model

Firstly the schematic model shown in figure 2.8 is converted to a matrix representation using Kirchoff's voltage law:

$$\begin{bmatrix} V_a \\ V_b \end{bmatrix} = \begin{bmatrix} \frac{\omega^2 m_1^2}{Z_c} & -\frac{\omega^2 m_1 m_2}{Z_c} \\ -\frac{\omega^2 m_1 m_2}{Z_c} & \frac{\omega^2 m_2^2}{Z_c} \end{bmatrix} \begin{bmatrix} I_a \\ I_b \end{bmatrix} \tag{A.1}$$

This can then be converted to an $S_{21}$ using the following equation:

$$S_{21} = \frac{2Z_0 Z_{21}}{(Z_{11}+Z_0)(Z_{22}+Z_0) - Z_{12}Z_{21}} \tag{A.2}$$

This results in the following:

$$S_{21} = \frac{-2m_1 m_2}{m_1^2 + m_2^2 + \frac{Z_0 Z_C}{\omega^2}} \tag{A.3}$$

We can then take the magnitude squared of this equation which results in the final equation for $|S_{21}|^2$:

$$|S_{21}|^2 = \frac{4g_1 g_2}{(g_1+g_2+1)^2 + 4Q_0^2\left(\frac{\omega-\omega_0}{\omega_0}\right)^2} \tag{A.4}$$

where $g_n$ is defined as the coupling coefficient of the resonator:

$$g_n = \frac{\omega_0^2 m_n^2}{Z_0 Z_R} \approx \frac{\omega_0^2 m_n^2}{Z_0 R} \tag{A.5}$$

### A.1.1 Converting to peak power and loaded Q factor representation

To simplify the following equations we make the assumption that $g_1 \approx g_2 = g$. At resonance (where $\omega = \omega_0$) the peak transmitted power can then be derived:

$$P_0 = \frac{4g^2}{(1+2g)^2} \tag{A.6}$$

Substituting this back into the equation for $|S_{21}|^2$ yields:

$$|S_{21}|^2 = \frac{P_0}{1 + \frac{4Q_0^2\left(\frac{\omega-\omega_0}{\omega_0}\right)^2}{(1+2g)^2}} \tag{A.7}$$

The loaded Q can then be defined as

$$Q_L = \frac{Q_0}{1+2g} \tag{A.8}$$

Finally, substituting equation A.6 back into equation A.8 then yields the equation to convert loaded Q into unloaded Q:

$$Q_L = Q_0(1 - \sqrt{P_0}) \tag{A.9}$$

We can also substitute equation A.8 back into A.7 to yield the final lorentzian function which solely depends of parameters that can be measured from a VNA:

$$|S_{21}|^2 = \frac{P_0}{1 + 4Q_L^2\left(\frac{\omega-\omega_0}{\omega_0}\right)^2} \tag{A.10}$$

## A.2 Derivation of TM modes for a cylindrical microwave resonant cavity

A transverse magnetic mode of a cylindrical resonant cavity only contains an electric field along the axis of the cylinder. Using the electric field helmholtz equation, substituting $k^2 = \omega^2\mu\varepsilon$ and applying the laplacian operator to $E_z$ results in the following

$$\frac{1}{r}\frac{\partial}{\partial r}\left(r\frac{\partial E_z}{\partial r}\right) + \frac{1}{r^2}\frac{\partial^2 E_z}{\partial \phi^2} + \frac{\partial^2 E_z}{\partial z^2} + k^2 E_z = 0 \tag{A.11}$$

To solve this, the $E_z$ field can be split into functions that are only dependent on a single axis

$$E_z(r,\phi,z) = R(r)\Phi(\phi)Z(z) \tag{A.12}$$

This allows us to represent the first equation as below

$$\frac{1}{rR}\frac{d}{dr}\left(r\frac{dR}{dr}\right) + \frac{1}{r^2\Phi}\left(\frac{d^2\Phi}{d\phi^2}\right) + \frac{1}{Z}\left(\frac{d^2 Z}{dz^2}\right) + k^2 = 0 \tag{A.13}$$

For the whole equation to equal zero, each part has to equal some constant independent of the position $r,\phi,z$. The second to last term is only a function of $z$, so we can separate it out

$$\frac{d^2 Z}{dz^2} + k_z^2 Z = 0 \tag{A.14}$$

where $k_z$ is a constant. This is a second order linear differential equation which can be solved to find $Z$

$$\begin{aligned} Z &= C_1' e^{jk_z z} + C_2' e^{-jk_z z} \\ &= C_1'(\cos(k_z z) + j\sin(k_z z)) + C_2'(\cos(k_z z) - j\sin(k_z z)) \\ &= (C_1' + C_2')\cos(k_z z) + j(C_1' - C_2')\sin(k_z z) \\ &= C_1\cos(k_z z) + C_2\sin(k_z z) \end{aligned} \tag{A.15}$$

At $z = 0$ and $z = h$ where $h$ is the height of the cavity, $Z(z)$ is at it's peak resulting in:

$$Z = C_1 \cos(\frac{z\pi p}{h}) \tag{A.16}$$

Substituting equation A.14 back into equation A.13 yields

$$\frac{1}{rR}\frac{d}{dr}\left(r\frac{dR}{dr}\right) + \frac{1}{r^2\Phi}\left(\frac{d^2\Phi}{d\phi^2}\right) + k^2 - k_z^2 = 0 \tag{A.17}$$

If we let $k_r^2 = k^2 - k_z^2$ and multiply by $r^2$ then

$$\frac{r}{R}\frac{d}{dr}\left(r\frac{dR}{dr}\right) + \frac{1}{\Phi}\left(\frac{d^2\Phi}{d\phi^2}\right) + r^2k_r^2 = 0 \tag{A.18}$$

We can then separate the $\Phi$ terms

$$\frac{1}{\Phi}\frac{d^2\Phi}{d\phi^2} = -m^2 \tag{A.19}$$

Again, solving the 2nd order linear differential equation

$$\Phi = C_3 \cos\left(m\left(\phi \pm \frac{\pi}{4}\right)\right) \tag{A.20}$$

The reason for the $\pm\frac{\pi}{4}$ is because $\mathrm{TM}_{mmp}$ modes where $m > 0$ can have two solutions simultaneously. Substituting equation A.19 back into equation A.18 yields

$$\frac{r}{R}\frac{d}{dr}\left(r\frac{dR}{dr}\right) + r^2k_r^2 - m^2 = 0 \tag{A.21}$$

Multiplying through by $R$ results in

$$r\frac{d}{dr}\left(r\frac{dR}{dr}\right) + R(r^2k_r^2 - m^2) = 0 \tag{A.22}$$

Using the product rule, the differential can be simplified

$$r^2\frac{d^2R}{dr^2} + r\frac{dR}{dr} + R(r^2k_r^2 - m^2) = 0 \tag{A.23}$$

This equation is in the form of bessel's differential equation which has the following solution

$$R = C_4 J_m(rk_r) + C_5 Y_m(rk_r) \tag{A.24}$$

Since there cannot be infinite electric field at the origin, the $C_5$ term must be zero. The $E_z$ field must also be zero at the cavity radius. To satisfy these boundary conditions we let $\alpha_{mn}$ be the $n^{\text{th}}$ root of the bessel function $J_m$. $R$ then becomes:

$$R = C_4 J_m(\frac{r\alpha_{mn}}{a}) \tag{A.25}$$

if we then substitute $R$, $\Phi$ and $Z$ back into equation A.12 then we arrive at the final $E_z$ equation for the fields of a $\text{TM}_{mmp}$ resonant mode:

$$E_z(r,\phi,z) = E_0 J_m\left(\frac{\alpha_{mn} r}{a}\right)\cos(m\phi+\theta)\cos\left(\frac{z\pi p}{h}\right) \tag{A.26}$$

# Appendix B

# Separated Red, Green and blue values of Iriotec foil scans

Below is the full RGB scan data of the averaged luminance values shown in figures 6.14 to 6.19

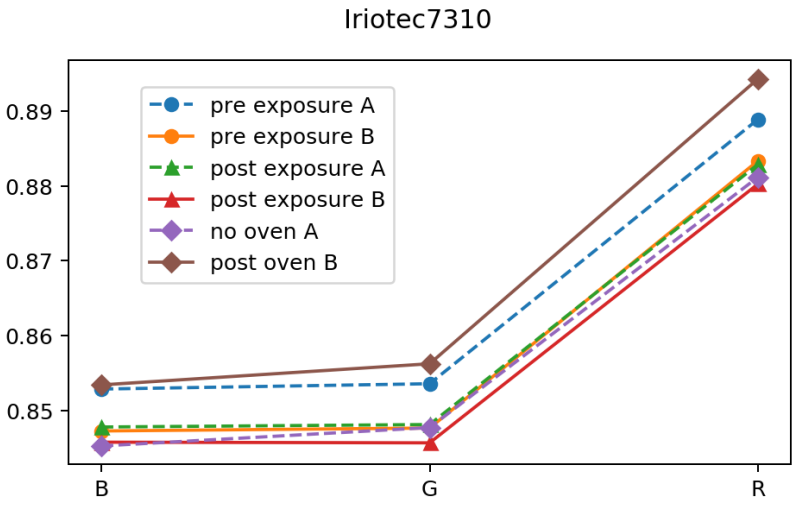


Fig. B.1 Oven experiment RGB scan results for Iriotec 7310.

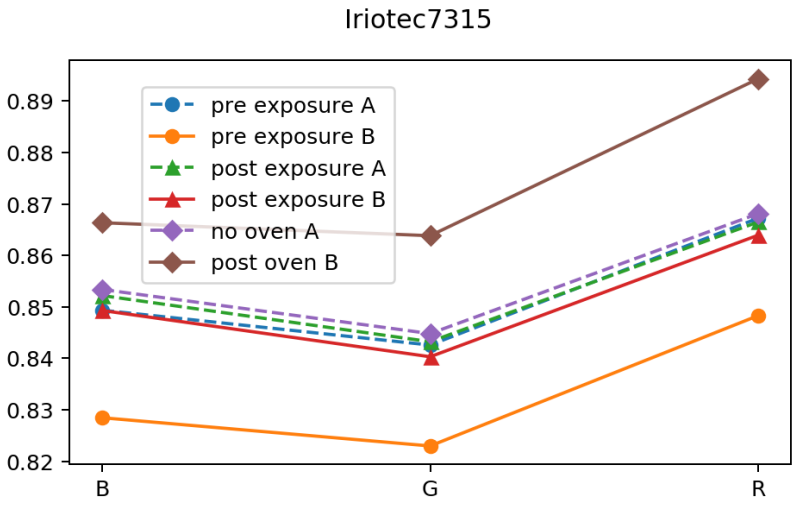


Fig. B.2 Oven experiment RGB scan results for Iriotec 7315.

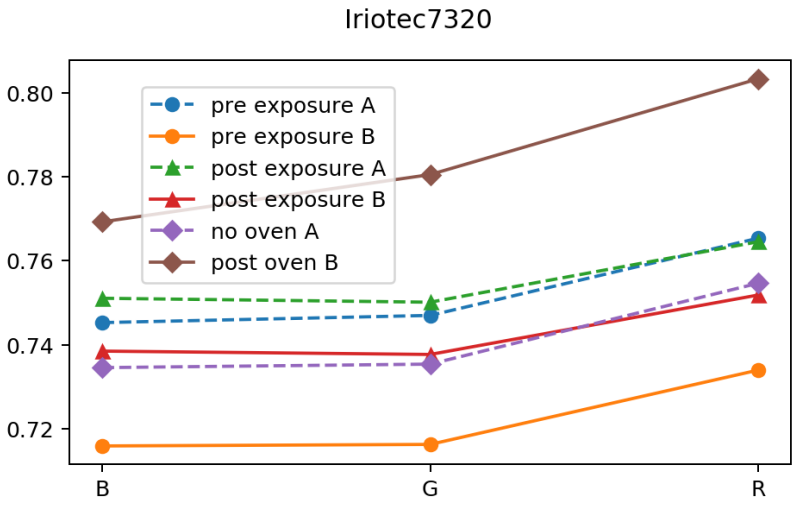


Fig. B.3 Oven experiment RGB scan results for Iriotec 7320.

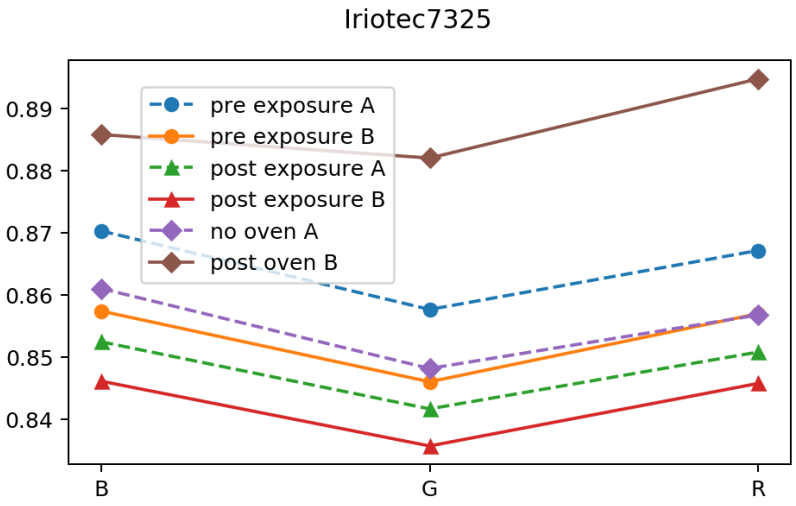


Fig. B.4 Oven experiment RGB scan results for Iriotec 7325.

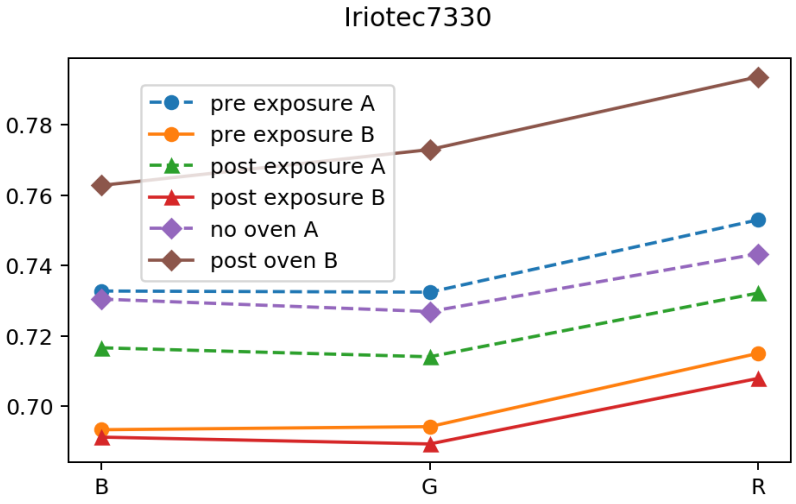


Fig. B.5 Oven experiment RGB scan results for Iriotec 7330.

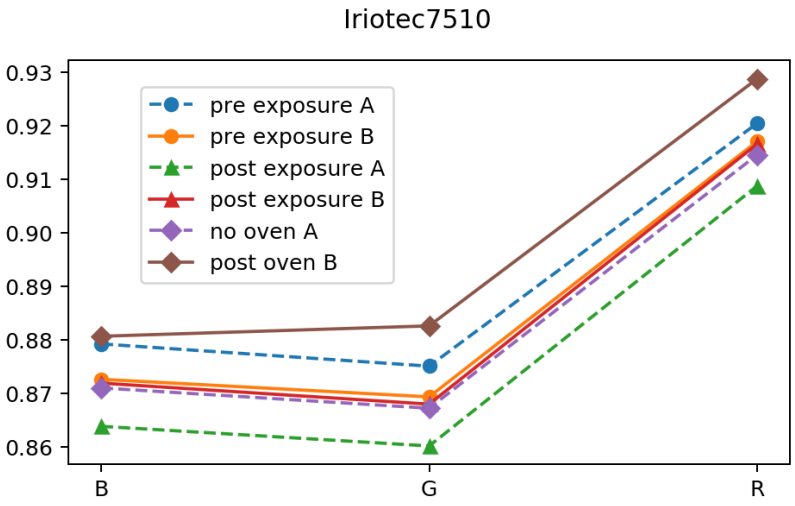


Fig. B.6 Oven experiment RGB scan results for Iriotec 7510.

# Appendix C

# X-ray diffraction patterns for $TiO_2$ powders

Below are the x-ray diffraction patterns of the $TiO_2$ powders. These measurements were kindly provided by Andrea Folli from the chemistry department at Cardiff University.

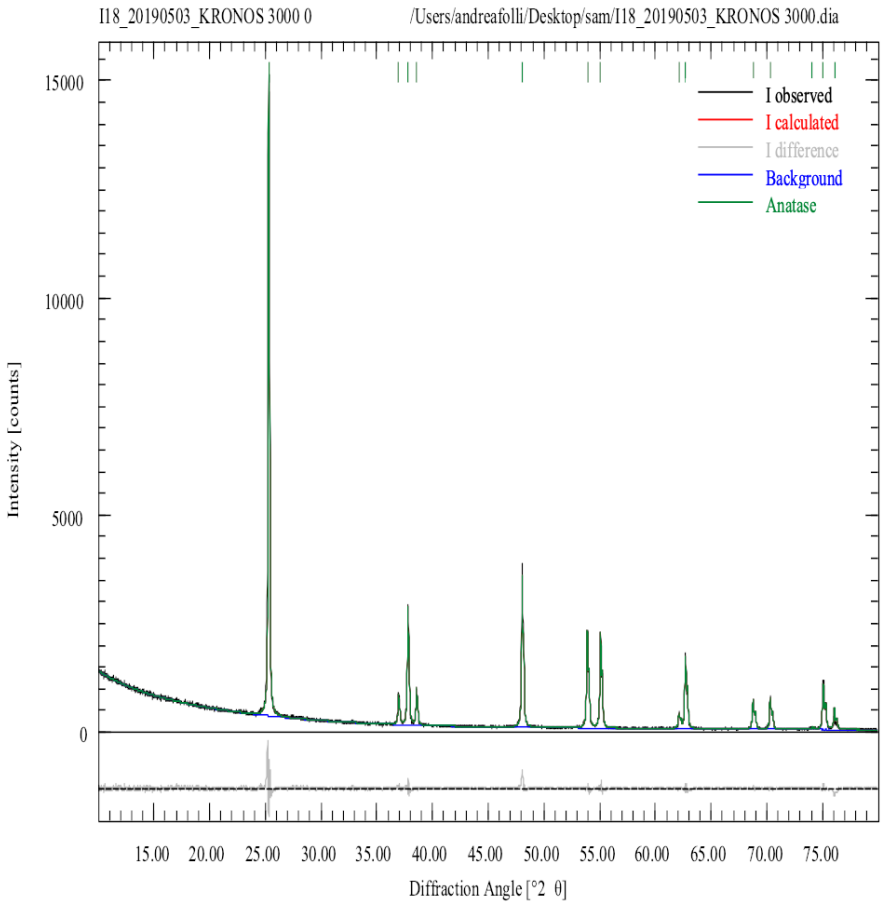


Fig. C.1 X-ray diffraction pattern for Kronos 3000.

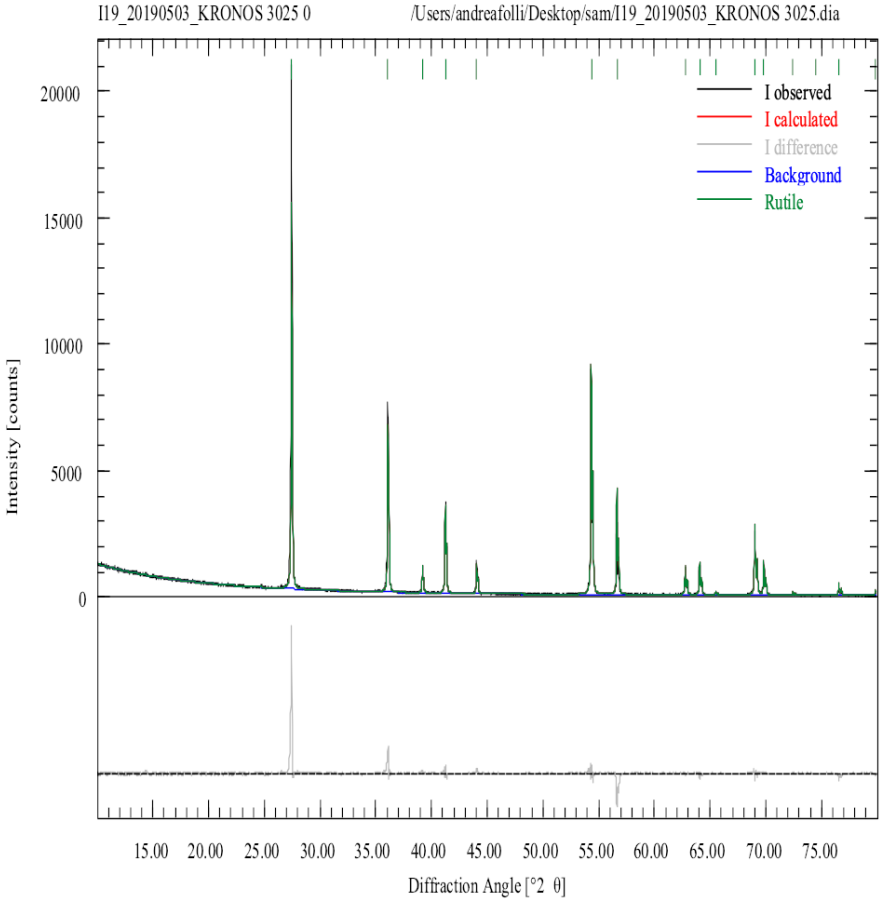


Fig. C.2 X-ray diffraction pattern for Kronos 3025.

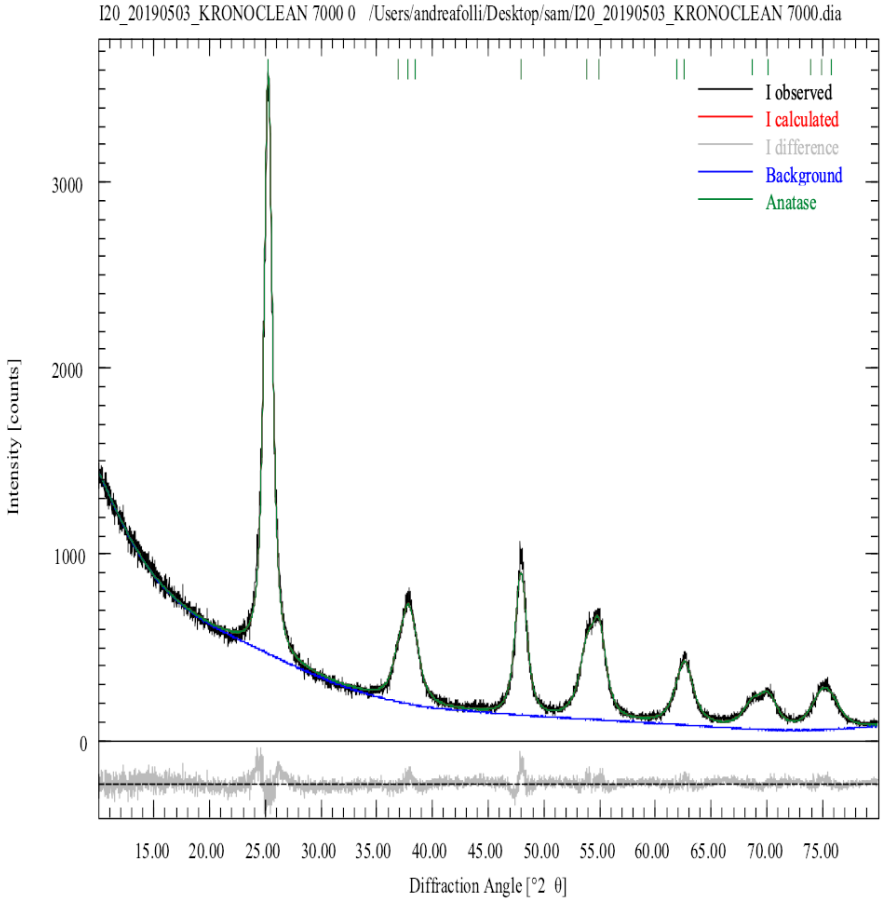


Fig. C.3 X-ray diffraction pattern for Kronoclean 7000.